Computational Investigation of Complex Molecular Fluids

A Thesis submitted in partial fulfillment
for the degree of
Master of Science
as a part of the
Integrated Ph.D. programme
(Materials Science)

by

Anirban Mondal

Chemistry and Physics of Materials Unit
Jawaharlal Nehru Centre for Advanced Scientific Research
Bangalore – 560 064, India

MARCH 2013

To My Parents

DECLARATION

I hereby declare that the matter embodied in the thesis entitled "**Computational Investigation of Complex Molecular Fluids**" is the result of investigations carried out by me at the Chemistry and Physics of Materials Unit, Jawaharlal Nehru Centre for Advanced Scientific Research, Bangalore, India under the supervision of Prof. S. Balasubramanian and that it has not been submitted elsewhere for the award of any degree or diploma.

In keeping with the general practice in reporting scientific observations, due acknowledgement has been made whenever the work described is based on the findings of other investigators. Any omission that might have occurred by oversight or error of judgement is regretted.

Anirban Mondal

CERTIFICATE

I hereby certify that the matter embodied in this thesis entitled "**Computational Investigation of Complex Molecular Fluids**" has been carried out by Mr. Anirban Mondal at the Chemistry and Physics of Materials Unit, Jawaharlal Nehru Centre for Advanced Scientific Research, Bangalore, India under my supervision and that it has not been submitted elsewhere for the award of any degree or diploma.

Prof. S. Balasubramanian
(Research Supervisor)

Acknowledgements

It is my immense pleasure to thank my research supervisor, Prof. S. Balasubramanian for giving me an opportunity to explore the interesting area of research on computational materials science. I am extremely thankful to him for suggesting me interesting research problems and for his guidance, support, and encouragement right from the beginning of this project. I sincerely acknowledge the academic freedom that I received in his group and the advices and suggestions at various stages of the work. I am greatly thankful to him for providing me excellent computing resources without which the project would not have been successful.

I would like to thank to all the faculty members of CPMU, TSU, NCU and ICMS for the courses they offered. I am particularly thankful to Prof. Swapan Pati, Prof. Umesh Waghmare, Prof. Chandrabhas Narayana, Prof. Shobhana Narasimhan, Dr. Santosh Ansumali and Dr. Kanishka Biswas for the fruitful discussions I had with them.

I am thankful to the open source community for their service in providing the useful softwares and operating systems. I particularly acknowledge the developers of LAMMPS, CP2K, CPMD and VMD softwares.

I have enjoyed the company and friendship of my present and past lab mates : Kanchan Sastri Palla, Sandeep K. Reddy, Rajdeep Singh Payal, K. Chidambar, B. Satyanarayana, Tarak Karmakar, B. Karteek, Chaitanya Sharma, Pallabi Haldar and Dr. Ganga Periyasami.

I acknowledge JNCASR, TUE-CMS and C-MMACS for computational facilities.

I thank all my friends for all the moments I shared with them.

Finally, I am thankful to my family members, who have been a source of constant support and strength for years. I thank my parents, brother and Brishti for their patience and encouragement.

I thank all those who have helped me directly or indirectly.

Preface

The thesis presents the results of investigations on complex molecular fluids using computational methods, such as classical molecular dynamics simulations, *ab initio* simulations and density functional theory (DFT) based quantum chemical calculations.

Chapter 1 presents a general introduction to heavy metal extraction and to room temperature ionic liquids describing their physicochemical properties and applications. This chapter also contains a brief discussion on the classical molecular dynamics simulation method, *ab initio* molecular dynamics method and density functional theory (DFT).

In Chapter 2, the complex behaviour of an extractant (Tri-*n*-butyl phosphate) used in the nuclear reprocessing industry is explored using classical molecular dynamics simulation. Aggregation of TBP molecules in *n*-octane up to a dimer is observed.

In Chapter 3, *ab initio* studies have been performed to derive atomic partial charges for imidazolium cation based room temperature ionic liquids, from their crystalline phase. The total charge on the ions is found to be less than unity. The current method is robust and provides a natural and amenable framework to derive site charges which can be used in classical force fields to model the condensed state. The charges are also correlated against experimentally determined polarities of these liquids.

In Chapter 4, the effect of cation-anion hydrogen bonding in modulating the low frequency vibrational modes in ionic liquids is studied using quantum chemical cluster calculations.

Contents

List of Figures

List of Tables

Chapter 1

Introduction

Complex molecular fluids find enormous applications in chemistry. The organization of molecules into self-assembled structures in certain contexts, leads to the emergence of many novel properties which are absent or unthinkable at the single molecule level. Complexity is thus tied to emergent behavior from the association of the individuals. This thesis describes how complexity is a feature of organic solutions used in heavy metal extraction in the nuclear processing industry. The thesis also contains simulation results of room temperature ionic liquids, a class of salts which have low melting points and exhibit interesting organized structures. The thesis provides a robust framework to derive atomic partial charges for the ions in ionic liquids using ab initio approaches. The final chapter describes how subtle hydrogen bonding interactions between the cation and the anion in an ionic liquid modulates the low frequency vibrational spectrum.

1.1 Nuclear Reprocessing

Nuclear reprocessing is the chemical treatment of spent fuel involving separation of its various constituents. Nuclear reprocessing has been used for multiple purposes, and their relative importance has changed over time. Principally, it is used to recover useful actinides from the spent fuel. A variety of chemical methods have been proposed and demonstrated for reprocessing of nuclear fuel.[1,2] In aqueous reprocessing technology, nuclear fuel is dissolved into an acidic solution. The resulting solution is then chemically processed to separate the metals of interest, typically uranium and/or plutonium.

Liquid-liquid extraction (also called solvent extraction) can be described as the partitioning of a species (solute) between two immiscible liquids. These immiscible liquids most often consist of an organic and an aqueous phase. The organic phase before extraction is called the solvent (hence the commonly used name solvent extraction) and the aqueous phase containing the solute is called the feed. The solvent always consists of a diluent, which is the bulk phase, and sometimes also of one or more several extractants. The extractant is the component that is primarily responsible for transferring the solute from one phase to another. One of the important and most often used liquid-liquid extraction method is known as PUREX. PUREX, the current standard method, is an acronym standing for *Plutonium and Uranium Recovery by EXtraction*. It has been used to extract uranium and plutonium independent of each other, from the fission product.

Tri-*n*-butyl phosphate, is an organophosphorus compound with the chemical formula $(CH_3CH_2CH_2CH_2O)_3PO$. It is commonly known as TBP. TBP is an ester of orthophosphoric acid and butanol; it is a colorless, odorless liquid. TBP is a commonly used extractant and phase modifier in solvent extraction.TBP, which is considered to be a hard Lewis base, has a well-documented ability to extract uranium and plutonium directly from dissolved used nuclear fuel. Metal extraction with TBP follows the solvation extraction mechanism. The molecular structure of TBP is shown in Figure 1.1.

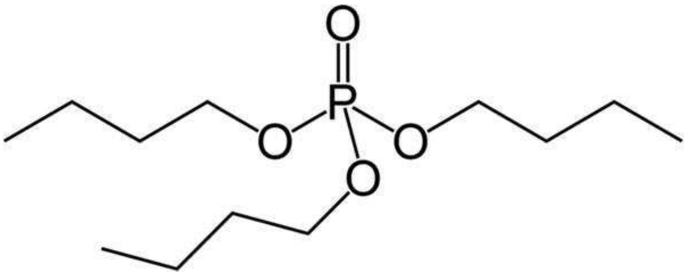

Figure 1.1: Molecular structure of Tri-*n*-butyl phosphate.[134]

1.2 Room Temperature Ionic Liquids

In our daily lives we come across several ionic salts; sodium chloride (NaCl) is one of the most important among them, which is also known as common salt. These ionic crystals have very large values of Madelung energy due to strong electrostatic interactions. Such compounds are solids at room temperature and usually have very high melting points that limits their use as solvents in most applications. For an example, the melting point of NaCl is 1074 K.[3]

Room temperature ionic liquids (RTILs)[4–9] are defined as liquids that are composed entirely of ions and are fluid below 100 °C. RTILs possess both organic and inorganic moieties. RTILs generally consist of bulky and asymmetric organic cations based on methylimidazolium [Rmim], N-butylpyridinium [RNbupy], pyrrolidinium, tetraalkylammonium and tetraalkylphosphonium. Some of these cations, such as imidazolium possess an aromatic ring that is polar and nonpolar substituents side groups that are predominantly alkyl chains. Figure 1.2 shows the chemical formulae of some of these cations. Structures of some of the cations are presented in Figure 1.3.

Compared to cation bases, anions are more in number. Some examples of those anions are, halides, nitrate $[NO_3]^-$, tetrafluoroborate $[BF_4]^-$, hexafluorophosphate $[PF_6]^-$, alkylsulfates $[RSO_4]^-$, alkylsulfonates $[RSO_3]^-$, sulfate $[NO_3]^-$, aluminium chloride $[AlCl_4]^-$, bis(trifluoromethylsulfonyl)imide $[(CF_3SO_2)_2N]$ or $[Tf_2N]^-$, triflate $[CF_3SO_3]^-$, perchlorate $[ClO_4]^-$ etc.[10–13,15–18,27] Structures of some anions are

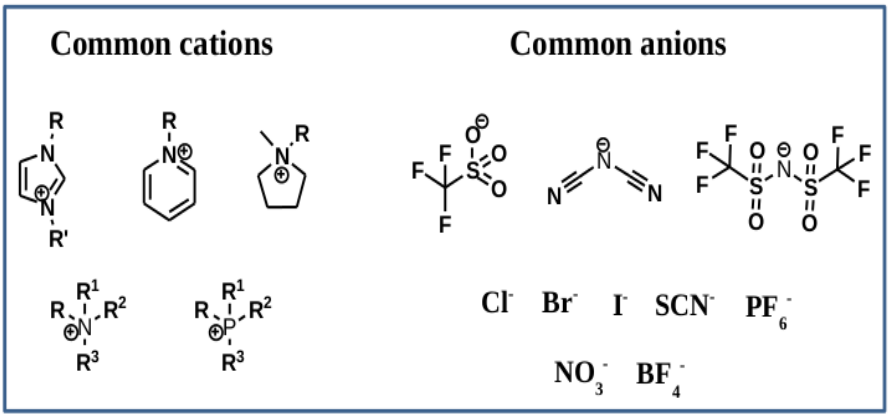

Figure 1.2: Constituents of room temperature ionic liquids.

given in Figure 1.4. In general, the anions used in the ionic liquid can be broadly divided as fluorous and non-fluorous anions. Tetrafluroborate $[BF_4]^-$, hexafluorophosphate $[PF_6]^-$ being the most prominent among the fluorous anions. Anions influence the properties of ILs in a major way. For example, [bmim]$[BF_4]$ is water soluble^4 whereas [bmim]$[PF_6]$ is sparingly soluble in water.^{19} Similarly, we can expect large changes when a fluorous anion is replaced with a non-fluorous one. For example, carbohydrates are sparingly soluble (< 0.5 g/L) in [bmim]$[BF_4]$, whereas [bmim][dca] that is based on the dicyanamide anion dissolves large amount of ($\approx$ 200 g/L) of carbohydrates such as glucose and sucrose.^{20}

The R group of the cation can be varied, typical examples are alkyl chains such as methyl, ethyl, butyl etc., but can also be any of a variety of other functional groups (e.g., alkenyl, methoxy). Various researchers have added hydroxyl functionality to it to increase water solubility or even amine functionality to increase the uptake of carbon dioxide in the ionic liquid. Thus, the properties of the ionic liquids can be tuned by adjusting the R groups in the imidazolium, pyridinium, pyrrolidinium, ammonium or phosphonium cations. Therefore, the possibility arises to optimize the ionic liquid for a specific application by stepwise tuning the relevant solvent properties. For this reason, ionic liquids have been referred to as designer solvents.

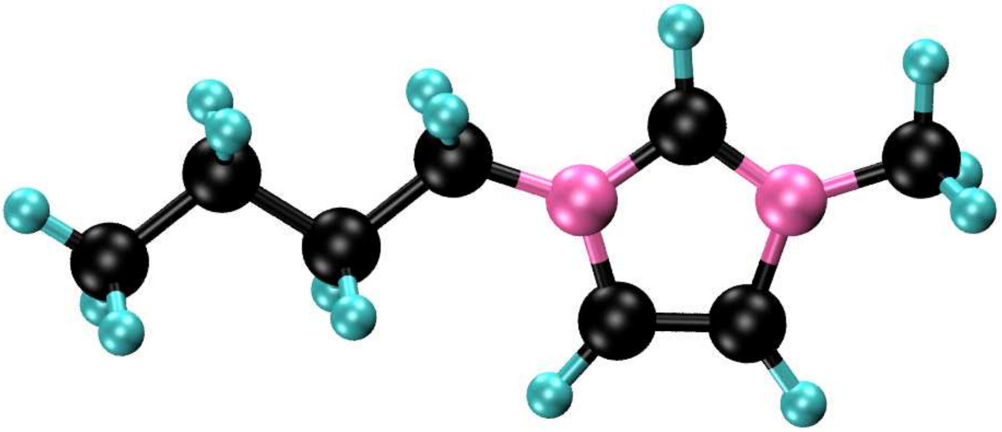

(a) 1-butyl-3-methylimidazolium

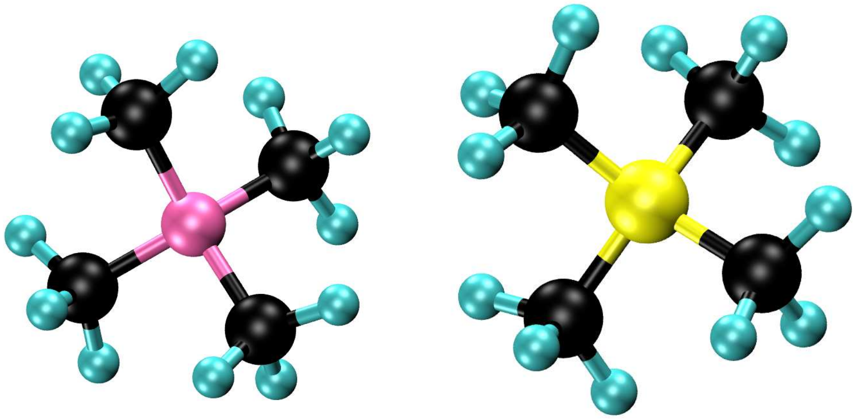

(b) Tetramethylammonium (c) Tetramethylphosphonium

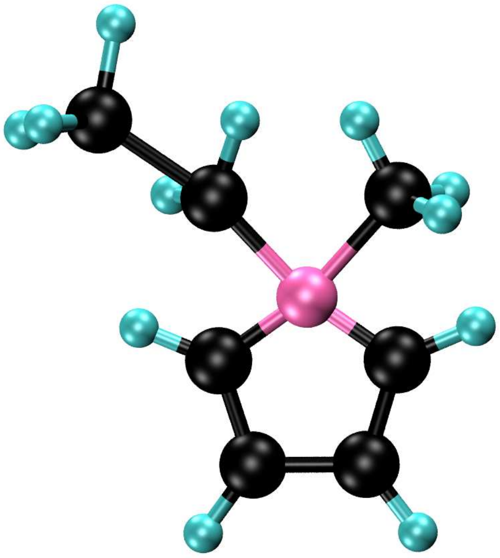

(d) N-ethyl-methylpyrrolidinium

Figure 1.3: Some of the examples for cations of room temperature ionic liquids. Colors: Nitrogen-pink, Carbon-black, Hydrogen-cyan, Phosphorus-yellow.

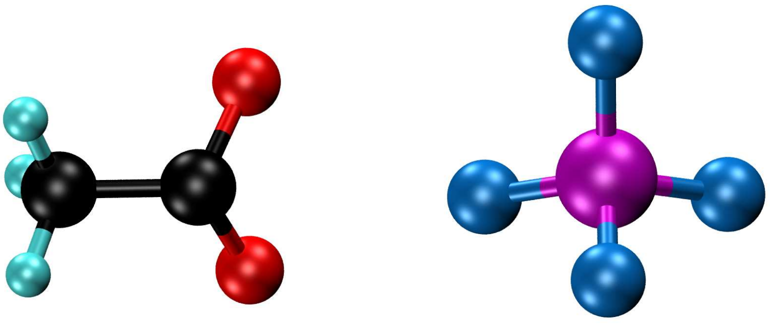

(a) Acetate $[CH_3CO_2]^-$ (b) Tetrafluoroborate $[BF_4]^-$

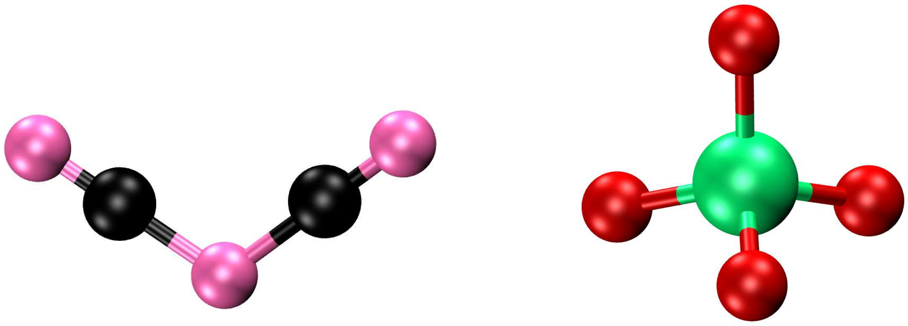

(c) Dicyanamide $[N(CN)_2]^-$ (d) Perchlorate $[ClO_4]^-$

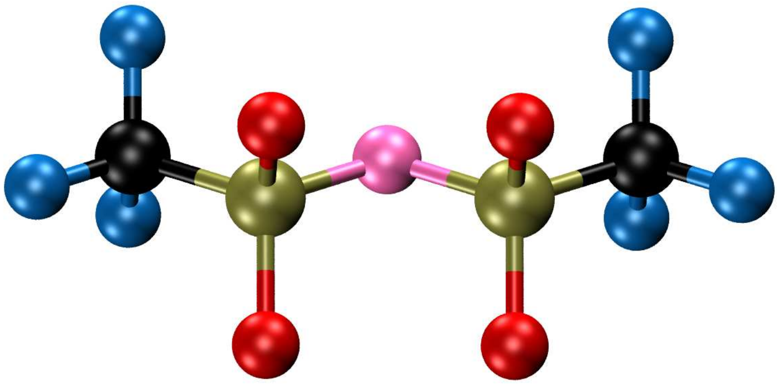

(e) bis-trifluoromethylsulphonylimide $[(CF_3SO_2)_2N]^-$

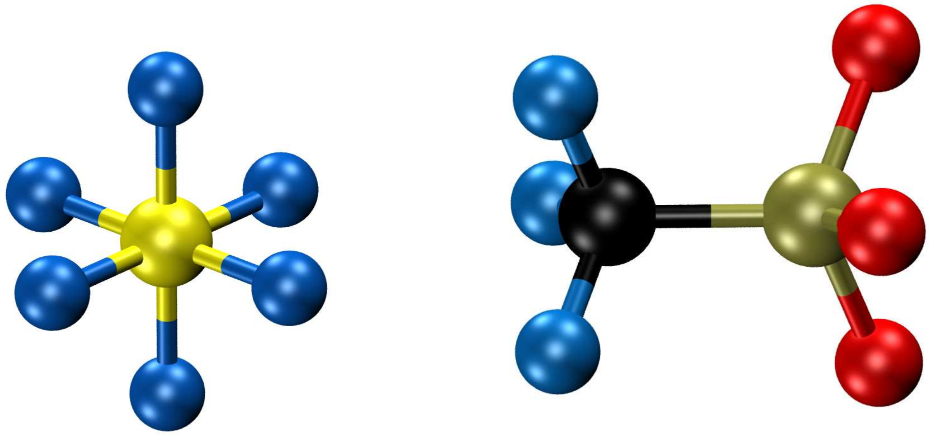

(f) Hexafluorophosphate $[PF_6]^-$ (g) Trifluoromethylsulphate $[CF_3SO_3]^-$

Figure 1.4: Some of the examples for anions of RTILs. Colors: Nitrogen-pink, Carbon-black, Hydrogen-cyan, Phosphorus-yellow, Oxygen-red, Fluorine-blue, Sulphur-tan, Chlorine-green, Boron-purple.

Ionic liquids are used to have a better kinetic control on the reactions, because they possess a wide liquidus range, ranging from 75 °C to 300 °C. The temperature range between the normal freezing point and boiling points determines the liquidus region of a solvent. Due to their narrow liquidus range, the common solvents which we come across in daily life are relatively volatile at process conditions. On the contrary, as ionic liquid is a salt, it has a negligible vapor pressure. Furthermore, they are nonflammable, can have a high thermal stability and a high ionic conductivity. These properties permit their use in many fields. Ionic liquids have been used to substitute volatile organic compounds (VOCs) as a reaction media, as homogeneous catalysis, and as an extractive media in liquid-liquid extraction processes.[4–13,15–18,27]

1.2.1 Physical and chemical properties

Ionic liquids are well known for their suitability in numerous task-specific applications, because they possess a unique set of physico-chemical properties. The notable characteristics of ionic liquidus are their negligible vapor pressure, nonflammability, thermal stability, high electrical conductivity, large electrochemical window, low nucleophilicity, capability of providing weakly coordinating environment and a good set of properties to solvate a wide variety of organic, inorganic and organometallic compounds. Further, we can design ionic liquids according to our choice; selecting a proper anion or by tuning the side chain length on the cation, we can tune the miscibility of ionic liquids with water or organic solvents. Increasing the length of an alkyl chain tends to decrease water solubility by increasing the hydrophobicity of the cation. In addition, the choice of anion can give rise to dramatic change in chemical and physical properties. For example, imidazolium salts with anions such as, acetate, nitrate, halide,trifluoroacetate are totally miscible with water, on the contrary imidazolium salts with $[(CF_3SO_2)_2N]^-$ and $[PF_6]^-$ anions are immiscible. $[BF_4]^-$ and $[CF_3SO_3]^-$ based imidazolium salts can be totally miscible or immiscible depending on the substituents on the cation.[21] The change in anion dramatically affects the chemical behavior and stability of ionic liquids while, cations have their profound effect on the physical properties. Hence, in general, the chemistry of ionic liquids are controlled by anions,[23] on the other hand the choice of cation determine the physical properties.[24]

Melting point

Most of the ionic liquids are liquid at room temperature and they have been defined to have melting points below 100 °C. Most often, it was found that the increase in anion size leads to decrease in melting point.[15] For example, the melting points of 1-ethyl-3-methylimidazolium type ionic liquids with different anions, such as $[BF_4]^-$, $[Tf_2N]^-$ and $[C_2H_5SO_4]^-$ are 15 °C, -3 °C and -20 °C, respectively.[25,26] The melting point of ionic liquids are greatly affected by the size and symmetry of the cations. Melting point of ionic liquids get reduced with large and increased asymmetric substitution at the nitrogen sites.[27] The decrease in the electrostatic energy caused by the spread of the ion charge over a larger molecular volume leads to a lowering of melting point.

Thermal stability

The stability of ionic liquids is crucial for optimum process performance in most applications. The heteroatom-carbon and heteroatom-hydrogen bonds limits the thermal stability of ionic liquids.[15] Generally, ionic liquids are found to be stable up to 500 °C. The ionic liquids 1-ethyl-3-methylimidazolium tetrafluoroborate, 1-butyl-3-methylimidazolium tetraauroborate are found to be stable up to temperatures of 445 °C and 423 °C, respectively.[28]

Viscosity

Generally, compared to common molecular solvents, ionic liquids are found to be more viscous and at room temperature, their viscosities range from 10 mPa.s to about 500 mPa.s. The hydrogen bonding and van der Waals forces determine the viscosity of ionic liquids. Energy required for molecular motion in ionic liquids increases with increase in the alkyl tail length, because of the stronger van der Waals forces between cations. Therefore, viscosity of ionic liquids increase as the alkyl tail length grows.[26] Further, the hydrogen bond formation ability of anions with the acidic proton makes an important impact on viscosity. Due to the formation of hydrogen bond complex with hydrogen bonding donors, fluorinated anions such as $[BF_4]^-$ and $[PF_6]^-$ form more viscous ionic liquids.[29] Other factors which affect viscosity of ionic liquids are the electrostatic interaction forces and the temperature. Generally, it has been found that viscosity of ionic liquids decreases with raise in temperature.[21,24,30–32]

Density

Density of ionic liquids decrease with increase in the length of the alkyl chain in the cation[50] and in general ILs are found to be more denser than water. Their density values ranges from 1 to 1.6 gm/cc. For a particular cation in an ionic liquid, the order of densities are like: $[CH_3SO_3]^- \approx [BF_4]^- < [CF_3CO_2]^- < [CF_3SO_3]^- < [C_3F_7CO_2]^- < [(CF_3SO_2)_2N]^-$.[33] Anions can also affect the density of ionic liquids. The density of 1-butyl-3-methylimidazolium type ionic liquids with anions, such as $[BF_4]^-$, $[PF_6]^-$ and $[Tf_2N]^-$ are 1.20 gm/cc, 1.37 gm/cc and 1.43 gm/cc, respectively.

Vapor pressure

Most ionic liquids have negligible vapor pressure.[34] A low vapor pressure is a direct indication of the high cohesive energy. The main reason for the low vapor pressure of ionic liquids is the presence of very strong electrostatic interactions between the ions.

Electrochemical window

Electrochemical window is the electrochemical potential range over which the electrolyte is neither reduced nor oxidized at an electrode. The electrochemical stability of a solvent is determined by this value. This property is very important in respect that it plays the key role in using ionic liquids in electrodeposition of metals and semiconductors. Water has a very low electrochemical window which is 1.2 V, due to which the electrodeposition of elements and compounds is limited in water. In contrast, the wide electrochemical window of ionic liquids have opened the door of electrodeposition of metals and semiconductors at room temperature. Some examples of large electrochemical windows in ionic liquids are: 4.15 V for [bmim][PF_6] at a platinum electrode,[35] 4.10 V for [bmim][BF_4][35] and 5.5 V for [bmpyrr][Tf_2N] at a glassy carbon electrode.[36] Elements, like Al, Mg, Si, Ge and the rare earth elements can be electrodeposited in ionic liquids. Also the thermal stability of ionic liquids allows to electrodeposit other elements, such as Ta, Nb, V, Se etc. at elevated temperature.

1.2.2 Applications

Solvents and catalysis

The non-volatile nature of room temperature ionic liquids made them to be used as environmentally friendly solvents for the chemical and pharmaceutical industries. They are the main candidates to replace the volatile organic compounds used in synthetic applications. Many reactions have been performed in ionic liquids. Diels-Alder reactions have been demonstrated in ILs, that makes the way for replacement of lithium perchlorate-diethylether mixtures.[22] Other chemical reactions, such as alkylation of sodium β-napthoxide,[37] Heck reactions,[3] Friedel-Crafts acylation,[39] electrophilic substitution reaction[40] etc. have also been demonstrated in ionic liquids. Ionic liquids offer the advantage of both homogeneous and heterogeneous catalysis for some reactions. In industrial hydroformylation and hydrogenation reactions,[41] molten tetraalkylphosphonium and ammonium salts were used as catalyst. Many homogeneous catalysis reactions have subsequently been demonstrated.[6,7,12,15,16,27,42–48]

Biocatalysis

Enzymes being stable in ionic liquids open up the possibility for ILs to be used in biological reactions, such as the synthesis of pharmaceuticals.[45,51–58,60,87] It has been found that the enzymes are relatively more stable in mixture of ILs and water, than in conventional media. In ionic liquids, the enzyme displayed exquisite stability and selectivity and their activity is equal to that observed in ethyl acetate-water. These fundamental studies of enzymes in ionic liquids have opened up a new field of nonaqueous enzymology.

Electrochemical applications

The wide electrochemical window and high electrical conductivity of ILs increased the scope of electrochemical reactions. Combination of wide liquid range and thermal stability in ILs, made them to be used as a replacement of traditional solvent-based electrolytes for a wide range of metal purification, electroplating etc. IL-based electrochemical devices, including batteries,[25,61–64] capacitors[65–67] and solar cells[68–70] have been developed.

Separations

Ionic liquids have also been used in many extraction processes. For example, [bmim][PF_6], [hmim][PF_6] and other [PF_6]$^-$ based ILs and with [Tf_2N] based ILs[71–73] have been used to extract metal ions; separation of alcohols and alkanes or alkenes was performed using [omim][Cl], [hmim][BF_4] or [hmim][PF_6],[74,75] [emim][ethyl sulfate] and [bmim][octyl sulfate] have been used in separation of trimethylamine hydrochloride/$AlCl_3$[76–79] etc.

1.3 Molecular Dynamics

Molecular dynamics[80–83] is a numerical technique which is carried out by using a model that, to a limited extent, mimics a real physical or chemical systems. It is a numerical technique to solve the classical Newton's equations of motion for computing the equilibrium and transport properties of a classical many body system. In this method particles are treated as classical particles, implies that the nuclear motion of the particles obey the laws of classical mechanics. Only when we consider the translational or rotational motion of light atoms or molecules (He, H_2, D_2) or vibrational motion with a frequency ν such that $h\nu > k_BT$ should we worry about quantum effects. The classical equations of motion for a simple atomic systems are given by;

$$m_i\ddot{\mathbf{r}}_i = \mathbf{f}_i \tag{1.1}$$

$$\mathbf{f}_i = -\frac{\partial U}{\partial \mathbf{r}_i} \tag{1.2}$$

where, $\mathbf{f}_i$ is the force acting on the ith particle, $\mathbf{r}_i$ is the position and m$_i$ is the mass of ith particle. For a system consisting of N number of particles, we need to be able to calculate the force $\mathbf{f}_i$ acting on each particle, which is derived from the potential energy $U(\mathbf{r}^N)$, where $\mathbf{r}^N = (\mathbf{r}_1, \mathbf{r}_2, ..., \mathbf{r}_N)$ represents the complete set of 3N atomic coordinates.

We can split the potential energy term $U(\mathbf{r}^N)$ into two parts, namely, bonding and non bonding interactions. $U(\mathbf{r}_{non-bonded})$ represents the non bonding interactions between atoms which is frequently split into 1-body, 2-body, 3-body ... terms;

$$U_{non-bonded}(\mathbf{r}^N) = \sum_i u(\mathbf{r}_i) + \sum_i \sum_{j>i} v(\mathbf{r}_i, \mathbf{r}_j) + ... \tag{1.3}$$

In the above expression, u($\mathbf{r}_i$) term represents the potential that is applied from externally source. The many-body interaction term generally needs to be studied with more concentration. Most often the pairwise interaction potential $v(\mathbf{r}_i, \mathbf{r}_j) = v(r_{ij})$ is given the most importance and three-body (and higher order) interactions terms have been neglected. The most commonly used pair potential is the Lennard-Jones potential.

$$v^{LJ} = 4\varepsilon \left[\left(\frac{\sigma}{r}\right)^{12} - \left(\frac{\sigma}{r}\right)^{6} \right] \tag{1.4}$$

The Lennard-Jones potential has two important parameters: σ, the diameter, and ε, the well depth. For molecular systems, we must also consider the intramolecular interactions. These bonded interactions are the different bond stretches, angle flexing and torsional terms. The intramolecular potential energy can be written as,

$$\begin{aligned} U_{intramolecular} &= \frac{1}{2}\sum_{bonds} k^r_{ij}(r_{ij} - r_{eq})^2 + \frac{1}{2}\sum_{angles} k^\theta_{ijk}(\theta_{ijk} - \theta_{eq})^2 \\ &+ \frac{1}{2}\sum_{torsion}\sum_{m} k^{\phi,m}_{ijkl}(1 + cos(m\phi_{ijkl} - \gamma_m)) \end{aligned} \tag{1.5}$$

The electrostatic interactions are exploited using the Coulomb potential. Most of the time, a single molecule quantum-chemical calculation is performed to have an estimation of the electron density throughout the whole system. These partial charge distribution is then modelled as under:

$$v^{Coulomb}(r) = \frac{Q_1 Q_2}{4\pi\varepsilon_0 r} \tag{1.6}$$

Force field refers to the functional form and set of parameters that describe the potential energy of a system to perform classical molecular dynamics simulations. Hence, a force field will contain the exact form of Eq.(1.5), and the various strength parameters k and the other constants, such as equilibrium bond length, equilibrium angle etc. Once we have the precise form of potential energy function $U(\mathbf{r}^N)$, next step is to calculate the forces acting on each atom using Eq.(1.2).

Now, consider a system consist of N number of particles, with their atomic coordinates $\mathbf{r}^N = (\mathbf{r}_1, \mathbf{r}_2, ..., \mathbf{r}_N)$ and the atomic momenta $\mathbf{p}^N = (\mathbf{p}_1, \mathbf{p}_2, ..., \mathbf{p}_N)$. The kinetic energy would then be given by, $K(p^N) = \sum_{i=1}^{N} |p_i|^2/2m_i$. Now, we know energy or the Hamiltonian of a system is just the sum of kinetic energy and potential energy, $H = K + U$. Therefore, the Hamiltonian $H(\mathbf{r}^N, \mathbf{p}^N)$ is represented as,

$$H(\mathbf{r}^N, \mathbf{p}^N) = U(\mathbf{r}^N) + \sum_{i=1}^{N} |p_i|^2/2m_i \tag{1.7}$$

Then the Hamilton's equations for this system is given as,

$$\dot{\mathbf{r}}_i = \frac{(\partial H)}{(\partial \mathbf{p}_i} = \frac{\mathbf{p}_i}{m_i} \tag{1.8}$$

$$\dot{\mathbf{p}}_i = -\frac{(\partial H)}{(\partial \mathbf{r}_i} = \mathbf{f}_i \tag{1.9}$$

Thus, given the initial positions and momenta of the particles, these coupled equations of motion need to be integrated numerically to determine $\mathbf{r}_i$ and $\mathbf{p}_i$ as a function of time. Finite difference method is generally used to solve these set of equations. The simple procedure is as follows. From the initial particle positions, velocities at time t, we have to derive the position, velocities at a later time $t + \delta t$. The equations are solved on a step-by-step basis; the choice of the time interval δt must be chosen relevantly. Most important criteria is that it should be much smaller than the fastest process occurring in the system. While choosing larger time steps, accuracy of numerical integration should not be lost. To handle systems involving interactions of multiple time scales efficiently, multiple time step algorithms have been developed. In these algorithms the short-range forces, which requires small integration time step are treated very frequently in time. On the other hand, the non-bonded interactions are treated with larger time step and less frequent force evaluations.

To solve the equations of motion over time several algorithms have been developed. For example, position Verlet[84,85] algorithm, Leap-Frog algorithm[86] , velocity Verlet[87] algorithm, Gear predictor-corrector algorithm etc. Most simple and efficient among these algorithms is the velocity Verlet algorithm. The velocity Verlet algorithm can be represented as

$$\boldsymbol{p}_i(t + \frac{1}{2}\delta t) = \boldsymbol{p}_i(t) + \frac{1}{2}\delta t \boldsymbol{f}_i(t) \tag{1.10}$$

$$\boldsymbol{r}_i(t + \delta t) = \boldsymbol{r}_i(t) + \delta t \boldsymbol{p}_i(t + \frac{1}{2}\delta t)/m_i \tag{1.11}$$

$$\boldsymbol{p}_i(t + \delta t) = \boldsymbol{p}_i(t + \frac{1}{2}\delta t) + \frac{1}{2}\delta t \boldsymbol{f}_i(t + \delta t) \tag{1.12}$$

In velocity Verlet algorithm, the volume of phase space is always conserved. It permits long timesteps, because it is lower order in time. Most importantly, it is least expensive as it requires only one force evaluation per step.

1.3.1 Long-range interactions

For a n-dimensional system, the long-range potential is defined as one in which the interaction decays slower than r^{-n}. In this potential, significant contribution to the total potential energy exist even for distances greater than the interaction cutoff distance. The charge-charge interaction or the Coulombic interaction, which decays as r^{-1} falls under this category. In a simulation of charged species, such as molten salts, it is important to calculate these long-range forces properly. One way to solve these problems is to increase the number of particles (N) resulting in a much larger simulation cell, so that screening by neighbors could decrease the range of interaction. But as we know that, the molecular dynamics simulation is a O(N^2) problem, the resulting computational cost would be very high. Hence, methods have been developed to exactly treat the long-range nature of the electrostatic interactions. Ewald summation method is very popular among the methods.

The Ewald sum is a lattice sum method, which includes the interaction of a particle with all other particles in the system and their periodic images. For a simulation box, which is positioned at a cubic lattice point $\mathbf{n}$ $(= (n_xL, n_yL, n_zh)$ with n_x, n_y, n_z being integers): the charge-charge contribution to the total potential energy due to all pairs of charges in the central simulation box can be expressed as :

$$V = \frac{1}{2} \sum_{|\mathbf{n}|=0}^{\prime} \sum_{i=1}^{N} \sum_{j=1}^{N} \frac{q_i q_j}{4\pi\epsilon_o |\mathbf{r}_{ij} + \mathbf{n}|} \tag{1.13}$$

Here, in this expression the interaction $i = j$ for $\mathbf{n} = 0$ has been neglected by the prime on the first summation. This summation is conditionally convergent and also it converges very slowly. We can convert the summation like the Eq.(1.14), such that it converges much more rapidly.

$$\frac{1}{r} = \frac{f(r)}{r} + \frac{1-f(r)}{r} \tag{1.14}$$

In the Ewald summation method, a neutralizing charge distribution of equal magnitude but of opposite sign is considered around each point charge. Most often a Gaussian charge distribution is used of following form.

$$\rho_i(\mathbf{r}) = \frac{q_i \alpha^3}{\pi^{3/2}} exp(-\alpha^2 r^2) \tag{1.15}$$

Now the total sum is consists of interactions between the point charges plus the neutralizing distributions. Hence, the real space summation becomes as;

$$V = \frac{1}{2} \sum_{i=1}^{N} \sum_{j=1}^{N} \sum_{|\mathbf{n}|=0}^{\prime} \frac{q_i q_j}{4\pi\epsilon_o} \frac{erfc(\alpha|\mathbf{r}_{ij} + \mathbf{n}|)}{|\mathbf{r}_{ij} + \mathbf{n}|} \tag{1.16}$$

where, erfc is the complementary error function, which is given by:

$$erfc(x) = \frac{2}{\sqrt{\pi}} \int_{x}^{\infty} exp(-t^2) dt \tag{1.17}$$

In the Ewald method, erfc(r) replaces the function f(r) in Eq.(1.14). Now, this new summation consisting of the error function converges very fast and beyond some cutoff distance, its value is negligible. This series converges faster as the width of the Gaussian (α) becomes wider. A second charge distribution is now added to the system which exactly counteracts the first neutralizing distribution. The contribution from this second charge distribution is:

$$V = \frac{1}{2} \sum_{k \neq 0} \sum_{i=1}^{N} \sum_{j=1}^{N} \frac{1}{\pi L^3} \frac{q_i q_j}{4\pi\epsilon_o} \frac{4\pi^2}{k^2} exp\left(-\frac{k^2}{4\alpha^2}\right) cos(\mathbf{k}.\mathbf{r}_{ij}) \tag{1.18}$$

The real space summation now converges more rapidly with large α, whereas in reciprocal space it converges rapidly for small value of α. Hence, there should be some balance between them. There is one more term that takes care of the interactions between each gaussian with itself in real space.

$$V = -\frac{\alpha}{\sqrt{\pi}} \sum_{k=1}^{N} \frac{q_k^2}{4\pi\epsilon_o} \tag{1.19}$$

One more correction term is needed for accounting the medium surrounding the simulation box. The correction term for a medium of relative permitivity of 1 is:

$$V_{correction} = \frac{2\pi}{3L^3} \left| \sum_{i=1}^{N} \frac{q_i}{4\pi\epsilon_o} \mathbf{r}_i \right|^2 \tag{1.20}$$

The Ewald sum is the summation of equations (1.16,1.18,1.19,1.20). This sum is very expensive as it scales as N^2. To speed up this summation FFT methods are being implemented which requires a grid-based charge distribution. Various FFT algorithm have been developed for this purpose. These include the particle-mesh Ewald method[88] and the particle-particle-particle-mesh approach.[89]

1.3.2 Periodic boundary condition

In a three-dimensional N-particle system with free boundaries, the fraction of molecules which stays at the surface is proportional to $N^{-1/3}$. To get rid off the surface effects on the system, the simulation cell is replicated periodically in all dimensions. For instance, particles in a cubic box are replicated in all directions to give a periodic array. In three dimensions each box would have 26 nearest neighbors. During the course of simulation, if a particle moves out of the cell, its periodic image from the neighboring cell enters into it and in the central box the number density remains conserved. Hence, the force calculation becomes of the order of N^2 after implementing the minimum image convention. Minimum image convention takes care that every particle interacts with the closest atoms or the images from the periodic array. The numbers of bonded terms, such as bond-stretching, angle-bending and torsional terms are all proportional to the number of atoms in a simulation cell. But the non-bonded interaction terms (for a pairwise model) in a force field are proportional to square of the numbers of atoms. In general, non-bonded interactions are calculated between every pair of atoms in the systems. Therefore, in a molecular dynamics simulation, the most time-consuming part is the calculation of the non-bonded energies. When a cutoff distance is applied, the interactions between all pairs of atoms that are separated than the cutoff value are set to zero, taking into account the closest image. Under periodic boundary conditions, the cutoff distance should not be so large that particle sees its own image. This has the effect of limiting the cutoff to no more than half the length of the simulation cell.

1.4 Analysis

For a system with a given initial configuration, molecular dynamics simulation would provide a trajectory (positions and velocities of all the atoms as a function of time) in the phase space in the appropriate ensemble. We can study the structural and dynamical properties of the system using this trajectory. For a liquid to study its structure, the most useful technique to use is the radial distribution function or the pair distribution functions g(r). It gives the probability of finding a particle at a distance r from another particle compared to the ideal gas distribution.Thus, it is thus. To calculate the g(r), configurations are read and the minimum image separation r_{ij} of all the pairs of atoms are calculated. These separations are sorted into a histogram where each bin has a width δr and extends from r to $r + \delta r$. After all the configurations have been processed, the histogram is normalized to calculate g(r). Suppose there are τ steps on the tape, and a particular bin b of the histogram, corresponding to the interval $(r, r + \delta r)$, contains $n_{his}(b)$ pairs. Then the average number of atoms whose distance from a given atom lies in this interval, is

$$n(b) = n_{his}(b)/(N \times \tau) \tag{1.21}$$

The average number of atoms in the same interval in an ideal gas at the same density ρ is

$$n^{id}(b) = \frac{4\pi\rho}{3}[(r+\delta r)^3 - r^3] \tag{1.22}$$

By definition, the radial distribution function is

$$g(r + \frac{1}{2}\delta r) = n(b)/n^{id}(b) \tag{1.23}$$

1.5 *Ab initio* Molecular Dynamics

A wide variety of systems including gaseous and condensed phase systems have been studied by using the classical molecular dynamics simulation. In these simulations, for a particular system, the empirical potential has to be determined. The form of the potential approximates the intermolecular interactions between the atoms, that usually includes pairwise interactions, three body and many body interactions. The experimental results and the *ab initio* calculations are used to determine these potential parameters and also these parameters are fixed throughout the course of simulation.

The main drawback of the classical molecular dynamics is that the results will be as good as the model used. To obtain a very good result, one should have a very good model of the system that could describe the system accurately. For a new system with complex intermolecular interactions, the form of the interactions and the potential parameters need to be determined. Transferability of these potentials is also a main issue.

Ab initio molecular dynamics successfully combines the traditional molecular dynamics and the electronic structure methods.[90–100] These *ab initio* calculations involves the quantum part that deals with electronic degrees of freedom and the classical dynamics of ions. *Ab initio* method relies on the Born-Oppenheimer approximation that separates the electronic and ionic degrees of freedom based on the difference in the masses between the electron and the ions. These methods are based on the Kohn-Sham formulation of DFT, and uses pseudopotentials to represent the interaction of valence electrons with the core electrons and the nuclei. The potential of interaction between the ions continuously changes with time. Here, electronic degrees of freedom are taken into account that gives a better microscopic picture of the system.

According to the Blöch theorem,[101] each electronic wave function can be expressed as a sum of plane waves

$$\psi_i(\vec{r}) = \sum_k C_k^i e^{\vec{k}.\vec{r}} \tag{1.24}$$

where, the coefficients of expansion are C_k^i's. Thus the electronic configuration can be expressed by a complete set of coefficients, (C_{k1}^1, ..., C_{kmax}^1, ..., C_{k1}^n, ..., C_{kmax}^n), denoted by C. Then the minimization process start searching in the space of all possible C for C_{opt}, such that $E(C_{opt})$, the electronic energy, is minimum energy for all C.

1.5.1 Plane waves

For solids, and in general condensed phases, Blöch's theorem[101] suggests that the wave function is composed of a phase factor and a periodic part, such that it verifies $u_{\mathbf{k}}(\mathbf{r}) = u_{\mathbf{k}}(\mathbf{r} + \mathbf{a}_i)$, where the lattice is $\mathbf{a}_i$. Here, the periodic potential is generated by the underlying lattice and thus it imposes the same periodicity on the density. Thus, in order to expand the periodic part of the orbitals, plane waves are prescribed to be used as the generic basis set. Hence, this can be used to introduce naturally the basis set of plane waves (PW).[102–107]

Any function in real space, in general, can be expressed as the Fourier transform of a function in reciprocal space,

$$u_{\mathbf{k}}(\mathbf{r}) = \int e^{i\mathbf{g}.\mathbf{r}} \tilde{u}_{\mathbf{k}}(\mathbf{g}) d\mathbf{g} \tag{1.25}$$

Here, the periodicity of $u_{\mathbf{k}}(\mathbf{r})$ imposes the constraint on the values of $\mathbf{g}$, the values of $\mathbf{g}$ becomes those, that verify $e^{i\mathbf{g}.\mathbf{a}_j} = 1$, i.e. $\mathbf{g}.\mathbf{a}_j = 2n\pi$ for $j = 1, 2, 3$ - the three lattice vectors. Therefore, the $\mathbf{g}$ vectors in the Fourier transform (1.25) are restricted to the reciprocal lattice vectors $\mathbf{G}$. The general expression of wave function is:

$$\varphi^{(\mathbf{k})}(\mathbf{r}) = \frac{e^{i\mathbf{k}.\mathbf{r}}}{\sqrt{\Omega}} \sum_{\mathbf{G}=\mathbf{0}}^{\infty} C_{\mathbf{k}}(\mathbf{G}) e^{i\mathbf{G}.\mathbf{r}} \tag{1.26}$$

Here, the Fourier coefficients are $C_{\mathbf{k}}(\mathbf{G})$. Now, the plane wave basis functions are defined as

$$\phi_{\mathbf{G}}(\mathbf{r}) = \frac{1}{\sqrt{\Omega}} e^{i\mathbf{G}.\mathbf{r}} \tag{1.27}$$

where the normalization is simply given by $\frac{1}{\sqrt{\Omega}}$; Ω is the volume of the periodic super-cell. Now, we can see that these plane waves are normalized in the supercell

$$\langle \phi_{\mathbf{G}} | \phi'_{\mathbf{G}} \rangle = \frac{1}{\Omega} \int_{\Omega} e^{i(\mathbf{G}-\mathbf{G}').\mathbf{r} d\mathbf{r}} = \frac{1}{\Omega} (\Omega \delta_{\mathbf{G},\mathbf{G}'}) = \delta_{\mathbf{G},\mathbf{G}'} \tag{1.28}$$

so that plane waves becomes orthogonal those corresponds to different wave vectors, $\mathbf{G} \neq \mathbf{G}'$. Also, the plane wave coefficients can be expressed in terms of the real-space wave functions;

$$C_{j\mathbf{k}}(\mathbf{G}) = \int_{\Omega} \phi_{\mathbf{G}}^{\mathbf{k}*}(r) \varphi_j^{\mathbf{k}}(\mathbf{r}) d\mathbf{r} = \frac{1}{\sqrt{\Omega}} \int_{\Omega} e^{-i(\mathbf{k}+\mathbf{G}).\mathbf{r}} \varphi_j^{\mathbf{k}}(\mathbf{r}) d\mathbf{r}. \tag{1.29}$$

According to Blöch theorem, in periodic potential, we can expand the wave function of an electron in a plane wave basis set. In the plane wave expansion the

G vectors are the reciprocal lattice vectors, in principle, we need infinite number of them to represent the wave functions with infinite accuracy. However, with the increase in $|\mathbf{k}+\mathbf{G}|$, the Fourier coefficients $C_{\mathbf{k}}(\mathbf{G})$ of the wave functions decreases, hence, we can effectively truncate the plane wave expansion at a finite number of terms, i.e. limited to all waves with kinetic energy lower than some cutoff energy E_{cut}:

$$\frac{\hbar^2}{2m}|\mathbf{k}+\mathbf{G}|^2 < E_{cut} \tag{1.30}$$

For the Γ-point ($\mathbf{k} = 0$), the G_{cut} value is given by

$$|\mathbf{G}| < G_{cut} = \sqrt{\frac{2mE_{cut}}{\hbar^2}} \tag{1.31}$$

The computed physical quantities an be erroneous because of this truncation of basis set. But we can easily get rid of this error by increasing the cutoff (E_{cut}). This implies that, without the modification of the Hamiltonian there is an increase in basis set. Hence, the energy should decrease variationally with increasing E_{cut}.

1.5.2 Pseudopotential

The electronic states of an atom can be classified into: (1) *core states*, a highly localized state that do not involve in chemical bonding, (2) *valence states*, these states are mainly responsible for the chemical bonding, and (3) *semi-core states*, there are no direct contribution from these states in chemical bonding, mostly localized and polarizable states. Most of the chemistry is determined by the valence electrons, whereas the core electrons are essentially inert. Hence, for the fundamental description of chemical bonding, it is not strictly necessary to have precise description of valence wave function inside the core region. In practice, this means that, we can take out the innermost electrons from the explicit calculations. In this approach,

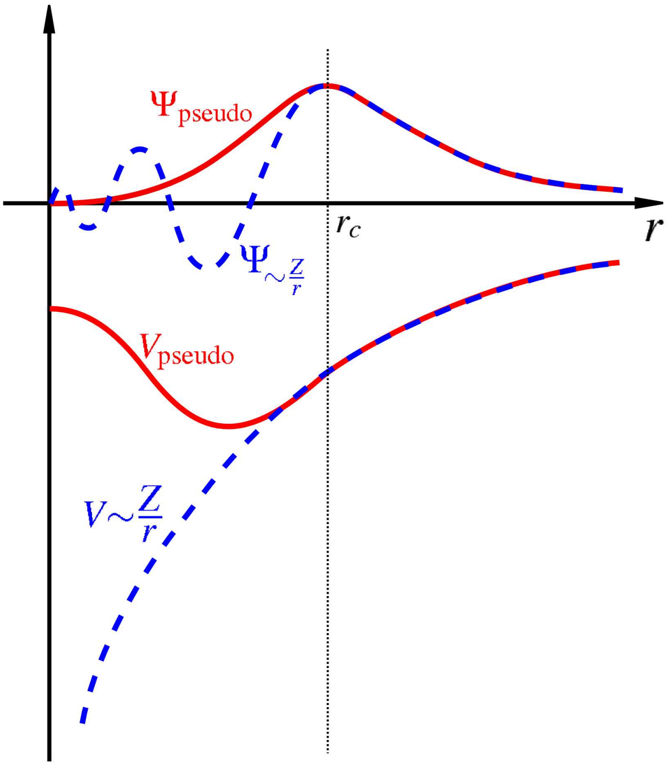

Figure 1.5: Comparison of a wavefunction in the Coulomb potential of the nucleus (blue) to the one in the pseudopotential (red). The real and the pseudo wavefunction and potentials match above a certain cutoff radius r_c.[135]

if we replace the inner solution (< cutoff radius) with a smooth, nodeless pseudowavefunction, we are not going to lose any crucial information. Therefore, in a practical sense, it becomes pseudo-atomic problem, where a *pseudopotential*[74,75,106–114] is used to replace the true potential.

The pseudo wave function solution obtained from the pseudopotentials approaches to the full wave function outside the chosen core radius r_c. It is required that, the pseudopotentials would be able to represent the long-range interactions of core electrons correctly. In order to have a small plane wave cutoff, the pseudopotential and the wave function should be as smooth as possible inside the cutoff distance. Transferability of the pseudopotentials is also expected, thus in different chemical environments the same pseudopotential would be able to produce same results of comparable accuracy.

The most practical and accurate pseudopotential was constructed once the norm conservation in pseudopotential has been implemented. In a norm-conserving pseudopotential, inside the core region the normalization of the pseudo wave function is being conserved. Hence, outside the core state, this wave function resembles that of the all-electron atom as closely as possible. The replacement of electronic degrees of freedom in the Hamiltonian by pseudopotential leads to a considerable reduction of the basis set as well as the number of electrons in the systems. Therefore, this allows for faster calculation or the treatment of larger systems.

1.5.3 Atom-centered basis sets

For molecular systems, there appears electrostatic interaction between periodic images in adjacent cells if dipole moment exists for that system. Because the dipole-dipole interactions decay as R^{-3}, and in plane wave scheme the periodic boundary condition are automatically embedded. Therefore, one has to choose a sufficiently large simulation cell to minimize this effect, which in turn increases the number of plane waves unnecessarily. Hence, plane wave methodology is not the most efficient one for molecular systems. For these kind of systems localized basis set are much better because they can be normally tuned to reproduce atomic wave functions.[106,107]

In quantum chemistry or molecular physics, it is very much popular of using *atomic orbitals* (AOs) to expand one-electron wave functions, or the *molecular orbitals* (MOs). Basis functions with different functional forms can be used to represent these AOs; most importantly these AOs are centered on the atomic nuclei. For a single atomic center,it is easier to construct as orthogonal basis. Naturally a multi-center expansion is always better choice, where basis functions centered on each atom in the molecule are used to construct the basis sets. A natural consequence of this approach is to have the information about the characteristics of the electronic distributions.

1.5.4 Hohenberg-Kohn's theorem and Kohn-sham formulation of DFT

Hohenberg-Kohn (HK) theorem[117–119] is at the heart of DFT. According to this theorem: in principle, it is possible to calculate the *ground-state* wave function $\Psi_0(\mathbf{r_1}, \mathbf{r_2}, ..., \mathbf{r_N})$ from a given ground-state density $n_0(\mathbf{r})$. It implies that, Ψ_0 is a functional of n_0. Hence, all the other ground-state observables are also becomes functional of n_0. Both functions, Ψ_0 and n_0 are equivalent and contain exactly the same information. Thus, the ground-state wave function Ψ_0 reproduces the ground-state density and also minimizes the energy. For a given ground-state density $n_0(r)$, we can define this requirement as

$$E_{v,0} = \min_{\Psi \to n_0} \langle \Psi | \hat{T} + \hat{U} + \hat{V} | \Psi \rangle, \tag{1.32}$$

where $E_{v,0}$ denotes the ground-state energy in potential $v(\mathbf{r})$. The preceding equation tells us that for a given density $n_0(\mathbf{r})$ the ground-state wave function Ψ_0 is that which reproduces this $n_0(\mathbf{r})$ and minimizes the energy. For an arbitrary density $n(\mathbf{r})$, we define the functional

$$E_v[n] = \min_{\Psi \to n} \langle \Psi | \hat{T} + \hat{U} + \hat{V} | \Psi \rangle, \tag{1.33}$$

If n is a density different from the ground-state density n_0 in potential $v(\mathbf{r})$, then the that produce this n are different from the ground-state wave function Ψ_0, and according to the variational principle the minimum obtained from $E_v[n]$ is higher than (or equal to) the ground-state energy $E_{v,0} = E_v[n_0]$. Thus, the functional $E_v[n]$ is minimized by the ground-state density n_0, and its value at the minimum is $E_{v,0}$. Kohn and Sham then showed that it is possible to map a many body problem by an exactly equivalent set of self consistent one electron equations, known as Kohn-Sham orbital. For a doubly occupied electronic states ψ_i the Kohn-Sham total energy functional can be expressed as;

$$E_{KS}\Big[\{\psi_i(\mathbf{r})\}\Big] = \sum_i f_i \int \psi_i^*(\mathbf{r})\left(\frac{-\hbar^2}{2m}\right)\nabla^2\psi_i(\mathbf{r})d^3\mathbf{r} + \frac{e^2}{2}\iint \frac{\rho(\mathbf{r_1})\rho(\mathbf{r_2})}{|\mathbf{r_1}-\mathbf{r_2}|}d^3\mathbf{r_1}d^3\mathbf{r_2} + \int \varepsilon_{XC}\{\rho(\mathbf{r})\}\rho(\mathbf{r})d\mathbf{r} + E_{eI}([\psi_i(\mathbf{r})],\{R_I\}) + U_I^O(\{R_I\}). \tag{1.34}$$

Here, on the right hand side, the first term is the kinetic energy of electrons, the second term represents electron-electron Coulomb energy, the third term corresponds to electron exchange correlation energy, the electron-ion interaction energy is given in the fourth term and the last term stands for ion-ion interaction. The electron density $\rho(\mathbf{r})$ is given by

$$\rho(\mathbf{r}) = \sum_i |\psi_i(\mathbf{r})|^2 \tag{1.35}$$

The ionic potential energy for the electrons can be obtained once after the minimization of E_{KS} with respect to single particle wave function. There are a large number of optimization algorithm reported in literature. In our calculations, most often we used the Broyden-Fletcher-Goldfarb-Shanno (BFGS)[120–125] numerical optimization method.

1.6 Softwares used

All the classical molecular dynamics simulations reported in the thesis were carried out using the LAMMPS[80] software. The *ab initio* molecular dynamics calculations/simulations were performed by the extensive use of CP2K[73] and CPMD[33] softwares. During the course of research, codes were developed for the calculation of structural and dynamical properties presented in the thesis. Some of the structure optimization, vibrational analysis and computations of binding energies were performed using the Gaussian09[32] software. Xmgrace, qtiplot and g3data softwares were used for plotting. Visualizations and some analysis were done with the visualization softwares VMD,[43] JMOL,[41,42] Mercury.[40] All the softwares used, except for Gaussian are freely available.

Bibliography

[1] **“Supply of Uranium”.** World Nuclear Association. Retrieved 29 January 2010.

[2] **“Fast Neutron Reactors”.** World Nuclear Association. Retrieved 11 March 2012.

[3] D. R. Lide, *Handbook of chemistry and physics.,* **72**, 1391 (2000).

[4] P. Wasserscheid, T. Welton (eds.), *Ionic Liquids in Synthesis*, (Wiley-VCH Verlag GmbH & Co. KGaA, Weinheim, 2003).

[5] R.D. Rogers, K.R. Seddon, S. Volkov (eds.), *Green Industrial Applications of Ionic Liquids*, (Kluwer Academic Publishers, Dordrecht, 2002).

[6] R.D. Rogers, K.R. Seddon (eds.), *Ionic Liquids. Industrial Applications to Green Chemistry*, (American Chemical Society, Washington, 2002).

[7] R.D. Rogers, K.R. Seddon (eds.), *Ionic Liquids as Green Solvents. Progress and Prospects*, (American Chemical Society, Washington, 2003).

[8] R.D. Rogers, K.R. Seddon (eds.), *Ionic Liquids IIIA: Fundamentals, Progress, Challenges, and Opportunities. Properties and Structure*, (American Chemical Society, Washington, 2005).

[9] R.D. Rogers, K.R. Seddon (eds.), *Ionic Liquids IIIB: Fundamentals, Progress,*

Challenges, and Opportunities. Transformations and Processes, (American Chemical Society, Washington 2005).

[10] K.R. Seddon, *J. Chem. Tech. Biotechnol.*, **68**, 351 (1997).

[11] K.R. Seddon, *Molten Salt Forum*, **5-6**, 53 (1998).

[12] J.G. Huddleston, H.D. Willauer, R.P. Swatloski, A.E. Visser, R.D. Rogers, *Chem. Commun.*, **16**, 1765 (1998).

[13] M. Freemantle, *Chem. Eng. News*, **76**, 32 (1998).

[14] J.D. Holbrey, K.R. Seddon, *Clean Prod. Proc.*, **1**, 223 (1999).

[15] P. Wasserscheid, W. Keim, *Angew. Chem. Int. Ed.*, **39**, 3772 (2000).

[16] C.M. Gordon, *Appl. Catal. A*, **222**, 101 (2001).

[17] J.F. Brennecke, E.J. Maginn, *AIChE Journal*, **47**, 2384 (2001).

[18] J. Dupont, C.S. Consorti, J. Spencer, *J. Braz. Chem. Soc.*, **11**, 337 (2000).

[19] A.G. Fadeev, M.M. Meagher, *Chem. Commun.*, 295 (2001).

[20] Q. Liu, M. H. A. Janssen, F. van Rantwijk, R. A. Sheldon, *Green Chem.,* **7**, 39 (2005).

[21] K.R. Seddon, A. Stark, M.J. Torres, *Pure Appl. Chem.*, **72**, 2275, (2000).

[22] M.J. Earle, P.E. McCormac, K.R. Seddon, *Green Chem.*, **1**, 23 (1999).

[23] M.J. Earle, S.P. Katdare, K.R. Seddon, *Org. Lett.*, **6**, 707 (2004).

[24] K.R. Seddon, A. Stark, M.J. Torres *Viscosity and density of 1-alkyl-3-methylimidazolium ionic liquids*, in M. Abraham, L. Moens (eds.): *Clean Solvents: Alternative Media for Chemical Reactions and Processing*, (ACS Symp. Ser., Vol. 819, American Chemical Society, Washington D.C. 2002)

[25] J. Fuller, R.T. Carlin, R.A. Osteryoung, *J. Electrochem. Soc.*, **144**, 3881 (1997).

[26] P. Bonhote, A.P. Dias, N. Papageorgiou, K. Kalyanasundaram, M. Gratzel, *Inorg. Chem.*, **35**, 1168 (1996).

[27] J.D. Holbrey, R.D. Rogers, *Physiochemical Properties of Ionic Liquids*, in P.Wasserscheid, T. Welton (eds.), *Ionic Liquids in Synthesis*, (Wiley-VCH, Weinheim 2003).

[28] M.E. van Valkenburg, R.L. Vaughn, M. Williams, J.S. Wilkes, *Thermochim. Acta*, **425**, 181 (2005).

[29] P.A.Z. Suarez, S. Einloft, J.E.L. Dullius, R.F. De Souza, J. Dupont, *J. Chim. Phys. Phys.-Chim. Biol.*, **95**, 1626 (1998).

[30] S.V. Dzyuba, R.A. Bartsch, *ChemPhysChem*, **3**, 161 (2002).

[31] O.O. Okoturo, T.J. VanderNoot, *J. Electroanal. Chem.*, **568**, 167 (2004).

[32] P. Wasserscheid, R. Van Hal, A. Bosmann, *Green Chem.*, **4**, 400 (2002).

[33] R.A. Mantz, P.C. Trulove, *Viscosity and Density of Ionic Liquids*, in P. Wasserscheid, T. Welton (eds.), *Ionic Liquids in Synthesis*, (Wiley-VCH, Weinheim 2003).

[34] R.D. Rogers, K.R. Seddon, *Science,* **302,** 792 (2003).

[35] U. Shroder, J.D. Wadhawan, R.G. Compton, F. Marken, P.A.Z. Suarez, C.S. Consorti, R.F. de Souza, J. Dupont, *New J. Chem.*, **24**, 1009 (2000).

[36] D.R. MacFarlane, P. Meakin, J. Sun, N. Amini, M. Forsyth, *J. Phys. Chem. B*, **103**, 4164 (1999).

[37] M. Badri, J.J. Brunet, R. Perron, *Tetrahedron Lett.*, **33**, 4435 (1992).

[38] T. Welton, *Chem. Rev.*, **99**, 2071 (1999).

[39] C.J. Adams, M.J. Earle, G. Roberts, K.R. Seddon, *Chem. Commun.*, 2097 (1998).

[40] J.A. Boon, J.A. Levisky, J.L. Pflug, J.L. Wilkes, *J. Org. Chem.*, **51**, 480 (1986).

[41] G.W. Parshall, *J. Am. Chem. Soc.*, **94**, 8716 (1972).

[42] 133. H. Olivier-Bourbigou, L. Magna, *J. Mol. Catal. A: Chem.*, **182-183**, 419 (2002).

[43] N.L. Lancaster, T. Welton, G.B. Young, *J. Chem. Soc., Perkin Trans.*, **2**, 2267 (2001).

[44] N.L. Lancaster, P.A. Salter, T. Welton, G.B. Young, *J. Org. Chem.*, **67**, 8855 (2002).

[45] R. Sheldon, *Chem. Commun.*, 2399 (2001).

[46] J. Dupont, R.F. de Souza, P.A.Z. Suarez, *Chem. Rev.*, **102**, 3667 (2002).

[47] D.B. Zhao, M. Wu, Y. Kou, E. Min, *Catal. Today*, **74**, 157 (2002).

[48] C.E. Song, *Chem. Commun.*, 1033 (2004).

[49] P.J. Dyson, *Appl. Organomet. Chem.*, **16**, 495 (2002).

[50] K.N. Marsh, J.A. Boxall, R. Lichtenthaler, *Fluid Phase Equilib.*, **219**, 93 (2004).

[51] A.J. Walker, N.C. Bruce, *Chem. Commun.*, **22**, 2570 (2004).

[52] R.A. Sheldon, R.M. Lau, M.J. Sorgedrager, F. van Rantwijk, K.R. Seddon, *Green Chem.*, **4**, 147 (2002).

[53] F. van Rantwijk, R.M. Lau, R.A. Sheldon, *Trends Biotechnol.*, **21**, 131 (2003).

[54] S.G. Cull, J.D. Holbrey, V. Vargas-Mora, K.R. Seddon, G.J. Lye, *Biotechnol. Bioeng.*, **69**, 227 (2000).

[55] R.M. Lau, F. van Rantwijk, K.R. Seddon, R.A. Sheldon, *Org. Lett.*, **2**, 4189 (2000).

[56] M. Erbeldinger, A.J. Mesiano, A.J. Russell, *Biotechnol. Prog.*, **16**, 1129 (2000).

[57] S. Park, R.J. Kazlauskas, *Curr. Opin. Biotech.*, **14**, 432 (2003).

[58] U. Kragl, M. Eckstein, N. Kaftzik, *Curr. Opin. Biotech.*, **13**, 565 (2002).

[59] M.Y. Lee, J.S. Dordick, *Curr. Opin. Biotech.*, **13**, 376 (2002).

[60] H.S. Schofer, N. Kaftzik, P. Wasserscheid, U. Kragl, *Chem. Commun.*, 425 (2001)

[61] C.L. Hussey, T.B. Scheffler, J.S. Wilkes, A. Fannin Jr., *J. Electrochem. Soc.*, **133**, 1389 (1986).

[62] T. Ito, T. Nohira, *Electrochim. Acta*, **45**, 2611 (2000).

[63] R.T. Carlin, H.C. De Long, J. Fuller, P.C. Trulove, *J. Electrochem. Soc.*, **141**, L73 (1994).

[64] D.R. MacFarlane, J. Huang, M. Forsyth, *Nature*, **402**, 792 (1999).

[65] A. Lewandowski, A. Swiderska, *Solid State Ionics*, **161**, 243 (2003).

[66] A.B. McEwen, S.F. McDevitt, V.R. Koch, *J. Electrochem. Soc.*, **144**, L84 (1997).

[67] M. Ue, K. Ida, S. Mori, *J. Electrochem. Soc.*, **141**, 2989 (1994).

[68] M. Gratzel, *J. Photochem. Photobiol. C: Photochem. Rev.*, **4**, 145 (2003).

[69] H. Matsumoto, T. Matsuda, *Electrochem.*, **70**, 190 (2002).

[70] N. Papageorgiou, Y. Athanassov, M. Armand, P. Bonhote, H. Pettersson, A. Azam, M. Gratzel, *J. Electrochem. Soc.*, **143**, 3099 (1996).

[71] A.E. Visser, R.P. Swatloski, S.T. Griffin, D.H. Hartman, R.D. Rogers, *Sep. Sci. & Techn.*, **36**, 785 (2001).

[72] G.T. Wei, Z. Yang, C.J. Chen, *Anal. Chim. Acta*, **488**, 183 (2003).

[73] M.L. Dietz, *Sep. Sci. Technol.*, **41**, 2047 (2006).

[74] T.M. Letcher, N. Deenadayalu, B. Soko, D. Ramjugernath, P.K. Naicker, *J. Chem. Eng. Data*, **48**, 904 (2003).

[75] T.M. Letcher, P. Reddy, *Fluid Phase Equilib.*, **219**, 107 (2004).

[76] A. Bosmann, L. Datsevich, A. Jess, A. Lauter, C. Schmitz, P. Wasserscheid, *Chem. Commun.*, 2494 (2001).

[77] S.G. Zhang, Z.C. Zhang, *Green Chem.*, **4**, 376 (2002).

[78] S. Zhang, Q. Zhang, Z.C. Zhang, *Ind. Eng. Chem. Res.*, **43**, 614 (2004).

[79] J. Eber, P. Wasserscheid, A. Jess, *Green Chem.*, **6**, 316 (2004).

[80] W.G. Hoover, *Computational Statistical Mechanics*, (Elsevier, New York, 1991).

[81] D. Frenkel, B. Smit, *Understanding Molecular Simulation*, (Academic Press, San Diego, 1996).

[82] M. P. Allen, D. J. Tildesley, *Computer Simulation of Liquids*, (Oxford, Clarendon, 1987).

[83] M. E. Tuckerman. *Statistical Mechanics: Theory and Molecular Simulation*, (Oxford, Clarendon, 2010).

[84] L. Verlet, *Phys. Rev.*, **159**, 98 (1967).

[85] L. Verlet, *Phys. Rev.*, **165**, 201 (1968).

[86] R.W. Hockney, J.W. Eastwood, *Computer simulation using particles*, (Taylor & Francis, Inc. Bristol, PA, USA 1998).

[87] W.C. Swope, H.C. Andersen, *Phys. Rev. B*, **41**, 7042 (1990).

[88] T.A. Darden, D.York, L. Pedersen, *J. Chem. Phys.*, **98**, 10089 (1993).

[89] R.W. Hockney, J.W. Eastwood, *Computer Simulation Using Particles*, (Taylor & Francis, 1989)

[90] D. K. Remler, P. A. Madden, *Molec. Phys.*, **70**, 912 (1990).

[91] G. Pastore, E. Smargiassi, F. Buda, *Phys. Rev. A*, **44**, 6334 (1991).

[92] M. C. Payne, M. P. Teter, D. C. Allan, T. A. Aris, J. D. Joannopoulos, *Rev. Mod. Phys.*, **64**, 1045 (1992).

[93] M. E. Tuckerman, M. Parrinello, *J. Chem. Phys.*, **101**, 1302, 1316 (1994).

[94] J. Hutter, M. E. Tuckerman, M. Parrinello, *J. Chem. Phys.*, **102**, 859 (1995).

[95] M. E. Tuckerman, P. J. Ungar, T. von Rosenvinge, M. L. Klein, *J. Phys. Chem.*, **100**, 12878 (1996).

[96] M. J. Gillan, *Contemp. Phys.*, **38**, 115 (1997).

[97] M. Parrinello, *Solid State Commun.*, **102**, 107 (1997).

[98] E. Sandre, A. Pasturel, *Mol. Simul.*, **20**, 63 (1997).

[99] D. Marx, *Nachr. Chem. Tech. Lab.*, **47**, 186 (1999).

[100] M. Parrinello, *Comput. Sci. Engg.*, **2**, 22 (2000).

[101] N. W. Ashcroft and N. D. Mermin, *Solid State Physics*, Saunders College Publishing, Philadelphia, 1976.

[102] J. Ihm, A. Zunger and M. L. Cohen, *J. Phys. C.*, **12**, 4409-4422 (1979).

[103] W. E. Pickett *Computer Physics Reports*, **9**, 115-197 (1989).

[104] F. Gygi, *Europhysics Letters*, **19**, 617-622 (1992).

[105] N. A. Modine, G. Zumbach, E. Kaxiras, *Phys. Rev. B*, **55**, 10289-10301 (1997).

[106] D. Marx, Jürg Hutter, *Ab Initio Molecular Dynamics*, Cambridge University Press, 2009.

[107] J. Kohanoff, *Electronic Structure Calculations for Solids and Molecules*, Cambridge University Press, 2006.

[108] V. Heine, *Solid. St. Phys.*, **24**, 1 (1970).

[109] L. R. kahn, W. A. Goddard, *J. Chem. Phys.*, **56**, 2685 (1972).

[110] L. Kleinman, D. M. Bylander, *Phys. Rev. Lett.*, **48**, 1425 (1982).

[111] A. Rappe, K. Rabe, E. Kaxiras, J. D. Joannopoulos, *Phys. Rev. B.*, **41**, 1227 (1990).

[112] D. Vanderbilt, *Phys. Rev. B.*, **41**, 7892 (1990).

[113] N. Trouillier, J. L. Martins, *Phys. Rev. B.*, **43**, 1993 (1991).

[114] N. J. Ramer, A. M. Rappe, *Phys. Rev. B.*, **59**, 12471 (1998).

[115] Goedecker, S.; Teter, M.; Hutter, *J. Phys. Rev. B* 1996, **54,** 1703-1710.

[116] Hartwigsen, C.; Goedecker, S.; Hutter, *J. Phys. Rev. B* 1998, **58,** 3641-3662.

[117] P. Hohenberg, W. Kohn, *Phys. Rev.*, **136**, B864 (1964).

[118] W. Kohn, L. J. Sham, *Phys. Rev.*, **140**, A1133 (1965).

[119] I. R. Stich, R. Car, M. Parrinello, S. Baroni, *Phys. Rev. B.*, **39**, 4997 (1989).

[120] Broyden, C. G., *Journal of the Institute of Mathematics and Its Applications*, **6**, 76-90 (1970).

[121] Fletcher, R., *Computer Journal*, **13 (3)**, 317-322 (1970).

[122] Fletcher, R., *Practical methods of optimization*, (2nd ed.), New York: **John Wiley & Sons, ISBN 978-0-471-91547-8**, (1987).

[123] Goldfarb, D., *Mathematics of Computation*, **24 (109)**, 23-26 (1970).

[124] Shanno, David F., *Math. Comput.*, **24 (111)**, 647-656 (1970).

[125] Shanno, David F.; Kettler, Paul C., *Math. Comput.*, **24 (111)**, 657-664 (1970).

[126] S.J. Plimpton, *J. Comp. Phys.*, **117**, 1 (1995).

[127] Cp2k, http://www.cp2k.org.

[128] Hutter, J.; Ballone, J. P.; Bernasconi, M.; Focher, P.; Fois, E.; Goedecker, S.; Marx, D.; Parrinello, M.; Tuckerman, M. E. CPMD, version 3.13.2; Max Planck Institut fuer Festkoerperforschung and IBM Zurich Research Laboratory: Stuttgart, Germany, and Zurich, 1990.

[129] Frisch, M. J.; et al. Gaussian 09, Revision B. 01; Gaussian Inc.; Wallingford, CT, 2010.

[130] W. Humphrey, A. Dalke, K. Schulten, *J. Molec. Graphics*, **14**, 33 (1996).

[131] Jmol: an open-source Java viewer for chemical structures in 3D. http://www.jmol.org/

[132] McMahon, B.; Hanson, R. M. *J. Appl. Crystallogr.* 2008, **41**, 811.

[133] Mercury: visualization and analysis of crystal structures C. F. Macrae, P. R. Edgington, P. McCabe, E. Pidcock, G. P. Shields, R. Taylor, M. Towler and J. van de Streek, *J. Appl. Cryst.,* **39,** 453-457, 2006.

[134] http://upload.wikimedia.org/wikipedia/commons/f/fe/Tributyl-phosphate-2D-skeletal.png

[135] http://upload.wikimedia.org/wikipedia/commons/f/fb/Sketch_Pseudopotentials.png

Chapter 2

Structure and dynamics of tri-*n*-butyl phosphate/*n*-octane mixtures : Molecular Dynamics simulation study

2.1 Introduction

In the field of solvent extraction, liquid-liquid extraction is the most common technique to separate compounds. In this method, compounds are separated based on their relative solubilities in two different immiscible liquids; most often the two liquids happen to be water and an organic solvent. This technique is used to extract a substance from one liquid phase to another. The most common examples where liquid-liquid extraction is used are nuclear reprocessing, ore processing, in the production of fine organic compounds and in other industries. The theme of the development of nuclear reprocessing technology was based on the chemical separation and recovery of metal ions like plutonium, uranium, zirconium etc. from irradiated nuclear fuel.[1] In the solvent extraction methods for nuclear fuel recycling, often the organic phase consists of a mixture of an extracting agent and a diluent. An important family of extractant molecules are the neutral organophosphorus ligands. They bind the hard cations via their phosphoryl group. In the context of cation separation by liquid-liquid extraction technique, the most important species is tri-*n*-butyl phosphate (TBP).[2,3] It has been used to extract uranium,[4–7] plutonium,[8,9] zirconium[10] and other metal ions.[11] In organic solvents such as chloroform,[12] liquid TBP is completely miscible, but its solubility in water (χ_{TBP} is rather low, a value of 2.6 $\times$ 10^{-5} at 298 K[13]). In acidic phases too, it is almost insoluble. After the discovery by Warf,[14] TBP has become the cornerstone of the industrial PUREX (Plutonium Uranium Refining by Extraction) extraction process to separate uranyl and plutonyl cations from nuclear waste solutions.[15,16] In such a liquid-liquid extraction process, the organic components gets separated into two phases, a light phase and a heavy organic phase. The heavy organic phase consists of high concentration of U(VI), Pu(VI) and TBP. This heavy organic phase is known as the third phase.[38] Thus, in prospect of this renewed interest in nuclear energy and waste management, a better understanding of molecular processes involved in heavy metal extraction is needed.

At room temperature, TBP is a liquid (boiling point = 284 ± 5°C, freezing point ≈ -80°C, and density at 25°C = 0.9727 g cm^{-3}).[26] All neutral organophosphorus compounds exhibit a tendency to self-associate and TBP is not contrary to this general trend.[27–31] Its self-association has been brought out with a variety of techniques including distribution experiments,[33] infrared spectroscopy,[34] nuclear magnetic resonance,[27] calorimetry,[29,30] and vapor pressure osmometry.[35] These techniques have also been used to explain the interaction between phosphate ester and the diluent.[36] It was established that the ester exhibits positive non-ideality in hexane but negative nonideality in CCl_4, $CHCl_3$ and benzene. In hexane, the positive nonideality accounts for the self-association of TBP. On the contrary, in other diluents the negative nonideality refers to TBP-diluent interaction, i.e., interaction between the phosphoryl oxygen and the π-electrons of benzene, hydrogen bonding between phosphoryl oxygen and chloroform and the interaction of the vacant 3d-orbital of chlorine and the phosphoryl oxygen.[36] With the help of proton magnetic resonance studies,[37] the existence of hydrogen bonding between TBP and chloroform has also been ascertained.

All these studies revealed that the dipole-dipole interactions between the P=O groups of the phosphate ester is responsible for the self-association of TBP, leading to the formation of TBP dimers and higher oligomers.[26,27,32–34] Alcock et al. [39] have studied the TBP-water system to explain the hydrogen bonding between phosphoryl oxygen and water proton, which leads to the formation of monohydrate compound such as TBP. H_2O which exists in organic phase. In a review,[40] Osseo-Asare examined the TBP-diluent/H_2O-acid-metal ion extraction systems. On the basis of his observations, Osseo-Asare proposed the existence of highly ordered assembly (such as a micelle or microemulsion) of TBP-acid-metal ion complex in organic diluents. The self-assembled framework consists of a hydrophilic core and a hydrophobic shell. The former is polar in nature and is composed of P=O groups of TBP and hence is capable of incorporating heavy metal ions. On the other hand, the hydrophobic shell is composed of the larger butyl tails of TBP and that is swollen by the diluent. In later years, progress was made to understand the formation, mechanism and structure (size, shape and aggregation number) of high-order assemblies in the organic phase by small-angle X-ray and neutron scattering (SAXS and SANS) techniques. Erlinger et al.[41] investigated the microscopic structures of reverse micelles of malonamides in organic phases by using the Baxter sticky hard sphere model.[42–44] They suggested that the van der Waals interactions between the malonamide reverse micelles in organic phase is the origin of third phase formation. Since then, Chiarizia, Jensen and co-workers[45] have studied the small-angle scattering profiles for organic phases containing TBP and heavy metal ions using the same hard sphere model. Very recently, Motokawa et al.[46] have studied the TBP/octane systems in dry conditions (without water) to reveal the microscopic structure of TBP assemblies in a dry diluent through analysis of the SAXS and SANS profiles. They proposed the fact that the attractive interactions among TBP assemblies in octane is very less and the shape of the TBP assembly is ellipsoidal.

In recent years, molecular modeling studies have been used to understand the fundamental molecular level behavior for some extraction systems. Molecular dynamics studies have been carried out by Wipff and co-workers to study systems such as TBP in vacuum and in chloroform,[17] the stoichiometry of TBP complexation in aqueous solution,[18] TBP complexation with uranyl nitrate and dissolution in supercritical CO_2,[19] the effect of TBP concentration and water acidity at the water-oil interface,[20] and liquid-liquid extraction of pertechnetic acid by TBP.[21] Almeida and co-workers have performed a series of molecular dynamics simulations to illustrate the aqueous phase complex formation process, interfacial migration and the effect of interface in promoting the formation of various complex species and the migration of neutral species into the organic phase.[22–25]

To our knowledge, no simulations have been carried out on a system such as TBP in a dry diluent. In this work, we present a classical molecular dynamics simulation study of TBP in a dry diluent, (*n*-octane) to provide an important glimpse into the initial state of the organic phase prior to the extraction of heavy metal ions.

2.2 Computational Details

Classical molecular dynamics simulations were performed on three different systems: (1) pure TBP (2) pure *n*-octane and (3) TBP/*n*-octane mixtures. Densities of pure systems calculated from these simulations agree well with experiments.[51,52] We took a number of TBP/*n*-octane mixtures as a function of volume fraction of TBP. Initial simulations were carried out on small system sizes (containing a maximum of 400 TBP molecules and 1500 octane molecules) to try and understand the solution and to identify the length scale of emerging intermolecular correlations. Larger system sizes were required as TBP molecules were seen to aggregate in n-octane. Volume fractions studied with the number of molecules employed are shown in Table 2.1.

Table 2.1: Summary of different systems studied.

Volume fraction of TBP (%)	Small system		Large system	
	TBP	*n*-octane	TBP	*n*-octane
100	256	—	2000	—
90	—	—	1800	334
80	400	167	—	—
75	300	167	1500	835
60	300	334	—	—
50	200	334	1000	1670
40	200	501	—	—
25	200	1002	500	2505
10	100	1503	200	3006
0	—	500	—	—

An all atom model based on the OPLS (Optimized Potentials for Liquid Simulations) force field developed by Almeida et al.[47] was used for TBP whereas for *n*-octane, the TraPPE united atom model[81] was used. Initial configurations of different mixture systems as well as of the pure systems were generated using the Packmol software package.[49] Equations of motion were integrated with the velocity Verlet algorithm with a time step of 0.5 fs. A cutoff of 15 Å was chosen for calculating pairwise interactions in real space for those atoms whose distance falls below this value. Above this value, long-range electrostatic interactions were computed using particle-particle particle-mesh solver with a precision of 10^{-5}. Non-bonded interaction potentials calculated for pair of atoms which were separated by three bonds were applied with scaling factors 1/2 and 1/1.2 for van der Waals and electrostatics, respectively. The parameters for cross interactions between different molecular species (atomic groups) were derived using the standard Lorentz-Berthelot rules.[81]

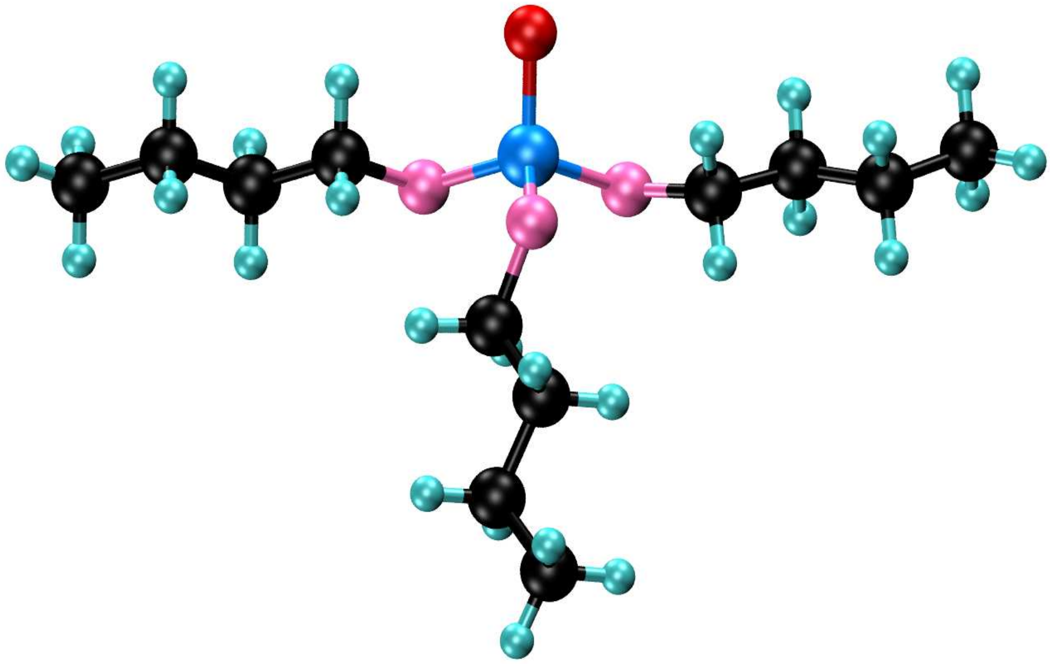

Figure 2.1: Schematic of tri-*n*-butyl phosphate. Colors: Phosphorus-blue, Oxygen (O2)-red, Oxygen (OS)-pink, Carbon-black, Hydrogen-cyan.

Three dimensional cubic periodic boundary conditions were applied.

Classical molecular dynamics simulations at constant number of molecules and constant temperature at 298 K were performed. Temperature and pressure of the systems were maintained at 298K and 1 atm using Nose-Hoover thermostat and barostat respectively, with a damping factor of 1 ps. Initial configurations were relaxed using standard energy minimization methods. Constant pressure and constant temperature ensemble (NPT) simulations were carried out on these energy minimized configurations until the volume equilibrated. We thus obtained the average box length of a particular system from which densities were calculated. The final coordinates of NPT run were taken to constant-volume and constant-temperature (NVT) ensemble simulation for further equilibration over 2 ns. Finally, an analysis run was generated for 5 ns in which configurations were stored every 500 ps. Simulations were carried out using the LAMMPS[80] software package. All systems were visualized using VMD.[53]

Partial pair correlation functions were obtained between all distinct pairs of atom types, up to a distance of half the box length and a bin width of 0.02 Å was used. These partial pair correlation functions were then used to obtain the isotropic partial structure factors.

The isotropically averaged partial structure factor between a pair of atom type α and β is given by,

$$S_{\alpha\beta}(q) = \delta_{\alpha\beta} + 4\pi\sqrt{\rho_\alpha\rho_\beta}\int_0^\infty r^2[g_{\alpha\beta} - 1]\frac{sin(qr)}{(qr)}dr \tag{2.1}$$

where $\rho_\alpha = \frac{N_\alpha}{V}$. N_α is the number of atoms of type α and V is the volume of the system, δ is the Kronecker delta function and g(r) is the partial pair correlation function. The upper limit in the integral was replaced with half the box length. The total X-ray structure factor is defined as

$$S(q) = \sum_\alpha\sum_\beta c_\alpha c_\beta \frac{f_\alpha(q)f_\beta(q)}{\langle f(q)\rangle^2} S_{\alpha\beta}(q) \tag{2.2}$$

where c_α is the concentration of atom type α in the system. f_α is the form factor of the atom type α and $\langle f(q)\rangle = \sum_\alpha c_\alpha f_\alpha(q)$.

The minimum value of q in our calculation was set by the linear dimension of the simulation box. The box length for all of our large systems were in the neighborhood of 96 Å. Therefore the lowest value of q was around 0.065 $Å^{-1}$. The X-ray form factors for all the atom types were obtained from NIST X-Ray Form Factors, Attenuation and Scattering Tables.[54] The values of form factors for each atom type are needed at integral multiples of the smallest q, which depends on the length of the simulation box. The values of form factors obtained from NIST were linearly interpolated to obtain form factors at the desired q values.

The total neutron structure factor was also obtained from the partial pair correlation functions. The coherent neutron scattering cross section is defined as

$$\left(\frac{\partial^2\sigma}{\partial\Omega\partial\omega}\right)_{coh} = \frac{1}{N}\frac{k}{k_0}\sum_{\alpha=1}^{n}\sum_{\beta=1}^{n} b_\alpha^{coh} b_\beta^{coh} \sqrt{N_\alpha N_\beta} S^{\alpha\beta}(Q,\omega) \tag{2.3}$$

Here b_α^{coh} and b_β^{coh} are the coherent scattering lengths relative to isotopes α and β. The coherent neutron scattering function (or the scattering length density) relative to the atom types α and β is given by,

$$S^{\alpha\beta}(Q,\omega) = \frac{1}{2\pi\sqrt{N_\alpha N_\beta}} \int_{-\infty}^{+\infty} \sum_{i_\alpha=1}^{N_\alpha}\sum_{j_\beta=1}^{N_\beta} \langle exp\{iQ.R_{i_\alpha}(t)\} \times exp\{-iQ.R_{j_\beta}(0)\}\rangle exp(-i\omega t)dt \tag{2.4}$$

where N_α and N_β are the number of atoms of type α and β respectively. Here the q-independent neutron scattering length of all the different atom types replaces the form factors in the case of X-ray structure factor. Neutron scattering length of all the different atom types were obtained from NIST Neutron scattering lengths and cross sections table.[54] Two factors play an important role here. Hydrogen possesses a large incoherent scattering cross section. Thus, the presence of hydrogen atoms generates an incoherent background which acts as a noise to the original scattering profile. In the present case, scattering from hydrogen atoms comes both from the butyl tails of TBP molecules as well as from octane molecules. Hence, to ensure sufficient contrast in neutron scattering between TBP and n-octane, the hydrogen atoms in n-octane should be replaced by deuterium. Because of these two reasons, we have considered deuterated octane molecules in our calculations for the scattering profiles, while maintaining hydrogens in case of alkyl tails in TBP.

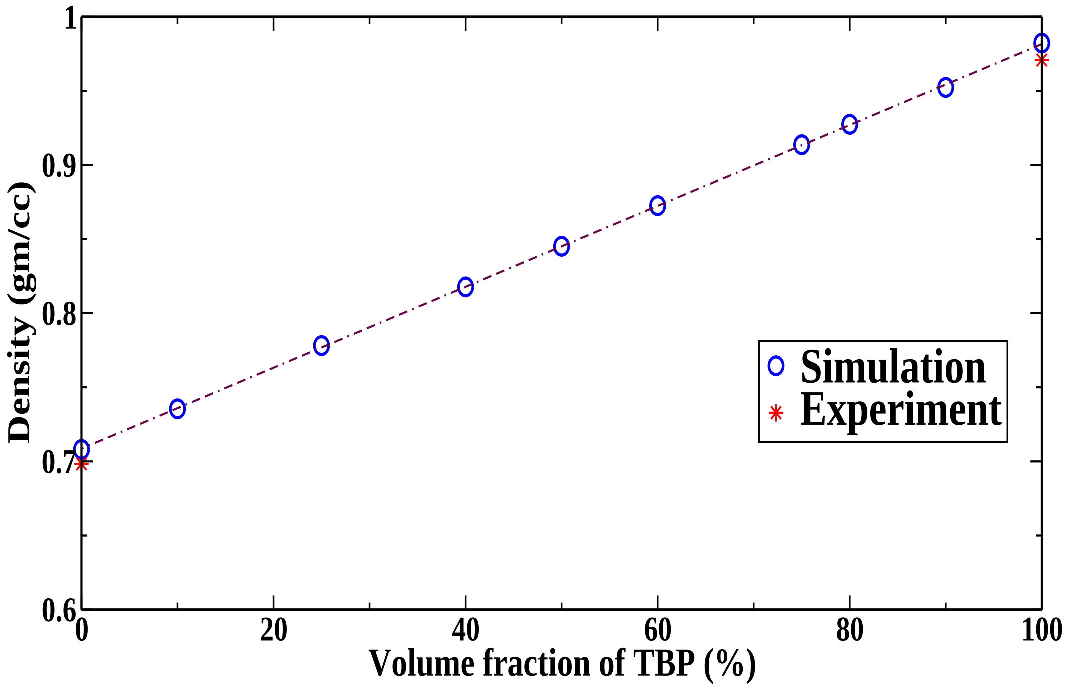

Figure 2.2: Density variation with volume fractions of TBP in the TBP/*n*-octane mixtures at 298 K.

2.3 Results and Discussion

2.3.1 Mass density

All simulations described were carried out at 298 K. The mass density of the systems were obtained from the converged volume during the constant NPT run. The density of pure TBP converged to 0.9750 gm/cc as against the experimental value[51] of 0.9708 gm/cc, whereas for *n*-octane it was 0.7043 gm/cc as against the experimental value[52] of 0.7032 gm/cc. Densities of the mixture systems were also calculated and plotted as a function of the concentration of TBP in Figure 2.2. Values are provided in Table 2.2.

Table 2.2: Calculated density values of TBP/n-octane mixture systems at 298 K.

System (% TBP)	Density (gm/cc)
100	0.982
90	0.952
80	0.927
75	0.914
60	0.872
50	0.845
40	0.818
25	0.778
10	0.735
0	0.708

2.3.2 Radial distribution function

The radial distribution functions between atoms belonging to different molecules were calculated. These are useful tools to obtain a deep insight into the microscopic structure of TBP/n-octane mixtures. Most of the radial distribution functions calculated involves the atoms on the phosphoryl group and between phosphorus and other atoms in the polar part of the TBP molecule. The polar core of TBP consists of phosphorus, a doubly bonded oxygen (O2 type) and three singly bonded oxygens (OS type) with the butyl tails. The butyl tail forms the non-polar part of the molecule while the P=O vector defines the polar region. Thus the pair correlation functions between phosphorus-phosphorus, phosphorus and the two different oxygen types can aid us with an understanding of the organization of these molecules. Another pair correlation function between phosphorus and the last carbon (of type C_d) of butyl tail was also calculated in order to see how the butyl tails are distributed around the phosphorus atom. Let us look at the radial distribution functions between these pairs.

The P-P radial distribution function is shown in Figure 2.3. It shows a broad peak starting around 6 Å running to about 11 Å. A close examination reveals the

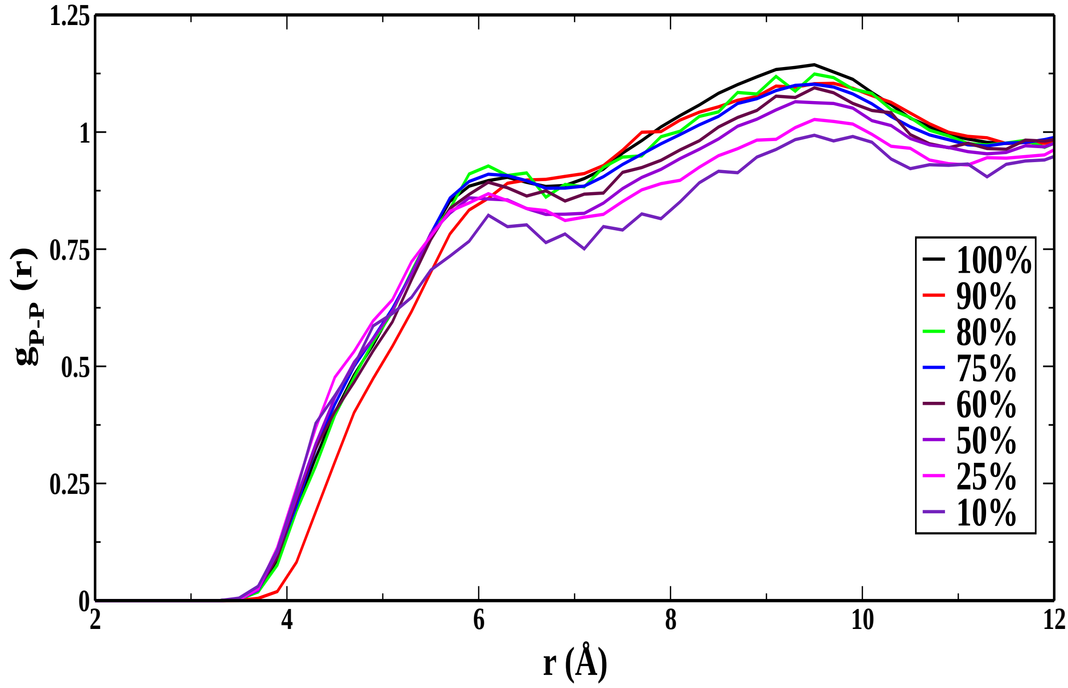

Figure 2.3: Intermolecular pair correlation function between the pairs of atoms P-P on two TBP molecules. Features beyond 12Å are not shown for clarity.

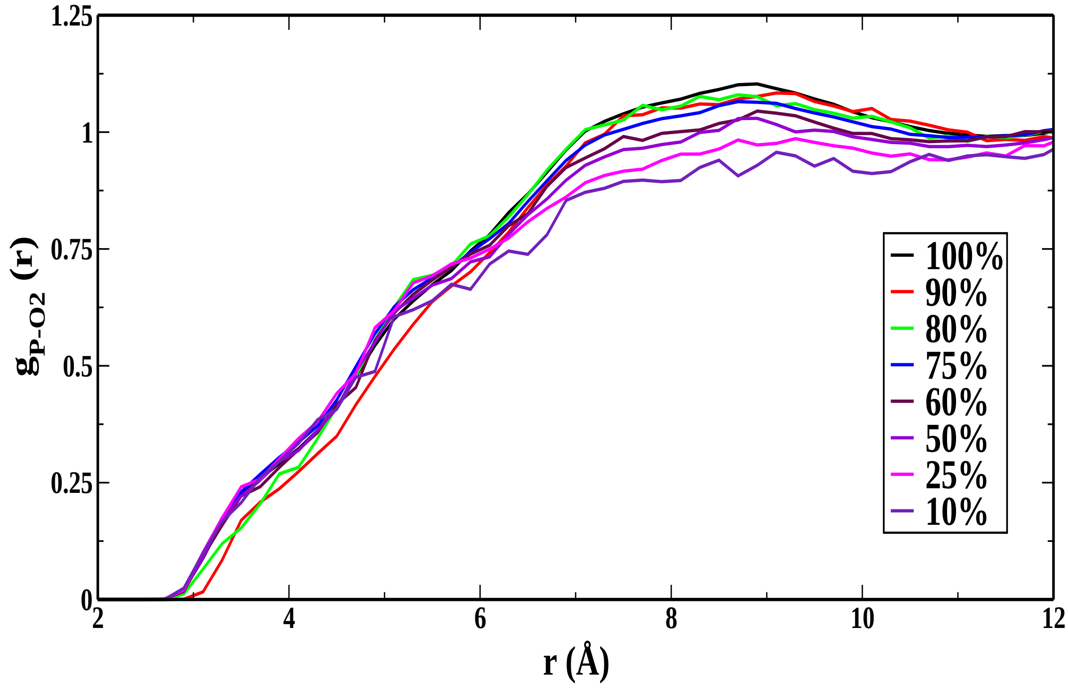

Figure 2.4: Intermolecular pair correlation function between the pairs of atoms P-O2 on two TBP molecules.

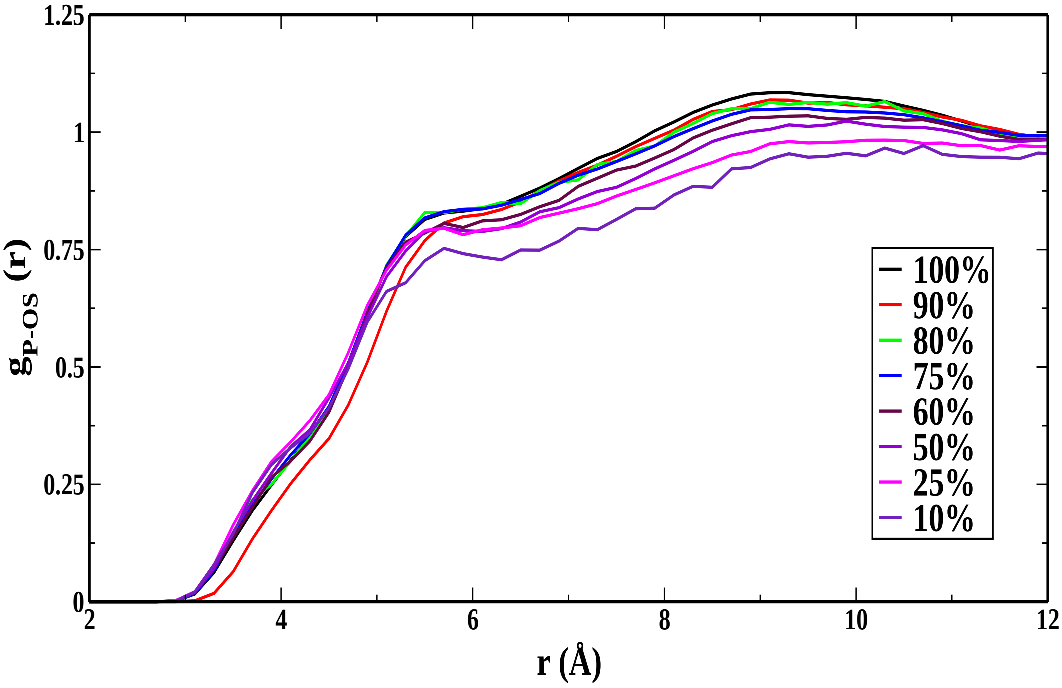

Figure 2.5: Intermolecular pair correlation function between the pairs of atoms P-OS on two TBP molecules.

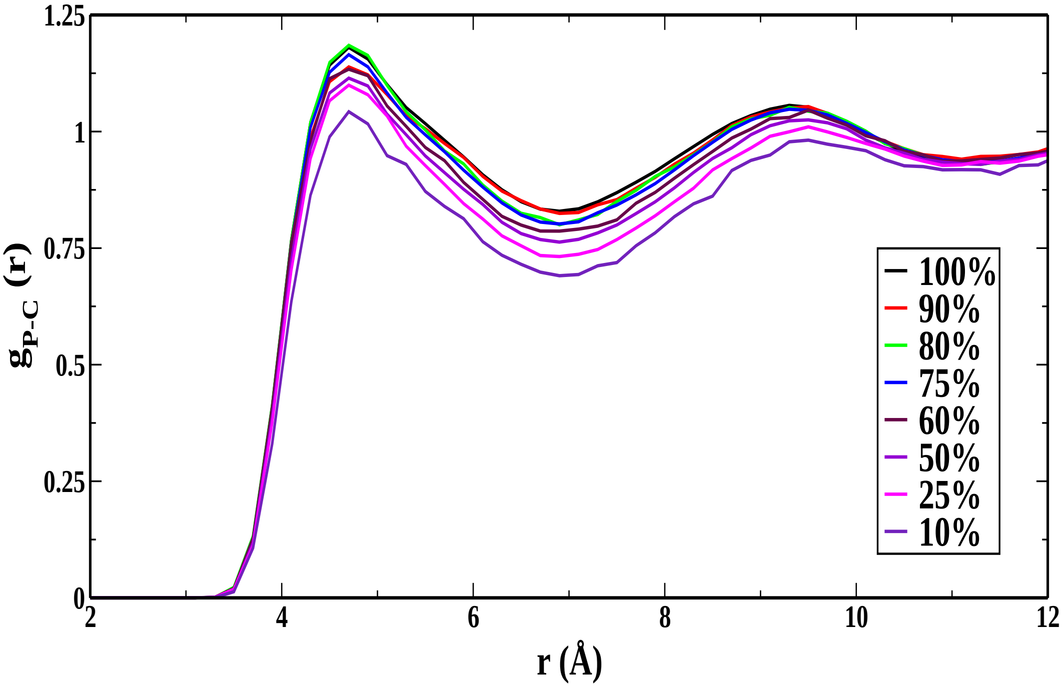

Figure 2.6: Intermolecular pair correlation function between the pairs of atoms P-C_d on two TBP molecules.

Table 2.3: Coordination numbers in the first neighbor shell. These distances correspond to the minimum of the first peak in the corresponding pair correlation function.

System (% TBP)	Coordination number
100	2.19
90	1.72
75	1.68
50	1.10
25	0.55
10	0.21

existence of a shoulder at 4.5 Å whose intensity increases with TBP concentration. It thus appears that near neighbour phosphorus atoms are distributed around a phosphorus atom in two different orientations. Because of the presence of large butyl tails, it is very difficult for two phosphorus atoms on two different TBP molecules to approach each other from the hydrophobic side. Instead, they approach each other from the P=O direction; it is likely that intermolecular dipole-dipole interactions between two P=O group aids in this process. We shall discuss the orientational preferences further in the next section. The integral of the P-P g(r) up to the first coordination shell provides the coordination number which are listed in Table 2.3.

A maximum of two TBP molecules can be present within the first neighbor shell; however, its propensity decreases rapidly with decreasing TBP concentration in octane. Thus if TBP self-associates in dry octane, it can only form up to dimer, not more than a dimer. Experimental findings also supports our simulated results.[46]

The P-O2 radial distribution function is shown in Figure 2.4. Three main features can be observed within the first coordination shell. The closest distance between phosphorus and oxygen (O2) is determined by the first shoulder in the phosphorus-phosphorus rdf which was present at 4.5 Å. Given that the P=O bond length is 1.48 Å, we can expect a similar shoulder in the P-O2 g(r) at around 3 Å. Indeed, such a feature is present at 3.1 Å in Figure 2.4. Following the same line of thought, we can see the subsequent shoulder in the P-O2 RDF at around 4.5 Å which is likely to be related to the peak present in the P-P RDF at 6 Å. These observations hint at the likely orientation of the P=O bond vectors which we take up in detail later.

Figure 2.5 shows how the oxygen atoms (OS) are distributed around the phosphorus atom in two different TBP molecules. There exist three OS type oxygen atoms in a single TBP molecule which are attached to the large butyl tails. These butyl tails are free to rotate and they can fold as well. As mentioned earlier, the butyl tails inhibit the phosphorus atoms to approach directly along their direction. However, as we saw earlier, the P=O vector can have two different orientations, perpendicular and anti-parallel. When the P=O vectors lie perpendicular to each other, the distance between phosphorus and oxygen atom (OS) can exhibit two different distributions. Due to this, phosphorus-oxygen (OS) pairs have their closest distance at around 4 Å and another clear shoulder around 5.5 Å. But, in the perpendicular orientations of P=O vectors, the double bonded oxygen atoms (O2) came close to each other, while, the single bonded oxygens (OS) atoms containing the butyl tails remains separated by a large distance. Hence, the distance between phosphorus and oxygens (OS) atoms became largest in this orientation. So, when P=O vectors remains anti-parallel to each other we obtain a broad peak at around 9 Å distance in the P-OS radial distribution function.

The intermolecular P-C_d radial distribution function is shown in Figure 2.6. Compared to other radial distribution functions it is having very sharp peak for each coordination shell. The first peak appears at 4.7 Å and first neighbor shell ends up at around 7 Å. After that, other coordination shells are also defined by clear and sharp peaks. After integrating the radial distribution function at the distance where the first neighbor shell ends, we obtain the coordination number of tail carbon atoms around a phosphorus atom. The maximum value of this coordination number is for the pure TBP system, where two tail carbons were found to be distributed around a phosphorus atom. For other systems its value decreases with decrease in the volume fraction of TBP. From these observations, it is evident that only two TBP molecules are self-associating and not more than a dimer forms either in pure liquid TBP or in TBP-octane solutions.

2.3.3 Small angle scattering

We have calculated the total X-ray and neutron scattering intensities for all the systems studied here. The intensities were taken to be the square of total structure factors for both the X-ray and neutron scattering and no other correction factors were not included in our calculation. Due to this, we did not provide much importance to the intensities for different systems, instead our main focus was the peak positions and the microscopic origin of the peaks.

At low wave vectors, the simulation data is limited by the system size. However, structural details up to a distance of around 25 nm^{-1} are well reproduced by our simulations. With a box length of around 96 Å the wave vector resolution is limited in our simulations to around 0.6 nm^{-1}. A finer resolution would necessitate a much larger box length which is beyond the scope of the present work.

Figure 2.7 compares the total X-ray intensity calculated from our simulations with experimentally obtained X-ray intensities at various compositions, while Figure 2.8 exhibits the same for neutron scattering. At TBP concentrations of 10 and 20%, no peak can be found at $q = 6.5$ nm^{-1}, consistent with the experimental data. However, a feature appears at this wave vector for concentrations beyond 50% volume fraction of TBP in the mixture systems whose intensity increases with TBP fraction. At this point, we can observe another interesting feature in the position of the main peak at 6.6 nm^{-1}. With increasing TBP concentration, this peak shifts slightly to larger wave vector values. What is the origin of this peak? Let us attempt this question through an examination of the weighted partial structure factors for

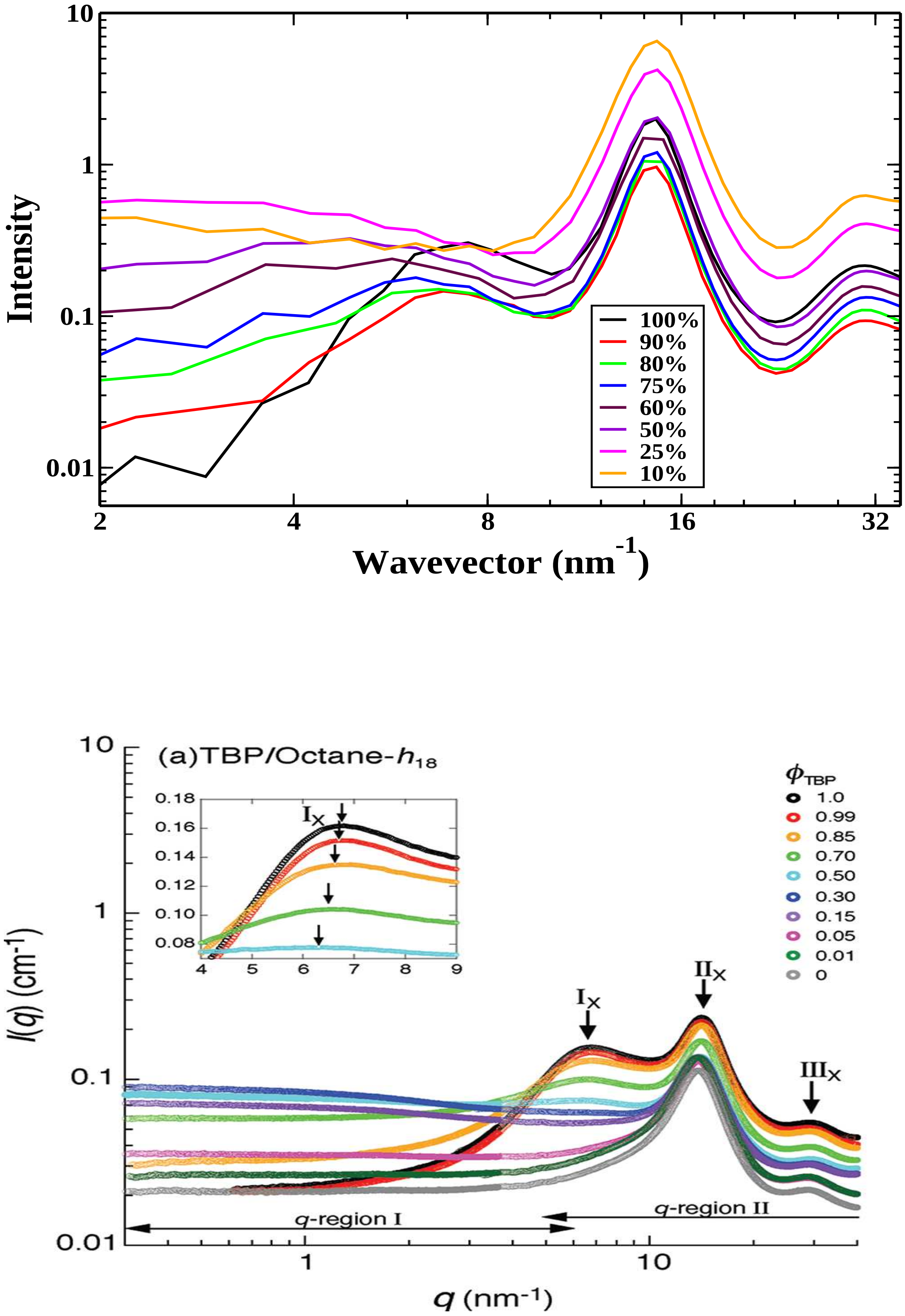

Figure 2.7: Comparison between the total X-ray intensity calculated from simulation (above) and experiment (below) for TBP/n-octane systems.[46]

Copyright: Experimental scattering profile has been reproduced with permission from *J. Phys. Chem. B*, **116,** 1319 (2012) Copyright 2012 Americal Chemical Society.

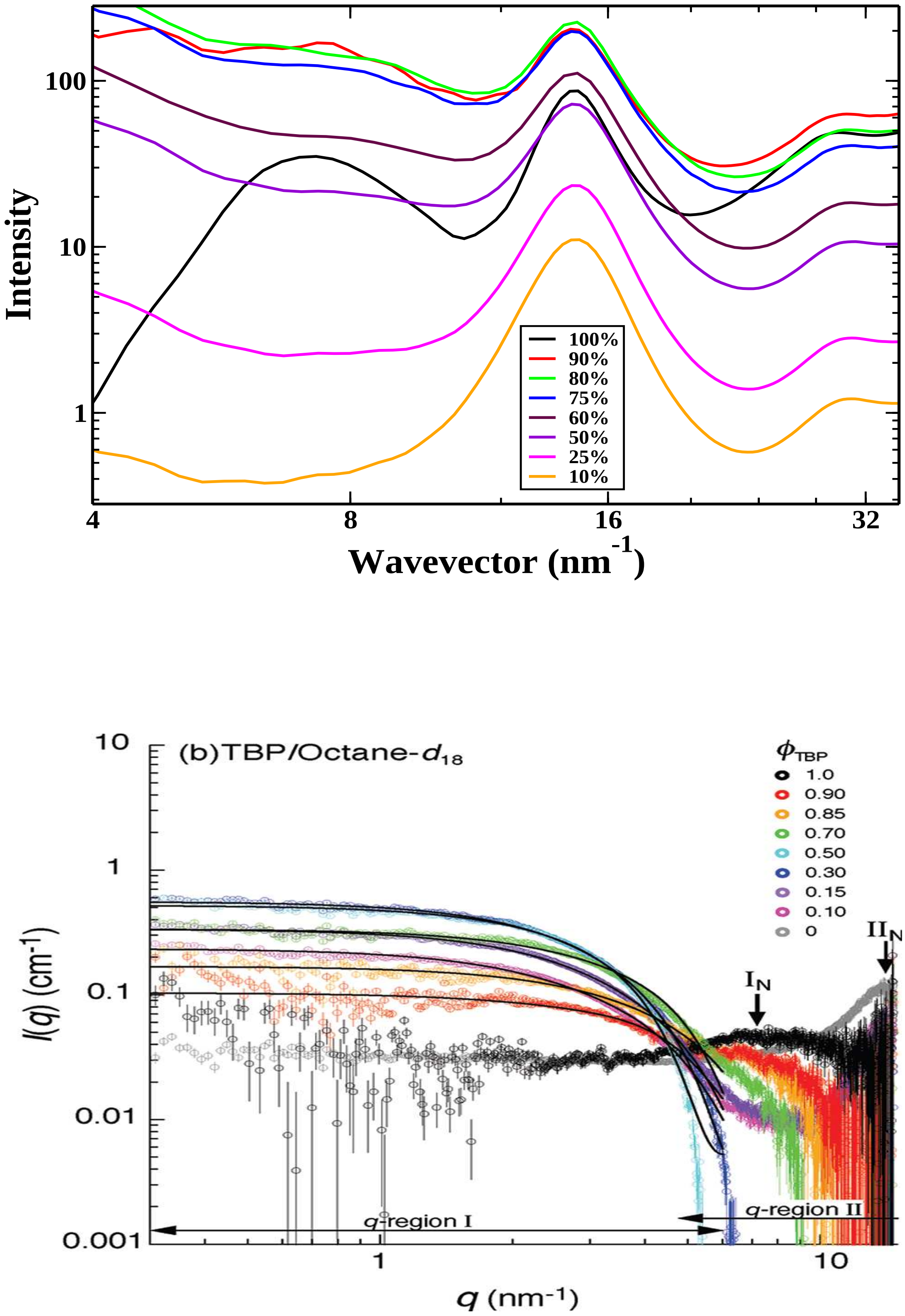

Figure 2.8: Comparison between the total neutron intensity calculated from simulation (above) and experiment (below) for TBP/octane-d_{18} systems.[46]

Copyright: Experimental scattering profile has been reproduced with permission from *J. Phys. Chem. B*, **116,** 1319 (2012) Copyright 2012 Americal Chemical Society.

both X-ray and neutron scattering.

Figure 2.9 shows the X-ray and neutron weighted partial structure factors for TBP/octane systems at the small q range. We can clearly see that most of the interactions which were responsible for the small q (6.5 nm^{-1}) peak arise from interactions between different pairs of atoms which constitute the polar core of TBP. They appear to originate from the intermolecular dipole-dipole interactions involving P=O groups of the phosphate esters of two different TBP molecules. Interactions including other three oxygens also contribute to this peak. The low wave vector peak demonstrates the inhomogenous distribution of TBP molecules in *n*-octane. A weak assembly can also be said to be formed between TBP molecules primarily through dipole-dipole interactions between P=O groups. This result is consistent with the previous literature which suggest formation of TBP dimer in dry octane.

Two more peaks are present, at 14.5 nm^{-1} and at 29.5 nm^{-1} in case of both X-ray and neutron scattering. Both these peaks are present at all TBP fractions. These arise from intramolecular geometry of TBP and octane and hence are unimportant in the current study.

2.3.4 Orientation of TBP molecules

As discussed earlier, a small shoulder at around 4.5 Å along with a broad peak starting from 6.5 Å and running up to 11 Å was observed in the P-P g(r). This observation suggests two different ways by which two TBP molecules approach each other. Based on this idea, we have calculated the angle distribution between P=O vectors of two neighboring TBP molecules which is shown in Figure 2.10.

The P=O vectors of two neighboring TBP molecules are seen to be distributed in two different orientations. A large number of neighbors are oriented with their P=O vector perpendicular to each other, while a significant but smaller quantum are oriented with this angle being around 145°. Figure 2.11 shows snapshots of TBP

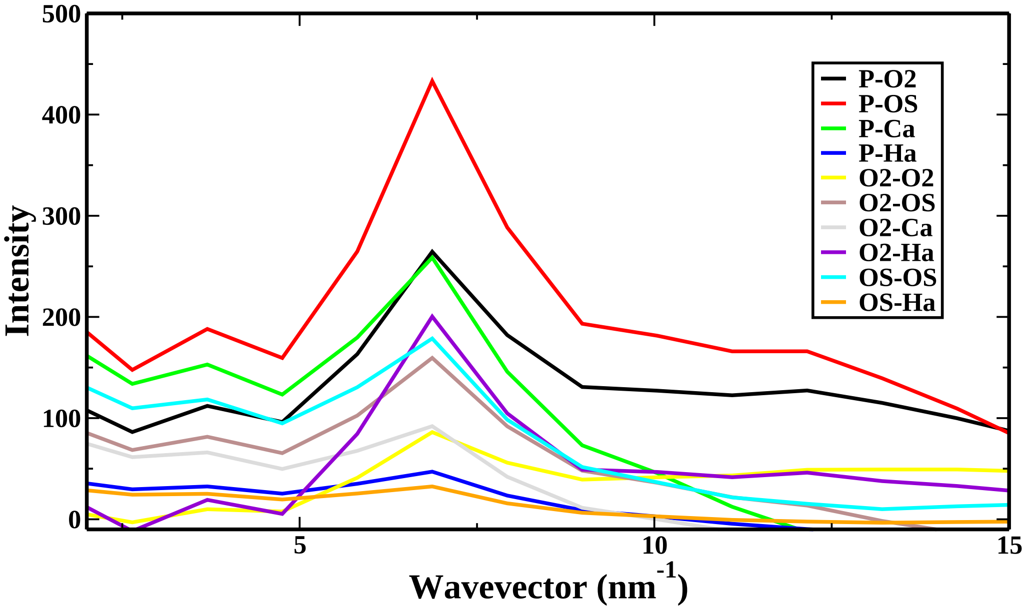

(a) X-ray

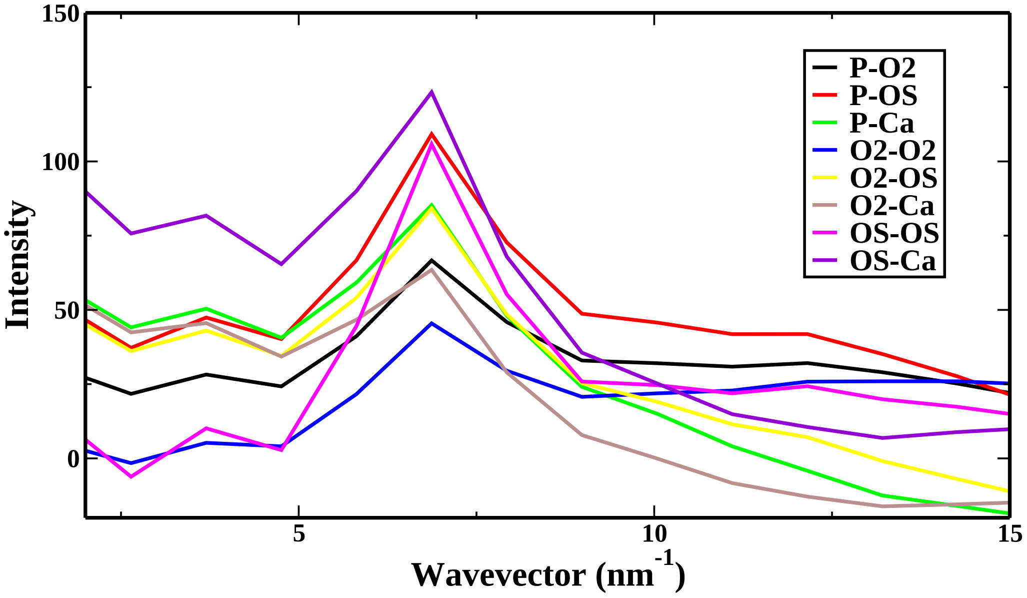

(b) Neutron

Figure 2.9: X-ray (a) and neutron (b) weighted partial structure factors calculated from simulation for TBP/octane systems.

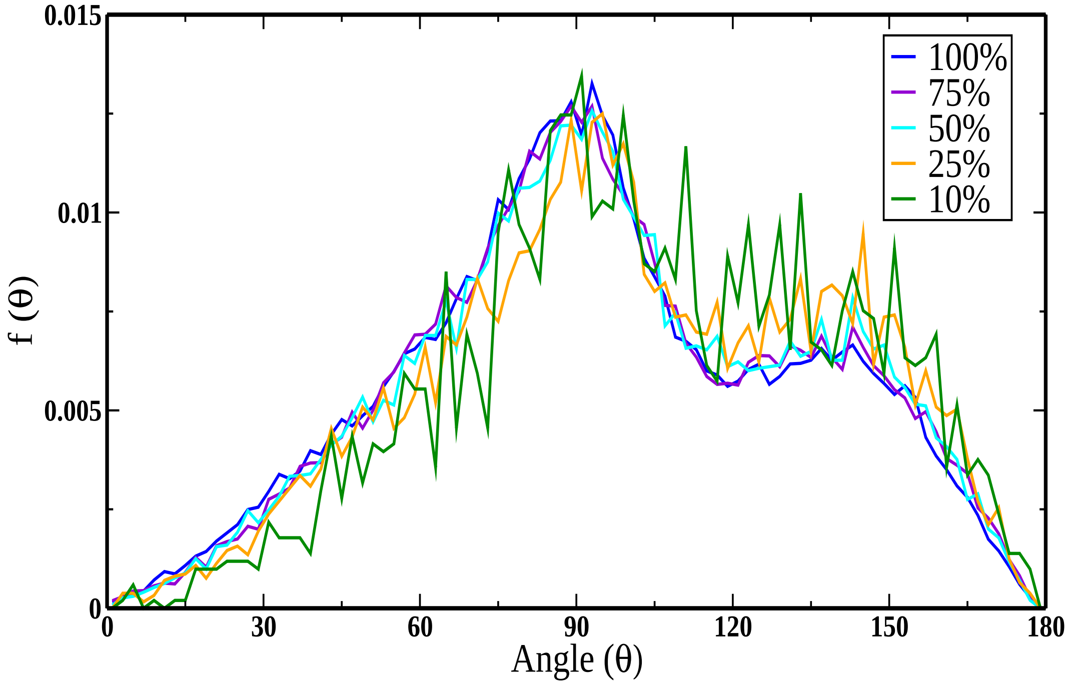

Figure 2.10: Angle distribution between two P=O vectors of two different TBP molecules separated by distance of 4.5 Å or less than that.

molecules taken from the simulations at these two orientations.

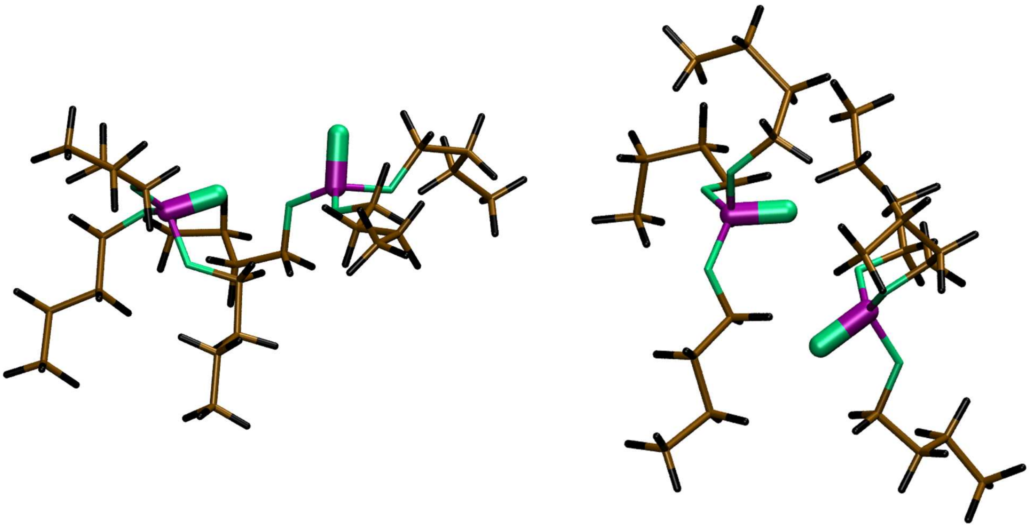

Figure 2.11: Two most probable orientations of P=O vectors in two different TBP molecules.

We have also calculated the distance between two TBP molecules in TBP assemblies. The distance between two phosphorus atoms was calculated for all the

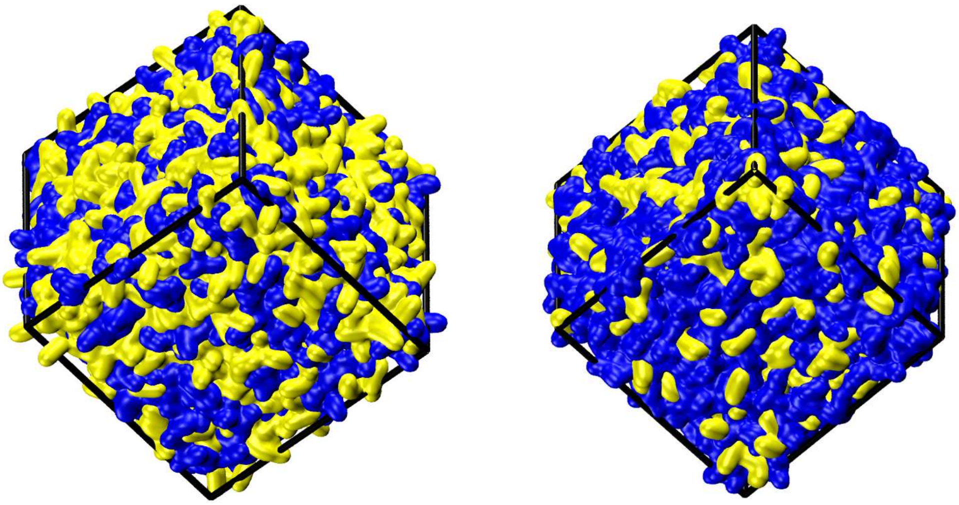

Figure 2.12: Volumetric density map of 50% and 75% TBP/*n*-octane mixture systems. Colors: TBP-blue, *n*-octane-yellow.

configurations and then an ensemble average has been taken over all the configurations. The average distance between two TBP molecules in TBP assemblies was found to be 9 Å.

2.4 Conclusions

We have performed classical molecular dynamics simulations to understand the microscopic structure of TBP/*n*-octane mixtures. Wide and small angle X-ray and neutron scattering functions were calculated and compared to available experimental data. The computed results match experiments closely and offer microscopic insights into the organization of TBP molecules in octane. In particular, we observe the formation of weak TBP assemblies, each containing two TBP molecules oriented such that their P=O bond vectors are oriented nearly perpendicular to each other. Two volumetric density maps containing 50% and 75% TBP in octane are shown in Figure 2.12 to illustrate their distribution in the solution.

The small angle X-ray and neutron profiles exhibit a peak at 6.5 nm^{-1}, whose intensity grows with increasing TBP fraction. This peak originates from the polar core of TBP molecules, the dipole-dipole interactions between intermolecular P=O groups of two different TBP molecules contributing the most. Further, correlations between the other three oxygens attached to the butyl tails too contribute to this feature.

These results indicate that the attractive interactions between TBP molecules in dry octane is contrary to the results obtained for TBP reverse micelles including water, nitric acid or heavy metal ions in their cores. In the absence of water, TBP molecules do not form aggregates larger than a dimer. These structural features of TBP/*n*-octane mixtures should be useful for future investigation of structure of TBP reverse micelles incorporating heavy metal ions.

Bibliography

[1] Andrews, A. *Nuclear Fuel Reprocessing: U.S. Policy.* CRS Report For Congress. Retrieved 25 March 2011.

[2] Marcus, Y.; Kertes, A. S. *Ion Exchange and SolVent Extraction of Metal Complexes;* Wiley-Interscience: New York, 1969.

[3] Tedder, D. W. *In Science and Technology of Tributyl Phosphate;*Schultz, W. W., Navratil, Z. D., Kertes, A. S., Eds. ; CRC Press, Boca Raton, FL, 1991; pp 35-70.

[4] Chiarizia, R.; Jensen, M. P.; Borkowski, M.; Ferraro, J. R.; Thiyagarajan, P.; Littrell, K. C. *Solvent Extr. Ion Exch.* 2003, **21,** 1-27.

[5] Chiarizia, R.; Nash, K. L.; Jensen, M. P.; Thiyagarajan, P.; Littrell, K. C. *Langmuir* 2003, **19,** 9592-9599.

[6] Zilberman, B. Y.; Fedorov, Y. S.; Kopyrin, A. A.; Arkhipov, S. A.; Blazheva, I. V.; Glekov, R. G. *Radiochemistry* 2001, **43,** 172-174.

[7] Moyer, B. A. *Solvent extraction: fundamentals to industrial applications;* Proceedings of ISEC 2008 International Solvent Extraction Conference **v. 1-2;** Canadian Institute of Mining, Metallurgy and Petroleum, 2008.

[8] Shukla, J. P.; Misra, S. K. *Indian J. Chem., Sect. A: Inorg., Bio-inorg., Phys., Theor. Anal. Chem.* 1995, **34,** 778-786.

[9] Plaue, J.; Gelis, A.; Czerwinski, K.; Thiyagarajan, P.; Chiarizia, R. *Solvent Extr. Ion Exch.* 2006, **24,** 283-298.

[10] Chiarizia, R.; Jensen, M. P.; Rickert, P. G.; Kolarik, Z.; Borkowski, M.; Thiyagarajan, P. *Langumir* 2004, **20,** 10798-10808.

[11] Nave, S.; Mandin, C.; Martinet, L.; Berthon, L.; Testard, F.; Madic, C.; Zemb, T. *Phys. Chem. Chem. Phys.* 2004, **6,** 799-808.

[12] Kharchenko, S. K.; Mikhailov, V. A.; Afanasiev, Y. A.; Ponomareva, L. I. *Akad. Nauk USSR, IzV. Sibirsk. Otd, Akad. Nauk SSSR, Ser. Khim. Nauk.* 1964, *Chem. Abstr.* **63,** *12384a,* 30-37.

[13] Marcus, Y. *The Properties of SolVents;* John Wiley & Sons: Chichester, 1998.

[14] Warf, J. C. *J. Am. Chem. Soc.* 1949, **71,** 3257.

[15] Horwitz, E. P.; Kalina, D. G.; Diamond, H.; Vandegrift, G. F.; Schultz, W. W. *SolVent Extract. Ion Exch.* 1985, **3,** 75-109.

[16] Choppin, G. R.; Nash, K. L. *Radiochim. Acta* 1995, **70/71,** 225-236.

[17] Beudaert, P.; Lamare, V.; Dozol, J. F.; Troxler, L.; Wipff, G. *Solvent Extr. Ion Exch.* 1998, **16,** 597-618.

[18] Beudaert, P.; Lamare, V.; Dozol, J. F.; Troxler, L.; Wipff, G. *J. Chem. Soc., Perkin Trans. 2* 1999, **11,** 2515-2523.

[19] Schurhammer, R.; Wipff, G. *J. Phys. Chem. A* 2005, **109,** 5208-5216.

[20] Baaden, M.; Burgard, M.; Wipff, G. *J. Phys. Chem. B* 2001, **105**, 11131-11141.

[21] Schurhammer, R.; Wipff, G. *J. Phys. Chem. B* 2011, **115,** 2338-2348.

[22] Cui, S.; de Almeida, V. F.; Khomami, B. *In Solvent Extraction: Fundamentals to Industrial Applications;* Moyer, B. A., Ed.; Canadian Institute of Mining, Metallurgy and Petroleum: Montreal,Quebec, Canada; 2008; pp 1069-1075.

[23] Ye, X.; Cui, S.; de Almeida, V. F.; Khomami, B. *J. Phys. Chem. B* 2009, **113,** 9852-9862.

[24] Ye, X.; Smith, R. B.; Cui, S.; de Almeida, V. F.; Khomami, B. *Solvent Extr. Ion Exch.* 2010, **28,** 1-18.

[25] Ye, X.; Cui, S.; de Almeida, V. F.; Hay, B. P.; Khomami, B. *Phys. Chem. Chem. Phys.* 2010, **12,** 15406-15409.

[26] L. L. Burger, in W. W. Schulz and J. D. Navratil (Eds), Science and Technology of Tributyl Phosphate, CRC Press, Boca Raton, FL, 1984, p. 25.

[27] D. M. Petkovic, B. A. Kezele, and D. R. Rajic, *J. Phys. Chem.,* **77**(1973) 922.

[28] D. M. Petkovic and Z. B. Maksimovic, *J. Inorg. Nucl. Chem.,* **38**(1976) 297.

[29] L. Tsimering and A. S. Kertes, *J. Chem. Thermodyn.,* **6**(1974) 411.

[30] L. Tsimering and A. S. Kertes, *J. Chem. Eng. Data,* **22**(1977) 163.

[31] A. Poczynailo, P. R. Danesi, and G. Scibona, *J. Inorg. Nucl. Chem.,* **35**(1973) 3249.

[32] Choi, K.; Tedder, D. W. *Ind. Eng. Chem. Res.* 1996, **35,** 2048-2059.

[33] D. Dyrssen and D. Petkovic, *J. Inorg. Nucl. Chem.,* **27** (1965) 1381.

[34] D. M. Petkovic, *J. Inorg. Nucl. Chem.,* **30** (1968) 603.

[35] Poczynailo, A.; Danesi, P. R.; Scibona, G. J. *Inorg. Nucl. Chem.* 1973, **35,** 3249-3255.

[36] A. M. Rozen. L. P. Khorkhorina. V. G. Yurkin, and N. M. Novikova, Dokl. Akad. Naulc SSSR, **153** (1963) 1387.

[37] S. Nishimura, C. H. Ke, and N. C. Li, *J. Phys. Chem.,* **72** (1968) 1297.

[38] Rao, P. R. V.; Kolarik, Z. *Solvent Extr. Ion Exch.* 1996, **14,** 955-993.

[39] K. Alcock. S. S. Grimley, T. V. Healy, J. Kennedy, and H. A. C. McKay, *Trans. Farad. Sot.,* **52** (1956) 39.

[40] Osseo-Asare, K. *Adv. Colloid Interface Sci.* 1991, **37,** 123-173.

[41] Erlinger, C.; Gazeau, D.; Zemb, Th.; Madic, C.; Lefrancois, L.; Hebrant, M.; Tondre, C. *Solvent Extr. Ion Exch.* 1998, **16,** 707-738.

[42] Baxter, R. J. *J. Chem. Phys.* 1968, **49,** 2770-2774.

[43] Menon, S. V. G.; Kelkar, V. K.; Manohar, C. *Phys. Rev. A.* 1991, **43,** 1130-1133.

[44] Liu, Y. C.; Chen, S. H.; Huang, J. S. *Phys. Rev. E.* 1996, **54,** 1698-1708.

[45] Chiarizia, R.; Jensen, M. P.; Borkowski, M.; Thiyagarajan, P.; Littrell, K. C. *Solvent Extr. Ion Exch.* 2004, **22,** 325-351.

[46] Motokawa, R.; Suzuki, S.; Ogawa, H.; Antonio, M. R.; Yaita, T., *J. Phys. Chem. B* 2012, **116,** 1319-1327.

[47] Cui, S.; V. F. de Almeida; Benjamin P. Hay; Bamin Khomani, *J. Phys. Chem. B* 2012, **116,** 305-313.

[48] Marcus G. Martin; J. Ilja Siepmann, *J. Phys. Chem. B* 1998, **102,** 2569-2577.

[49] L Martinez, R Andrade, EG Birgin, JM Martinez, *Journal of Computational Chemistry,* **30,** 2157-2164, 2009.

[50] S.J. Plimpton, *J. Comp. Phys.*, **117**, 1 (1995).

[51] Tian, Q. L.; Liu, H. Z. *J. Chem. Eng. Data* 2007, **52,** 892-897.

[52] M. Estrada, G. Silva, K. Hall, F. Borja, *J. Chem. Eng. Data* 2011, **56,** 4461-4465.

[53] W. Humphrey, A. Dalke, K. Schulten, *J. Molec. Graphics*, **14**, 33 (1996).

[54] C.T. Chantler, K. Olsen, R.A. Dragoset, J. Chang, A.R. Kishore, S.A. Kotochigova, D.S. Zucker, (2005), X-Ray Form Factor, Attenuation and Scattering Tables (version 2.1). [Online] Available: http://physics.nist.gov/ffast [2009, October 26]. National Institute of Standards and Technology, Gaithersburg, MD. Originally published as C.T. Chantler, J. Phys. Chem. Ref. Data 29(4), 597-1048 (2000); and C.T. Chantler, J. Phys. Chem. Ref. Data 24, 71-643 (1995).

Chapter 3

Ab initio derived charges to refine force field for ionic liquids

3.1 Introduction

In recent years, room temperature ionic liquids (ILs) have sparked widespread interest as fluids with wide ranging applications. Due to their unique properties such as low melting points, negligible vapor pressure, non-flammability and good ionic conductivity, the resulting possibility of manifold applications including catalysis,[1] electrochemistry,[2] separation technologies,[3] molecular materials,[4] or performance chemicals[5] has stimulated extensive study on this group of compounds during the past decade.[6] From a physical point of view, ILs are a subclass of molten salts, which have a melting point below 100 °C, that often consist of bulky organic cations and inorganic anions. A combination of an imidazolium-based cation containing a methyl group at one of the nitrogen and a long alkyl side chain at the other nitrogen, is a common component of ILs. The properties of ILs can be changed in two different ways. First, varying the alkyl tail length allows the possibility to tune the solvent and the second way to influence the solvent properties is the choice of anion.

Most often, these anions are heteroatomic, few examples are BF_4^-, Tf_2N, PF_6^- or SCN etc.

The most powerful tool to obtain an atomic-level understanding of complex systems is molecular simulation. Molecular simulation methods at various theoretical levels have been widely used to examine ILs, these range from ab initio calculations,[7–9] ab initio molecular dynamics (AIMD),[10–20] to classical molecular dynamics simulations. Ab initio and density functional theory (DFT) calculations of ILs provides accurate intra- and intermolecular interaction information. But, these calculations demand huge computational cost, because of this fact application of these methods are usually limited to small size systems and to short time scales. Molecular dynamics simulations on the other hand, have been performed on systems consists of hundreds or thousands of ILs pairs over nanosecond or even microsecond time scales. The classical molecular dynamics approaches employed various kinds of force fields, such as OPLS,[21] AMBER,[22] GROMACS,[23] CHARMM,[24] Lopes,[25–29] Wang,[30] including polarizable ones,[31] and multiscale coarse-graining models[32,33] also. These simulation studies revealed that the dynamics of the ILs modelled using these force fields are consistently too slow, relative to experiments.

Ionic liquids are characterized by the interplay of different physical and chemical interactions which have been identified with Coulomb, van der Waals, π stacking interactions as well as hydrogen bonding. Hydrogen bonds and van der Waals forces are weaker and short-ranged while, Coulomb interactions are stronger and long-ranged. In simple salts like sodium chloride, Coulomb interactions dominate over the van der Waals interactions; on the contrary, in molecular solvents with neutral building blocks, such as water, van der Waals forces as well as hydrogen bonding dominates over the Coulomb interactions. But in the case of ILs, all the three different kinds of interactions play crucial roles giving rise to their unique properties.

The electrostatic interaction in ILs determines their unique properties such as low vapor pressure and good ionic conductivity. We know there is a large probability of charge transfer and polarizability in ionic species. Because of this, the effective charges on cations and anions in the bulk phases are smaller than unity.[34,39,40] Experimental findings also supports this phenomenon in ILs.[41,42] Charge transfer and polarizability are treated implicitly in ab initio or DFT calculations. But in case of classical MD simulations, traditionally atomic charges were derived from quantum chemical calculations of an ion or an ion pair studied in gas phase. Condensed phase polarization will not be captured in such calculations, leading to erroneous estimates of effective charge on the ions. Typically, the cation and anion possess unit charges in such an approach, which enhances the stability of the crystalline or liquid phase in condensed phase calculations. Such approaches also were found to diminished values of diffusion coefficients of ions relative to experimental measurements.

The first remedy to handle the effect of electronic polarizability in ILs was the introduction of polarizable force fields. Voth et al.[38] came up with polarizable force fields, which gives a much faster diffusive behavior by a factor of three compared with the nonpolarizable model. This is because in the polarizable force field reduces the cage effect responsible for trapping ions in a local cage. Recently Borodin[58] has developed polarizable force fields for more ionic liquids. But polarizable force fields are very difficult to develop and they are much more computationally expensive than the fixed charge models. A possible alternative treatment of charge transfer and polarizability for standard nonpolarizable force fields consists of an overall charge scaling of the atomistic partial charges, which gives rise to an ionic charge deviation from ±1 e. The dynamics of the liquid gets speeded up because of the lower electrostatic binding and this technique has been implemented for ionic liquids force fields by several groups.[34,59,61] Most of force fields were obtained by applying a uniform scaling factor to the unit charges. A liquid phase AIMD simulation,[40] fit to experimental density or other system properties[62] has been the way for most of the cases to determine this scaling factor. Most often within each molecule, the atomic charge distribution were left unchanged from those derived from gas phase quantum chemical calculations.

Kossmann et al.[63] have used second-order Møller-Plesset perturbation theory (MP2) and density functional theory (DFT) techniques to study [DMIM][Cl] clusters and they found a reduced charge of the chloride of about -0.823 e. An ab initio molecular dynamics simulation of [DMIM][Cl] followed by a Mulliken population analysis performed by Bühl et al.[11] also gives a reduced charge between -0.7 and -0.8e for the chloride. However, the shortcomings of methods such as Mulliken, Löwdin or natural population analysis (NPA) are known to be highly basis set dependent and unpredictable with marked fluctuations in the partial charges.[64] There is a different method also to calculate charges which is based on the fitting of the electrostatic potential (ESP) in the vicinity of a molecule. In this procedure, the potential at some points around the molecule are chosen and atomic charges are adjusted such as to reproduce the ESP. There are three major algorithms used for calculating RESP atomic charges: ChelpG,[65] Connoly,[66] and Geodesic.[67] The main difference stems from the way these algorithms select the points on the ESP surface for the fitting procedure. As a simple point charge cannot replace a charge density when approaching the respective atom, points that are too close to the molecule have to be excluded in this method. Hence, this is a good method for isolated molecules but an insufficient one for the bulk. A relatively recent approach for calculations of charge distribution is that of Richard Bader's; referred to as Atoms-in-Molecules (AIM) theory[68] which uses zero-flux surfaces to divide atoms. This procedure also becomes more tedious for bulk systems than for ion pairs.

The bulk phase environment is affected by the charge transfer and polarization. In this regard, Delle site and co-workers have suggested a new method to calculate atomic charge distribution from liquid phase AIMD simulation directly.[69–71] They have used the Blöchl[72] method for snapshots derived from a CPMD trajectory to derive atomic charges. In this way the liquid phase charge distribution gets automatically involved but it depends on the proper sampling of the configurational space. In the Blöchl method, atomic charge is derived from the analysis of reciprocal space charge density and hence, there is no need of exclusion of real space points. Therefore, this method is perfectly suited for use under periodic boundary conditions.

In spite of these efforts, the development of atomic charges for ILs is still a subject under intense development. In the present work, we present a simple, effective and systematic method to derive atomic charges for ionic liquids. The atomic charges of ionic liquids were derived from AIMD simulation on their crystal phase. These charges were compared with the charges obtained from liquid phase classical MD simulation. In both the cases we obtain a set of reduced atomic charges for ionic liquids. In cases where the experimental crystal structure is unknown, we propose that liquid state configurations can be obtained from a classical MD trajectory generated with any reasonable force field. DFT calculations on snapshots of such configurations too can yield the correct set of atomic charges.

3.2 Computational Details

The complete procedure developed by Blöchl,[72] was for electrostatic decoupling of periodic images within a plane-wave based density functional theory (DFT) code. The basic idea of this procedure is to use the multipole moments of separated charge densities to express the interaction between them. In the following, we provide a brief description of the method as discussed in Refs.[72] and Refs.[69]

We know that under periodic boundary conditions, the electrostatic interactions can be treated efficiently in the reciprocal representation. Hence, the charge density $n(\mathbf{r})$ is always available in both real and reciprocal space in a plane-wave-based calculation. In reciprocal space, the multipole moments of a charge density is expressed by the derivatives of the charge density around the lattice vector $\mathbf{G} = \mathbf{0}$. It is difficult to derive atomic partial charges because the basis functions cannot easily be assigned to certain atoms. However, it was proposed that a model charge density[69] $\tilde{n}$ which is composed of Gaussian functions $g_i(\mathbf{r})$, centered at each atomic site can be constructed as,

$$\tilde{n}(\mathbf{r}) = \sum_{\mathbf{i}} \mathbf{q_i g_i}(\mathbf{r}) \tag{3.1}$$

The interactions between the original density and surrounding charges have to represented correctly, i.e., their multipole moments have to be reproduced by $\tilde{n}$. This is done by fitting the reciprocal density around $\mathbf{G} = \mathbf{0}$. The parameters of $\tilde{n}$ and q_i values are obtained from extremum condition of

$$F(q_i, \lambda) = \frac{V}{2} \sum_{\mathbf{G} \neq 0} w(\mathbf{G}) \mid n(\mathbf{G}) - \sum_i q_i g_i(\mathbf{G}) \mid^2 - \lambda [n(\mathbf{G} = 0)V - \sum_i q_i g_i(\mathbf{G} = 0)V] \tag{3.2}$$

where $w(\mathbf{G})$ is a weighting function which rapidly decays with increasing $\mathbf{G}$, V is the volume of simulation box, and λ is a Lagrangian multiplier. The desired atomic partial charges are obtained by summing all q_i values for the considered atom once the model density is optimized. There is no need to exclude any real space points in this method (which is necessary in other methods) and the actual fitting is carried out in reciprocal space. For bulk systems, this method is appropriate as they are usually simulated under periodic boundary conditions. Blöchl suggested using 3-4 Gaussians per atomic site to get very accurate charges. In the present work, we used four Gaussians per atomic site and the cutoff value was set to 3.5E_h (7 Ry). The smallest radius of the Gaussian used in our calculation was set to a value of 0.5a_0 or 0.2645 Å. Radius of all other Gaussians were obtained by multiplying the previous decay length with progression factor of 1.5.

Atomic charges were derived from AIMD calculations. Density functional theory (DFT) calculations were carried using CP2K software.[73] All valence electrons were treated with triple-zeta double-polarized basis and a density cutoff of 280 Ry was used. Exchange and correlation effects were considered through the Perdew, Burke and Ernzerhof (PBE) functional. Geodecker-Teter-Hutter (GTH) pseudopotentials[74] were used to consider the effect of core electrons and nuclei. Initial cell parameters and atomic positions were taken from Cambridge structural database.[37–39] Depending on the magnitude of the cell parameters, two replicas in the corresponding direction were used for building a supercell. A description of all the systems studied here is provided in Table 3.1. Each of them was optimized by varying the cell parameters and coordinates iteratively until an energy minimum was found. Convergence criteria of 10^{-7} and 10^{-4} were employed for the gradient of the wave functions and for the force on the nuclei respectively. On the final geometries, atomic charges were calculated using the Blöchl[72] approach implemented in CP2K. This set of charges will be referred to as charge-a.

Table 3.1: Summary of the cell parameters and supercell dimension of all the systems being studied.

System	Cell parameter						Supercell
	a, Å	b, Å	c, Å	α	β	γ	
[MMIM][Cl]	8.652	7.858	10.539	90.0	106.34	90.0	(2x2x1)
[MMIM][PF_6]	11.254	9.361	17.986	90.0	90.0	90.0	(1x2x1)
[BMIM][PF_6]	8.755	8.904	9.013	95.810	114.955	103.061	(2x2x2)
[BMIM][CH_3SO_3]	7.934	8.480	10.278	103.404	99.567	111.620	(2x2x1)
[BMIM][CF_3SO_3]	10.222	12.534	22.541	90.0	93.281	90.0	(1x1x1)
[BMIM][Cl]	10.113	11.411	8.328	90.0	90.0	90.0	(1x1x2)
[EMIM][PF_6]	8.627	9.035	13.469	90.0	101.92	90.0	(2x2x1)
[EMIM][HCO_3]	7.448	7.602	8.164	90.627	101.339	109.740	(2x2x2)
[EMIM][BF_4]	8.762	9.396	11.425	90.0	98.720	90.0	(2x2x1)
[EMIM][NO_3]	4.540	14.810	13.445	90.0	95.74	90.0	(3x1x1)
[EMIM][NO_2]	7.870	6.752	8.517	90.0	114.21	90.0	(2x2x2)
[EMIM][PCl_6]	7.698	12.266	15.018	90.0	101.447	90.0	(2x1x1)

In order to check for charge transferability between the crystalline and liquid phases of the same compound, we also calculated the site charges for liquid configurations generated from classical molecular dynamics runs. Two systems, [MMIM][Cl] and [MMIM][PF_6], containing 42 and 30 ion pairs respectively, were chosen for this purpose. The force field developed by Lopes[25] group was used in the classical MD simulations and they were carried out using the LAMMPS[80] software package. Initial positions of all atoms were generated by placing the molecules randomly in a box of length 20 Å. Equations of motion were integrated with the velocity Verlet algorithm with a time step of 1 fs. To use this large time step, all C-H covalent bonds were constrained using the SHAKE algorithm as implemented in LAMMPS software.[80] A cutoff of 10 Å was chosen for calculating pairwise interactions in real space for those atoms whose distance falls below this value. Long range electrostatic interactions were computed using the particle-particle particle-mesh solver with a precision of 10^{-5}. As prescribed by the Lopes force field, a multiplication factor of 0.5 was used to scale down the non-bonded interactions calculated for pair of atoms which were separated by three bonds. The parameters for cross interactions between different molecular species (atomic groups) were derived using the standard Lorentz-Berthelot rules.[81] Cubic periodic boundary conditions were applied.

Initial configurations were relaxed using standard energy minimization methods. Constant-pressure and constant-temperature ensemble (NPT) simulations were carried out until the convergence of volume. Temperature and pressure of the system were maintained at 300K and 1 atm using Nóse-Hoover thermostat and barostat respectively, with a damping factor of 1 ps. The final coordinates of the NPT run were taken to the constant-volume and constant-temperature (NVT) ensemble for a further equilibration for 5 ns under constant NVT conditions. Finally, an analysis run was generated for 10 ns. Configurations at every 1 ns were chosen for charge calculation using ab initio methods. All systems are visualized using Mercury[40] and VMD.[43]

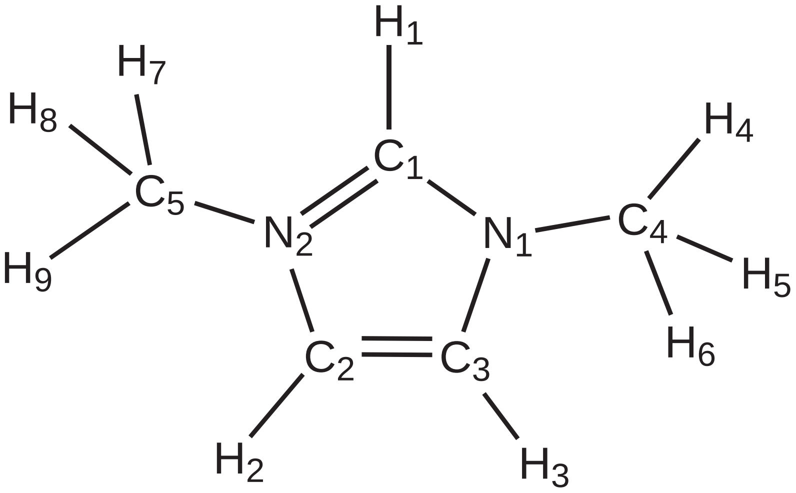

Figure 3.1: Atom labeling in imidazolium ring.

In the ab initio calculations, the wave functions and the force were optimized every step with convergence criteria of 10^{-7} and 10^{-4} respectively. Atomic charges were calculated using the Blöchl approach implemented in CP2K before and after geometry optimization for all the configurations. The charges thus obtained were averaged over all ions and the configurations. These set of atomic charges are hereafter referred to as charge-b and charge-c respectively. The nomenclature used to describe sites on the imidazolium ring is shown in figure 3.1.

3.3 Results and Discussion

3.3.1 Comparison of crystal and liquid charges

For both the systems, the total charge on an ion obtained before and after the optimization of geometry were different. For [MMIM][Cl], the mean values of the charge distribution were ±0.70 and ±0.61 whereas the corresponding values for [MMIM][PF_6] were ±1.01 and ±0.91 respectively. The charges obtained from the liquid simulation after geometry optimization within DFT are closer to the values for the crystal; however, charges obtained before the geometry optimization (i.e., charges calculated for configurations derived from the force field) exhibit significant differences from those of the crystalline state. These are compared in Table 3.2 for the two systems.

Table 3.2: Comparison of crystal and liquid charges in [MMIM][Cl] and [MMIM][PF$_6$].

Atom	charge-a		charge-b		charge-c	
	[MMIM][Cl]	[MMIM][PF$_6$]	[MMIM][Cl]	[MMIM][PF$_6$]	[MMIM][Cl]	[MMIM][PF$_6$]
N1	0.181	0.209	0.122	0.269	0.210	0.256
C1	-0.154	-0.123	0.142	-0.151	-0.144	-0.162
N2	0.140	0.164	0.124	0.254	0.202	0.247
C2	-0.147	-0.193	0.027	-0.189	-0.163	-0.194
C3	-0.073	-0.114	0.024	-0.177	-0.177	-0.182
H1	0.198	0.244	0.040	0.249	0.186	0.251
H2	0.158	0.199	0.041	0.236	0.183	0.237
H3	0.079	0.223	0.047	0.235	0.198	0.234
C4	-0.158	-0.458	-0.111	-0.473	-0.334	-0.454
H4	0.075	0.182	0.059	0.208	0.129	0.187
H5	0.022	0.208	0.059	0.206	0.129	0.191
H6	0.113	0.231	0.059	0.208	0.130	0.190
C5	-0.194	-0.334	-0.110	-0.482	-0.328	-0.458
H7	0.113	0.142	0.059	0.204	0.130	0.188
H8	0.101	0.131	0.059	0.208	0.127	0.189
H9	0.064	0.148	0.058	0.210	0.129	0.193
Cl/PF$_6$	-0.520	-0.856	-0.701	-1.016	-0.607	-0.916

Now, if we compare these three charge distributions, we can see that the ion charges obtained from liquid phase classical simulation after geometry optimization within DFT (charge-c) were comparable to those obtained from the crystal simulation (charge-a). In fact, in many a case, charge-a and charge-b have opposite signs, while the sign of charge-c is identical to that in charge-a. This behavior is reflected in the total ion charges as well. The anion charge of charge-b is farther from that of charge-a, while that of charge-c is comparable to that in charge-a. It reflects the fact that configurations accessed by the force field are not quite representative of the liquid state, and the near neighbor arrangements are improved with the DFT approach. In figure 3.2 we have plotted the distribution of the total charge on all the ions obtained from the liquid phase classical simulation (after geometry optimization within DFT). The data is averaged over all the ions and configurations. The interesting part of this plot is the mean value of this charge distribution. For both the systems, we found that the ion charges obtained from the crystal simulation is very close to the mean value of the charge distribution in the liquid state. This observation opens a window of opportunity. If the crystal structure of a particular salt (IL) is undetermined, we can still obtain the site charges for the ions present therein. We can carry out simulations of its liquid state using a reasonable force field, select configurations from its trajectory, quench them to their local minima within periodic DFT (geometry optimization) and derive the Blochl charges.

Based on the argument presented above, we chose eight different ILs for which the crystal structures are not known. We followed the same procedure as described for [MMIM][Cl] and [MMIM][PF_6] in these calculations. Since the geometry optimization of the bulk liquids within DFT cannot be carried out for large system sizes, liquids containing 30 to 40 ion pairs were considered in these simulations. Again, the Lopes-Padua force field[25] was employed. Furthermore, since the interaction cutoff has to be less than half box length, we have used a pairwise cutoff distance of 10Å in these classical MD simulations. The densities of the systems compared well against experimental data. The wave functions and the force were optimized every step with convergence criteria of 10^{-6} and 10^{-3} respectively, in all the ten configurations generated from liquid simulation for all the systems. Later, the chargeswere calculated using the Blöchl approach as discussed earlier. Details of these calculations and the charges obtained are summarized in Table 3.3.

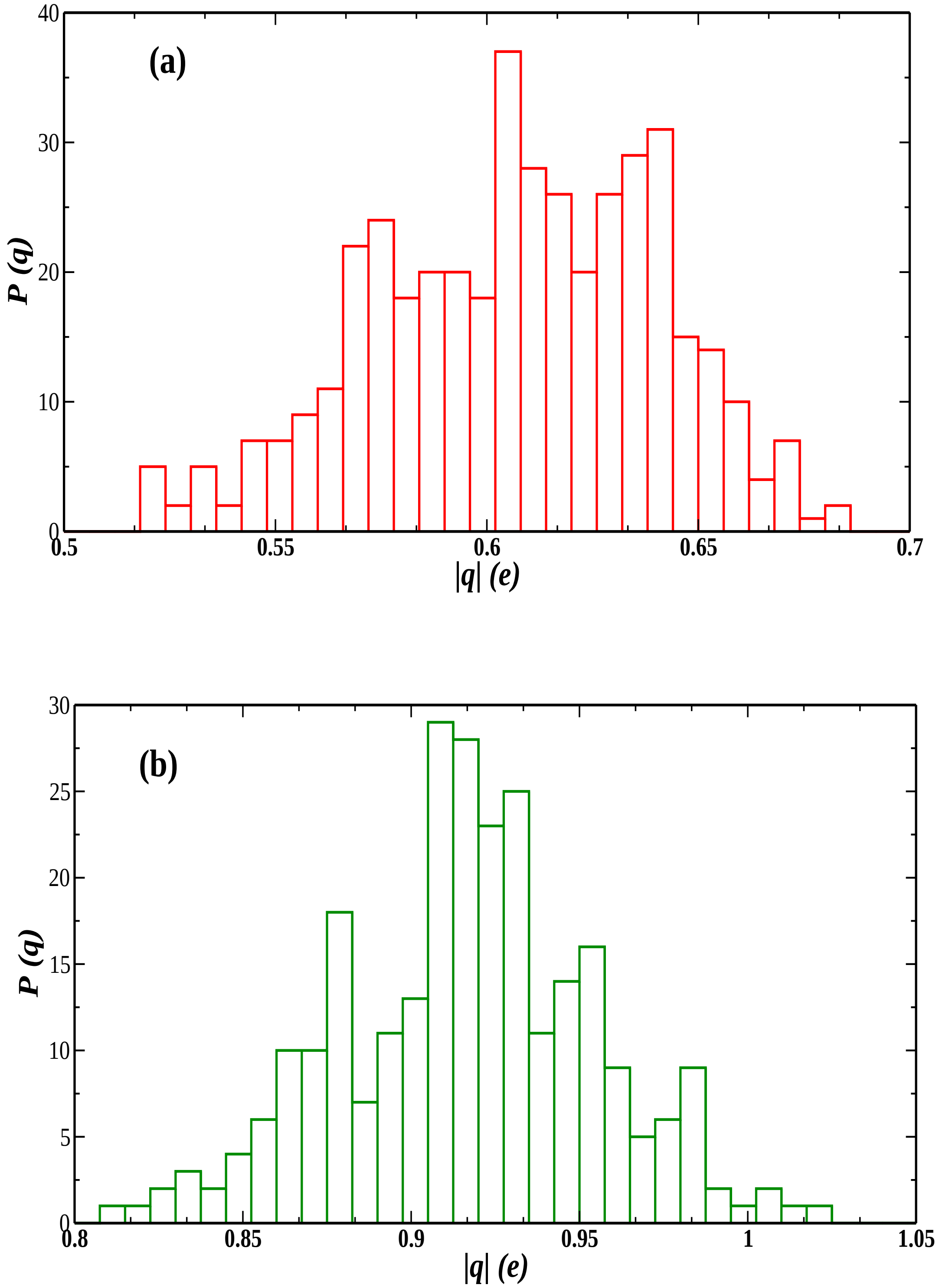

Figure 3.2: Distribution of total ion charges obtained from liquid phase classical simulation for (a) [MMIM][Cl] and (b) [MMIM][PF_6].

Table 3.3: Charges calculated for snapshots obtained from liquid phase classical simulations.

System	No. of ion pairs in the liquid	Charge-b [e]	Charge-c [e]
[MMIM][BF_4]	36	±0.918	±0.799
[MMIM][NO_3]	45	±0.821	±0.645
[MMIM][NTf_2]	25	±0.815	±0.730
[EMIM][Cl]	40	±0.686	±0.587
[EMIM][NTf_2]	21	±0.771	±0.667
[BMIM][BF_4]	28	±0.879	±0.774
[BMIM][NO_3]	30	±0.780	±0.631
[BMIM][NTf_2]	18	±0.802	±0.696

3.3.2 Radial distribution functions

We have calculated the radial distribution functions for two different systems, [MMIM][Cl] and [MMIM][PF_6] using two set of configurations. Those configurations were same as used for calculating charges, generated from liquid phase simulation; before and after geometry optimization. Radial distribution functions (RDFs) for these two systems are given in Figure 3.3 and Figure 3.4.

For all the cases the cation is represented by the center of imidazolium ring, HA represents the acidic proton (H2) and the non-acidic protons (H3 and H4) are represented by H. In both the systems, we observed a slight increase in the intensity in cation-anion RDF obtained from the configurations after geometry optimization. The anion-anion RDF obtained from configurations after quenching also exhibit difference with that from configurations before quenching. The anions approach each other closer in the after geometry relaxation. These effects were also observed by Bhargava et al.,[60] they performed CPMD run for [BMIM][PF_6] and compared with the results obtained from classical simulation for same system and found this differences.

Crucial differences were noticed in the RDFs between acidic proton (H2) and

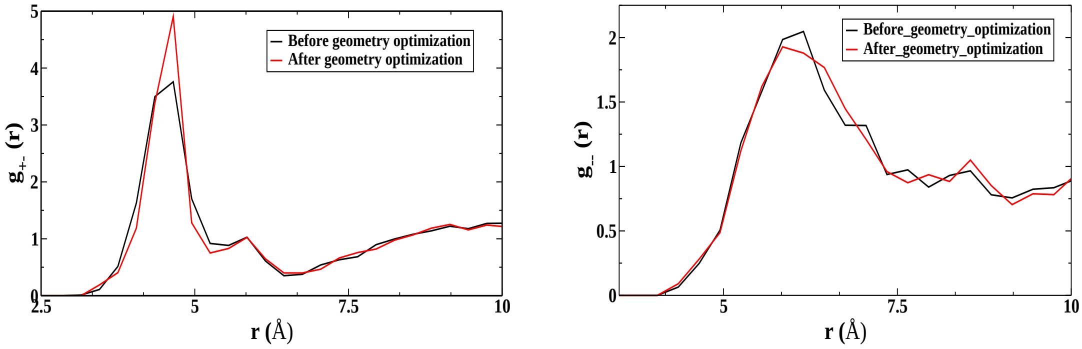

(a) g_{cat-an}(r) (b) g_{an-an}(r)

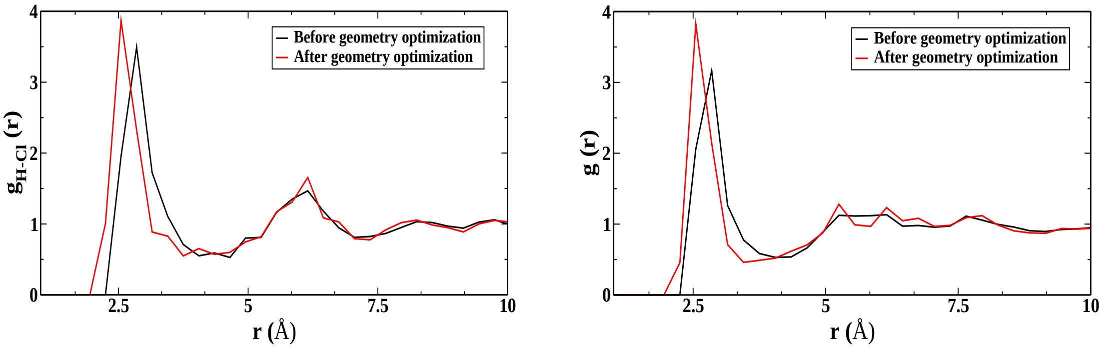

(c) g_{HA-Cl}(r) (d) g_{H-Cl}(r)

Figure 3.3: Radial distribution function derived for [MMIM][Cl] using configurations before and after geometry optimizations.

chlorine ([MMIM][Cl]) or fluorine ([MMIM][PF_6]) in the two systems. After relaxation, there was a clear shift towards smaller distances was observed in the position of first peak. Thus it is evident that the acidic proton forms a hydrogen bond with the chlorine or fluorine atom of anion. This hydrogen bond can be characterized as "weak" hydrogen bond on the basis of distance between the two atoms. This was also observed in previous literature reports.[59,60]

3.3.3 Crystal densities

The cell parameters of all the systems were optimized to the energy minimum. The cell parameters obtained from DFT compare extremely well against experiment. Given that ionic liquids exhibit varied interactions including electrostatic, van der

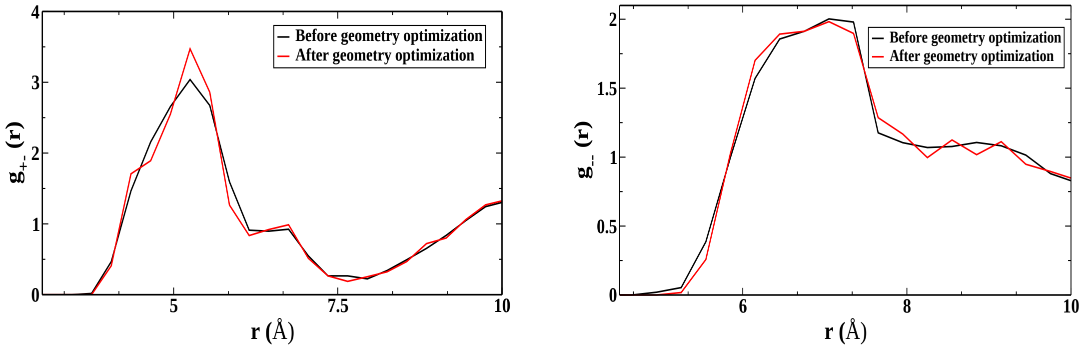

(a) g_{cat-an}(r) (b) g_{an-an}(r)

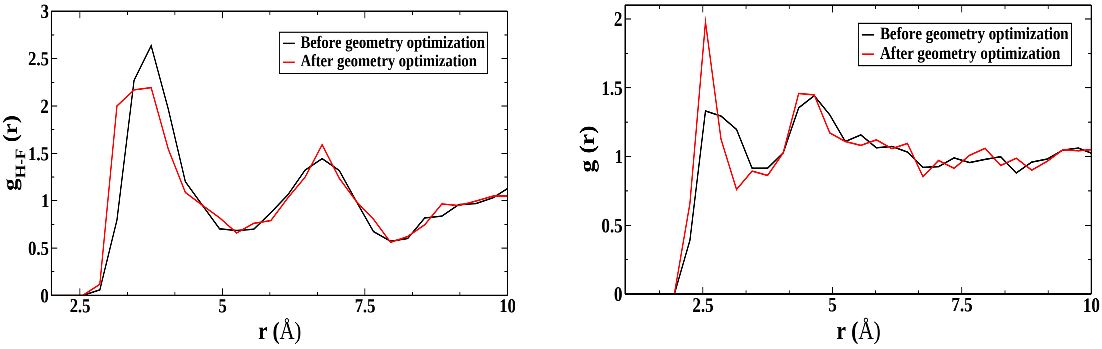

(c) g_{HA-F}(r) (d) g_{H-F}(r)

Figure 3.4: Radial distribution function derived for [MMIM][PF$_6$] using configurations before and after geometry optimizations.

Waals, hydrogen bonding, π stacking etc., the good match demonstrates the robustness of the calculations and the protocols to describe the interactions in ionic liquids precisely. Results from computation are compared with experimental data in Table 3.4. Except for a few systems, the predicted density from DFT match the experimental values.

3.3.4 Atomic charges

Charge transfer between ions : We know that the basicity and polarizability of anions are related, i.e., as the basicity of anions increases, their polarizability too increases.[89] Now, if an anion becomes more polarizable, then the electron density around it gets distorted easily by the electron withdrawing character of cations surrounding that anion. Thus, we can expect a greater charge transfer between a

Table 3.4: Comparison of the cell parameters and crystal densities.

System	Cell parameter						Density (g/cc)		
	Δa(%)	Δb(%)	Δc(%)	$\Delta\alpha$(%)	$\Delta\beta$(%)	$\Delta\gamma$(%)	ρ_{Exp}	ρ_{Sim}	$\Delta\rho$(%)
[MMIM][Cl]	0.02	0.42	0.13	0.0	0.04	0.0	1.281[43]	1.288	0.55
[MMIM][PF_6]	0.0	0.22	0.31	0.0	0.0	0.0	1.698[44]	1.706	0.47
[BMIM][PF_6]	0.69	0.51	0.28	0.04	0.11	0.07	1.560[45]	1.58	1.2
[BMIM][CH_3SO_3]	0.87	0.64	1.54	0.02	0.04	0.12	1.296[46]	1.33	2.4
[BMIM][CF_3SO_3]	0.7	0.11	0.36	0.0	0.03	0.0	1.328[47]	1.34	0.90
[BMIM][Cl]	1.71	2.46	0.88	0.0	0.0	0.0	1.207[48]	1.27	5.2
[EMIM][PF_6]	1.14	2.38	1.72	0.0	0.81	0.0	1.656[49]	1.58	4.7
[EMIM][HCO_3]	0.25	1.21	0.16	0.2	0.08	0.19	1.345[50]	1.365	1.45
[EMIM][BF_4]	0.65	0.76	0.13	0.0	0.04	0.0	1.414[47]	1.435	1.4
[EMIM][NO_3]	0.59	0.202	0.07	0.0	0.396	0.0	1.279[51]	1.289	0.782
[EMIM][NO_2]	0.953	3.58	0.67	0.0	0.13	0.0	1.265[51]	1.33	5.14
[EMIM][PCl_6]	0.42	1.11	0.323	0.0	0.51	0.0	1.696[52]	1.735	2.29

cation and an anion. The charge transfer leads to a reduction in the total charge of the ions.

Our calculations reveal a clear trend in the atomic charges for three different ionic liquids possessing a common anion, ([PF_6]). The systems investigated were [MMIM][PF_6], [EMIM][PF_6] and [BMIM][PF_6]. The charges of the five ring atoms and the three hydrogens directly attached to the imidazolium ring exhibit the trend which can be seen in Table 3.5.

Table 3.5: Comparison of atomic charges.

Atom	Charges in different systems		
	[MMIM][PF_6]	[EMIM][PF_6]	[BMIM][PF_6]
N1	0.201	0.360	0.450
C1	0.164	0.065	0.110
N2	-0.114	-0.183	-0.207
C2	-0.124	-0.241	-0.311
C3	-0.193	-0.069	-0.141
H1	0.244	0.241	0.228
H2	0.199	0.191	0.298
H3	0.223	0.183	0.158

The nitrogen connected to the longer alkyl group is referred to as N2. As the chain length increases, we expect a larger electron cloud near this nitrogen atom, because of the strong positive inductive effect of the alkyl tail. As a result, the total positive charge on imidazolium ring would decrease, as can be seen by summing the charge on the five atoms constituting the imidazolium ring. Further, we can observe that the charge on all the three carbon atoms of the imidazolium ring are negative. So, the charge imbalance within the ring increases with increasing alkyl group length. To compensate this decrease in charge of the ring and to maintain the total positive charge on the ring, we may expect an increase in positive charge on the other nitrogen (N1) of the ring, on which a single methyl group is attached for all the three systems. Our calculations show the same trend in the nitrogen atom (N1) charge as surmised; the positive charge on the nitrogen (N1) atom increases as the alkyl tail length increases and the difference between charges on two nitrogens increases in the same manner.

Based on the previous reasoning, we may also expect an effect on the charge of the carbon and hydrogen atoms, which are close to the larger alkyl tail. These atoms are C1, C2, H1 (acidic proton) and H2. Our results show that the negative charge increases for the two carbon atoms whereas the positive charge on the acidic proton decreases as the alkyl tail length increases. These can also be explained by the same positive inductive effect of the alkyl tail. However, this trend was not found in case of the other hydrogen (H2). This may be due to some other reason which is still unknown to us.

3.3.5 Ion charges

Kamlet-Taft parameter: In the previous section, we discussed some trends in the atomic site charges for few ionic liquids having a common anion. Now, we would like to better understand the total charge on the ions. For this purpose, we studied the crystals of different ionic liquids keeping the same cation and varying the anion. The total charge on the ions of these systems were compared against the spectroscopically (experimental) determined Kamlet-Taft parameter of the ionic liquids. Kamlet-Taft[87–89] is one of the most comprehensive and widely used solvent scales for the understanding and prediction of solvent behavior. There are three parameters in the Kamlet-Taft scale. Those are the hydrogen bond donating ability α, the hydrogen bond acceptor ability β, the dipolarity-polarizability π^* and a correction term, δ, to the dipolarity-polarizability to account for variations in solvent polarizability within a given solvent class.

The Kamlet-Taft parameter π^* is calculated by measuring the wavelength of maximum absorbance, υ_{max} in kK (kilokeyser, 10^-3 cm^-1), of the dye N,N-diethyl-4-nitroaniline:

$$\pi^* = \frac{\upsilon_{max} - \upsilon_0}{s} \tag{3.3}$$

here υ_0 is the regression value for a reference solvent system and s is the susceptibility of the intensity of spectral absorption due to changing solvent dipolarity/polarizability.

Kamlet-Taft parameter α is obtained by:

$$\alpha = \frac{(E_T(30) - 14.6(\pi^* - 0.23) - 30.31)}{16.5} \tag{3.4}$$

α is a measure of a solvent's hydrogen bond donating acidity.

The Kamlet-Taft parameter β is determined by measuring the relative difference of solvatochromism between 4-nitroaniline (1) and N,N-diethyl-4-nitroaniline (2):

$$\beta = \frac{(1.035\upsilon(2)_{max} - \upsilon(1)_{max}) + 2.64}{2.8} \tag{3.5}$$

where $\upsilon(1)_{max}$ and $\upsilon(2)_{max}$ are the wavelengths of the maximum absorbance of dissolved 4-nitroaniline and N,N-diethyl-4-nitroaniline, respectively. The β parameter gives a measure of a solvent's hydrogen bond accepting basicity.

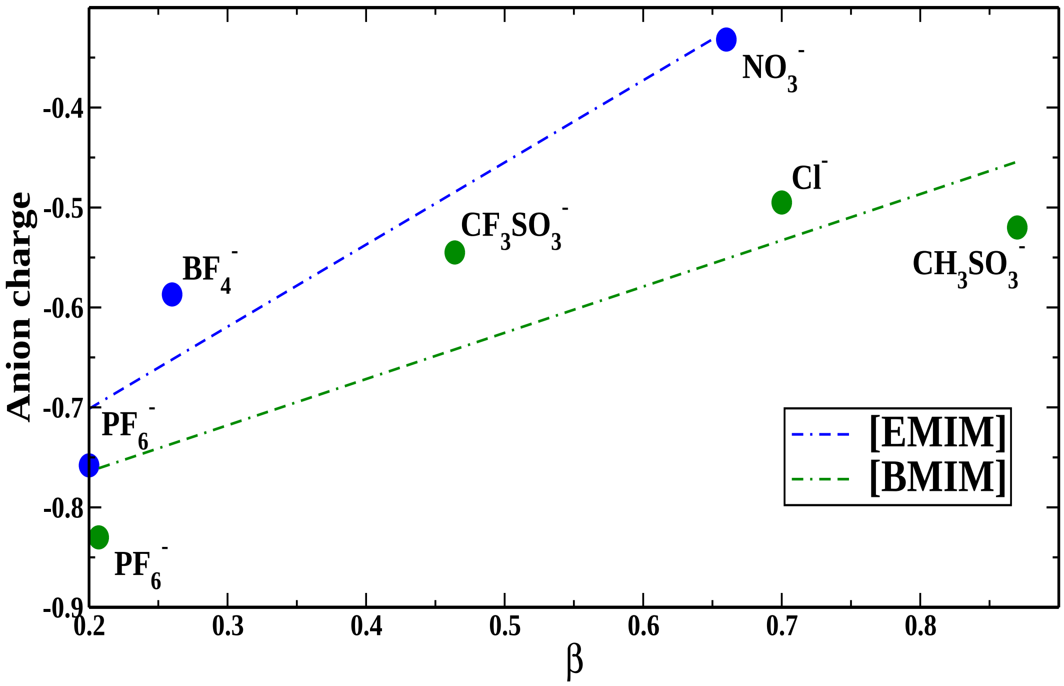

Figure 3.5: Variation in total ion charge against β value for ionic liquids having $[\mathrm{EMIM}]^+$ and $[\mathrm{BMIM}]^+$ as common cation with different anions.

Among all these parameters, the one that determines the hydrogen bond acceptor ability, which is β, is extremely important for the prediction of anion behavior. We have examined many crystals in which the cations were either $[\mathrm{EMIM}]^+$ or $[\mathrm{BMIM}]^+$, with different kinds of anions. The ion charges in the crystalline state were calculated as before and are plotted against the experimentally determined β value for the liquid state of the corresponding salt.

From Figure 3.5, it is clear that there is a correlation between the ion charge and the β parameter for the two classes of ionic liquids having different cations. In both the cases, the ion charge decreases as the value of the β parameter increases and hence, a linear relationship is found between the computed ion charge in the crystalline state and the experimentally determined β of the corresponding liquid.

There is an another series in ions known as the Hofmeister series,[90,91] which is a classification of ions based on their ability to decrease or increase the solubility of non-polar molecules. In particular, in aqueous salt solutions, solubility is intricately

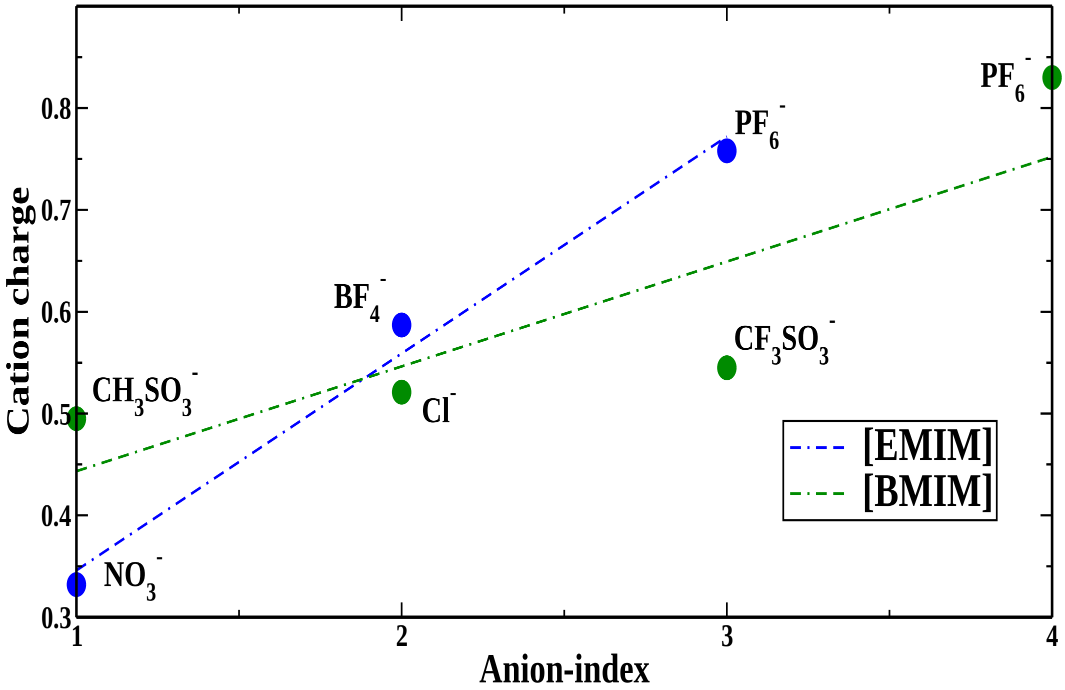

Figure 3.6: Variation in total ion charge along the Hofmeister series anions for $[EMIM]^+$ and $[BMIM]^+$ based ionic liquids.

tied to the hydrophobicity of the solute. Among the anions studied herein, the following ranking of solubility in water is known from literature:

$$CH_3SO_3^- > Cl^- > CF_3SO_3^- > NO_3^- > BF_4^- >> PF_6^-.$$

Given a cation (either $[EMIM]^+$ or $[BMIM]^+$), we can also examine the total ion charge obtained in the crystalline state against the position of the anion in the Hofmeister series. The same is shown in Figure 3.6.

From the Figure 3.6 it is clear that the total ion charge is increasing along the Hofmeister series. Hence, the fact what we can understand from these two comparison is that, an ionic liquid for which we don't have the ion charge, we can easily have guess value or we can estimate it comparing with these two series.

3.3.6 Density

The crystal phase of few ionic liquids was simulated using the new set of atomic charges at the temperature at which the crystal structure was measured. We took the force field developed by Lopes,[25] with change in the atomic charges only, all other parameters were kept original as in that force field. In all the cases, crystal structures were found to be stable. The equilibrium lattice parameters are summarized in Table 3.6. For all the ILs, the new set of charges predicted lower density than the experimental results. Thus, although the charges obtained are realistic of the condensed state, the non-bonded interaction parameters of the Lopes-Padua force field need to be refined to take into account the new set of charges.

Table 3.6: Calculated lattice parameters and density for ILs (Length in Å and Angle in degree), using new set of charges and the rest of the force field the same as in Ref.[25]

System	Cell parameter						Density	
	a	b	c	α	β	γ	ρ_{Exp}	ρ_{Sim}
[EMIM][NO_3]	4.633	15.116	13.723	89.999	95.739	89.99	1.279[51]	1.202
[EMIM][PF_6]	8.805	9.3940	13.776	89.999	103.04	89.99	1.656[49]	1.532
[BMIM][Cl]	10.563	11.748	8.5790	89.999	89.999	89.99	1.207[48]	1.089
[BMIM][PF_6]	8.948	9.101	9.212	95.809	114.95	103.0	1.560[45]	1.461
[BMIM][CH_3SO_3]	8.048	8.602	10.426	103.40	99.567	111.6	1.296[46]	1.241

In a similar approach, i.e., using the new set of charges with the original non-bonded and intramolecular parameters, we have also simulated few ILs in their liquid phase. The densities were calculated during a constant-NPT run post the convergence of the volume. As observed in the case of crystalline phase, the densities of the liquid phase too modelled likewise were lower than the experimental values. The same are provided in Table 3.7. It should be noted that the Lopes[25] force field predicts the liquid densities rather accurately (which we have confirmed as well); however, subtle interactions, including the cation-anion hydrogen bonding have been demonstrated to be lacking in that force field. The current approach of partial charges obtained from ab initio calculations of the crystalline phase holds considerable promise in reproducing such intricate interactions. However, the deviation in the density points to the need for refining the non-bonded interactions which have been illustrated earlier by Bhargava and Balasubramanian[59] as well.

Table 3.7: Comparison of liquid phase densities obtained from reduced set of charges (and original non-bonded parameters) against that from experiments and the original Lopes force field.

System	Density (gm/cc)		
	Exp.	Lopes	Reduced charge
[EMIM][BF_4]	1.280[53]	1.099	1.010
[EMIM][PF_6]	1.558[54]	1.380	1.308
[BMIM][Cl]	1.075[55]	1.045	0.919
[BMIM][PF_6]	1.360[56]	1.340	1.305
[BMIM][CF_3SO_3]	1.294[57]	1.358	1.267

3.3.7 Liquid phase structure

The liquid phase structure of [BMIM][PF_6] was studied in terms of radial distribution functions (RDFs) using both the original Lopes force field as well as with a combination of the new set of charges and Lopes non-bonded and intramolecular parameters. The cation-anion g(r) exhibits a sharp peak at about 5.0 Å and a shoulder at 6.8 Å which indicates a well organized liquid structure. The ordering exists up to 20 Å because of the presence of long-range electrostatic interaction. The height of the first peak decreased slightly and the shoulder structure at 6.8 Å became less clear in case of reduced charges compared to the original Lopes parameters. Further, the peak position was slightly shifted towards higher distances, upon the reduced charge. Earler literature results too suggested decreased structuring in the liquid when simulated with reduced atomic charges.[83] Hence, our result is consistent with the reported ones. The cation-cation and anion-anion RDFs show differences going from original Lopes parameters to Lopes parameters with reduced charge. This happens because of the presence of different packing structures between cations and anions when they are simulated with different charges. We also saw the difference in the relative heights of the split peaks of the first neighbor shell in the anion-anion RDFs, when charges were reduced. In case of RDFs between acidic proton and any fluorine of anion, the results are almost similar to the cation-anion RDFs. Here too, peak heights were found to be less and slightly right shifted when we move from full charges to reduced charges. These radial distribution functions are given in Figure 3.7.

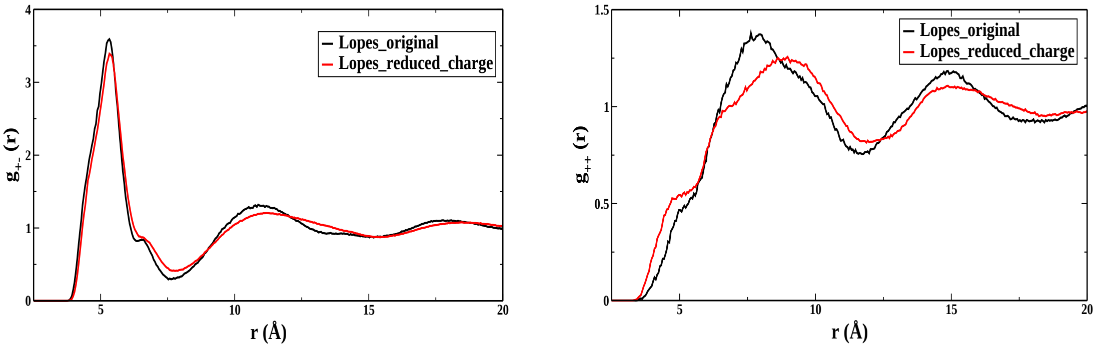

(a) g_{cat-an}(r) (b) $g_{cat-cat}$(r)

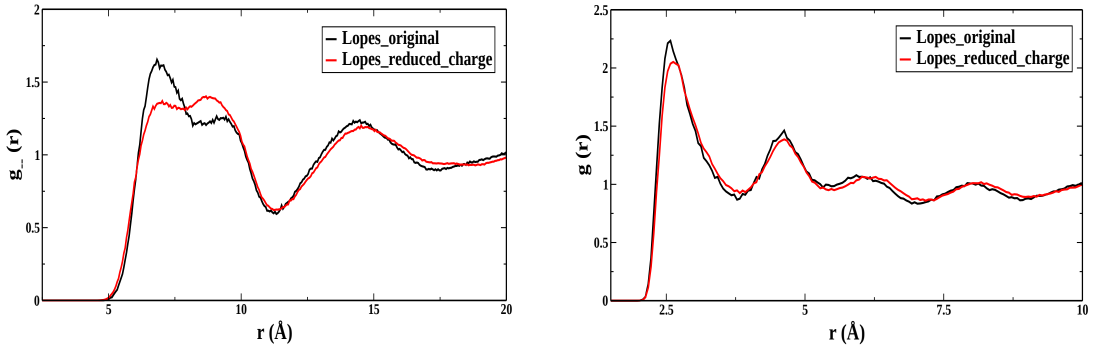

(c) g_{an-an}(r) (d) g_{H-F}(r)

Figure 3.7: Radial distribution function derived from NVT ensemble simulation for [BMIM][PF_6] using Lopes original parameters with reduced charges.

3.3.8 Heat of vaporization

One of the most important properties that is used to characterize ILs is vaporization enthalpy. It is almost an order magnitude higher than for molecular liquids because of strong electrostatic interaction between the ions.[84] It is very much important to properly reproduce the heats of vaporization, ΔH_{vap}, in addition to densities for ionic liquids as they both serve as key properties, representative of molecular size and intermolecular interactions.[85] Heat of vaporization is calculated as:

$$\Delta H_{vap} = \Delta H_{gas} - \Delta H_{liquid} = E_{total}(gas) - E_{total}(liquid) + RT \tag{3.6}$$

The average intra- and intermolecular energy for the ion pair in the gas phase from each ionic liquid combination gives the value of $E_{total}(gas)$ term. $E_{total}(liquid)$ is computed from the total potential energy of the liquid consisting of both the average intramolecular energy, $E_{intra}(liquid)$, and the average intermolecular energy, $E_{inter}(liquid)$. In enthalpy, the PV-work term is replaced by the RT term.

Table 3.8: Heat of vaporization values computed using reduced set of charges and compared with literature reported values. [a]Predicted values taken from Ref.[92] [b]Predicted values taken from Ref.[93] [c]Predicted values taken from Ref.[94]

System	ΔH_{vap} (kcal/mol)	
	Lit.	Reduced charge
[EMIM][BF_4]	24.00[a]	24.17
[EMIM][PF_6]	38.24[b]	33.67
[BMIM][Cl]	32.00[a]	19.55
[BMIM][PF_6]	45.80[c]	45.48
[BMIM][CF_3SO_3]	–	33.48

Comparison between the computed and experimental heats of vaporization ΔH_{vap}, values is very difficult because of the large deviations in reported experimental values obtained from different techniques. We have calculated the enthalpy of vaporization values for few ionic liquids using the reduced set of charges and Lopes parameters. They were compared with literature reported values and are given in Table 3.8. These calculated values match well with experiments except for [BMIM][Cl], for which computed value was little less than experimental value. In any case, we believe that the non-bonded parameters have to be refined.

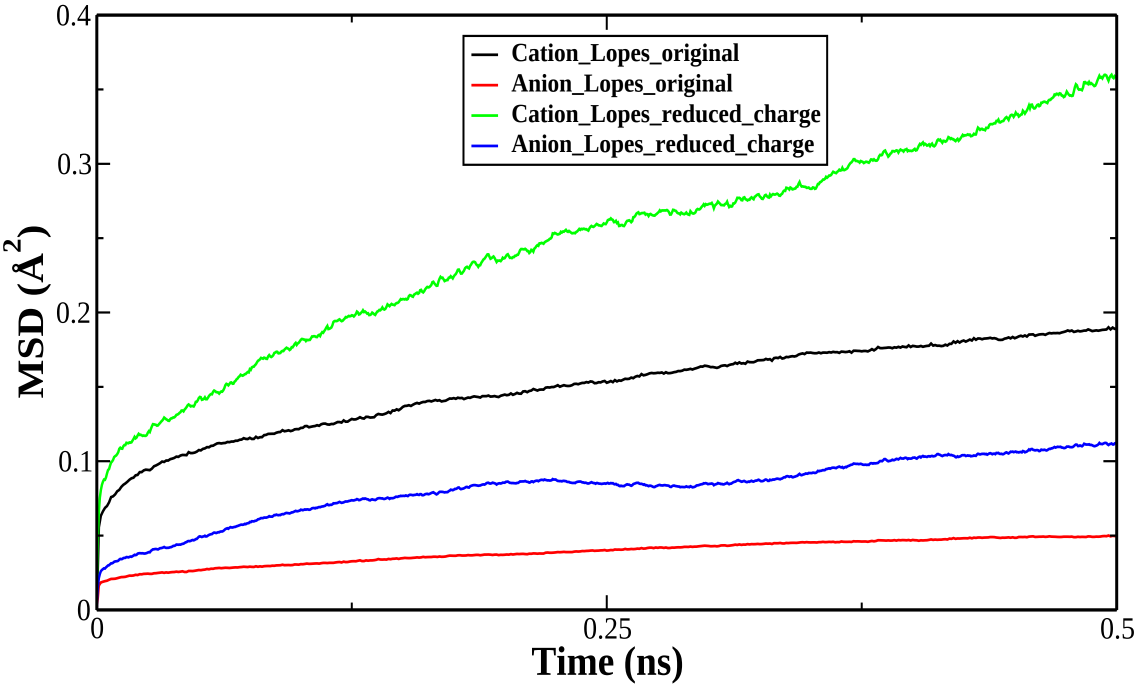

Figure 3.8: The computed center of mass mean square displacement in liquid [BMIM][PF$_6$] at 300 K.

3.3.9 Mean squared displacement

Translational properties of [BMIM][PF$_6$] was quantified through the mean square displacement of ion center of mass:

$$MSD(t) = \langle (r_i(t) - r_i(0))^2 \rangle \tag{3.7}$$

where $r_i(t)$ is the center of mass of ion at time t. The calculated MSDs are given in Figure 3.8 at 300 K. The reduced charge model yields much larger diffusion of ions. One of the serious drawbacks of the Lopes force field documented by many researchers is the nearly an order of magnitude difference between the diffusion coefficients obtained from it compared to experiment (the model underpredicts diffusion). Thus, the reduced charge model proposed in a systematic manner in the current chapter is a welcome improvement over the unit charge model which overbinds the ions.

The self-diffusion coefficients are calculated from from the MSD using the Einstein relation:

$$D_s = \frac{1}{6} \lim_{t \to \infty} \frac{d}{dt} \langle (r_i(t) - r_i(0))^2 \rangle \tag{3.8}$$

The self-diffusion coefficients were estimated from the slope of the MSD versus time in the diffusive region. In [BMIM][PF_6], the ion diffusion was significantly underestimated compared to experimental values by the full charges used in Lopes original force field. But, when we used the reduced set of charges, we found that the experimental self-diffusivities for both the cation and anion were reproduced very well. Hence, it is evident that the dynamic properties of ionic liquids are sensitive to the atomic charge distribution as well as to the total ion charges also.

3.4 Conclusions

In this work, we have come up with a way of deriving atomic charges of ionic liquids in a systematic manner by using density functional theory and plane wave basis set calculations on their crystalline phase. Previous efforts were also made where atomic charges of ionic liquids were calculated from AIMD run on the liquid phase[59,69–71] and also from AIMD calculations on crystal phase.[86] It is very much important to include the charge transfer and polarization effect for ionic liquids in their condensed phase, in the calculation of the atomic charges in ILs. In our calculations, with periodic boundary conditions, these were included in a direct manner. We have applied this method to a number of ILs, interestingly for all the ILs we obtained the total charge on the ions to be less than unity. The requirement of a crystal structure as input is the main difficulty or drawback of this procedure. Site charges in systems for which the crystal structure is unknown can also be obtained by performing classical MD simulations of their liquid phase using a reasonable force field, followed by geometry optimization (with 3-d periodic boundary conditions) within DFT. This procedure can be performed on several snapshots chosen from the classical MD trajectory. Interestingly, the charges obtained from this procedure match that obtained from the crystal, demonstrating that (a) the geometry optimized liquid structure is quite representative of the real system and (b) polarization and charge transfer effects are also captured using this simple but effective procedure. It is also further demonstrated that one does not need to carry out expensive ab initio MD simulations of the liquid state to obtain the site charges. Hitherto, this was the only approach used by researchers. The current study thus opens a new route to an inexpensive, robust and reliable way to obtain site charges in the condensed state.

Molecular dynamics simulations were carried out for a few ionic liquids using the new reduced set of charges combined with the rest of the force field developed by Lopes et al.[25] A few system properties were calculated to see the performance of this new set of reduced charges and these compared with results obtained from original Lopes parameters as well as experimental data. Static properties such as density, liquid phase structure in terms of radial distribution functions were calculated from the two different simulations. Calculated liquid densities using the new reduced set of charges underestimate the experimental densities by about 8%, whereas the densities obtained from original Lopes parameters were in better agreement with experimental results. In case of liquid phase structure, all the radial distribution functions was found to be shifted a little towards right side going from full charge to reduced charge. This is because, when the atomic charges get reduced, the electrostatic interactions between the ions also decreases; resulting in the appearance of peaks in radial distribution functions at larger distance. Also the height of those peaks get reduced using the reduced charges. The differences in density and in the pair correlation functions should not come as a surprise or as a dampener. They point to the increasing necessity of the refinement of the torsional and the non-bonded interaction parameters in the force field, an opinion shared by many researchers.[86]

However, reduced set of charges gave a good agreement for the heat of enthalpy (ΔH_{vap}) values with the experimental results. The full charge significantly underestimated the self-diffusivities of the ions; however, this property was well reproduced by simulations using the reduced charges.

Compared to static properties, dynamic properties are more sensitive to the magnitude and atomic charge distributions in ILs. The performance of this reduced set of charges can be improved by adjusting other parameters in the force field, for example, by tuning the vdW parameters. The short range interactions of the original force field contain also effective Coulomb interactions, an adaption to our proposed new set of partial charges is also necessary. Due to the connection with the 1-4 interactions, the dihedral interaction parameterization also get directly affected. Thus, it also needs to be refitted with respect to our new charge distribution and the LJ potentials. These will be attempted in the near future.

Bibliography

[1] a) J. Dupont, *Acc. Chem. Res.* 2011, **44,** 1223-1236; b) S. Werner, M. Haumann, P. Wasserscheid, *Ann. Rev. Chem. Biomol. Engin.* 2010, **1,** 203-230.

[2] F. Endres, *Chem. Ing. Tech.* 2011, **83,** 1485-1492.

[3] W. Meindersma, F. Onink, A. B. de Haan, in *Handbook of Green Chemistry, Vol.* **6***,* (Ed.: P. T. Anastas), Wiley-VCH, Weinheim, 2010, pp. 139-190.

[4] Z. Ma, J. Yu, S. Dai, *Adv. Mater.* 2010, **22,** 261-285.

[5] M. Maase, in *Ionic Liquids in Synthesis,* 2nd ed., (Eds.: P. Wasserscheid, T. Welton), Wiley-VCH, Weinheim, 2008, pp. 663-686.

[6] a) Maginn, E. *J. Acc. Chem. Res.* 2007, **40 (11),** 1200-1207; b) Maginn, E. J. *J. Phys.: Condens. Matter* 2009, **21 (37),** 373101.

[7] Hunt, P. A. *J. Phys. Chem. B* 2007, **111,** 4844-4853.

[8] Zahn, S.; Kirchner, B. *J. Phys. Chem. A* 2008, **112,** 8430-8435.

[9] Izgorodina, E. I.; Bernard, U. L.; Macfarlane, D. R. *J. Phys. Chem. A* 2009, **113,** 7064-7072.

[10] Del Popolo, M. G.; Lynden-Bell, R. M.; Kohanoff, *J. J. Phys. Chem. B* 2005, **109,** 5895-5902.

[11] Bühl, M.; Chaumont, A.; Schurhammer, R.; Wipff, G. *J. Phys. Chem. B* 2005, **109,** 18591-18599.

[12] Bhargava, B.; Balasubramanian, S. *Chem. Phys. Lett.* 2006, **417,** 486-491.

[13] Bagno, A.; DAmico, F.; Saielli, G. *ChemPhysChem* 2007, **8,** 873-881.

[14] Kirchner, B.; Seitsonen, A. P. *Inorg. Chem.* 2007, **46,** 2751-2754.

[15] Hadi, M.; Ansari, Y. *J. Chem. Phys.* 2007, **126,** 154502.

[16] Spickermann, C.; Thar, J.; Lehmann, S.; Zahn, S.; Hunger, J.; Buchner, R.; Hunt, P.; Welton, T.; Kirchner, B. *J. Chem. Phys.* 2008, **129,** 104505.

[17] Thar, J.; Brehm, M.; Seitsonen, A. P.; Kirchner, B. *J. Phys. Chem. B* 2009, **113,** 15129-15132.

[18] Zahn, S.; Thar, J.; Kirchner, B. *J. Chem. Phys.* 2010, **132,** 124506.

[19] Mallik, B.; Siepmann, J. I. *J. Phys. Chem. B* 2010, **114,** 12577-12584.

[20] Zahn, S.; Wendler, K.; Delle Site, L.; Kirchner, B. *Phys. Chem. Chem. Phys.* 2011, **13,** 15083-15093.

[21] Jorgensen, W.; Maxwell, D. S.; Tirado-Rives, J. *J. Am. Chem. Soc.* 1996, **118,** 11225-11236.

[22] Cornell, W. D.; Cieplak, P.; Bayly, C. I.; Gould, I. R.; Merz, K. M.; Ferguson, D. M.; Spellmeyer, D. C.; Fox, T.; Caldwell, J. W.; Kollman, P. A. *J. Am. Chem. Soc.* 1995, **117,** 5179-5197.

[23] Scott, W. R.; Hunenberger, P. H.; Tirono, I. G.; Mark, A. E.; Billeter, S. R.; Fennen, J.; Torda, A. E.; Huber, T.; Kruger, P.; van Gunsteren, W. F. *J. Phys. Chem. A* 1999, **103,** 3596-3607.

[24] MacKerell, A. D.; J.; Bashford, D.; Bellott, M.; Dunbrack, R. L.; Evanseck, J. D.; Field, M. J.; Fischer, S.; Gao, J.; Guo, H.; Ha, S.; et al. *J. Phys. Chem. B* 1998, **102,** 3586-3616.

[25] Canongia Lopes, J. N.; Deschamps, J.; Padua, A. A. *J. Phys. Chem. B* 2004, **108,** 2038-2047.

[26] Canongia Lopes, J. N.; Deschamps, J.; Padua, A. A. *J. Phys. Chem. B* 2004, **108,** 11250.

[27] Canongia Lopes, J. N.; Padua, A. A. *J. Phys. Chem. B* 2004, **108,** 16893-16898.

[28] Canongia Lopes, J. N.; Padua, A. A. *J. Phys. Chem. B* 2006, **110,** 19586-19592.

[29] Canongia Lopes, J. N.; Padua, A. A.; Shimizu, K. *J. Phys. Chem. B* 2008, **112,** 5039-5046.

[30] Liu, Z.; Huang, S.; Wang, W. *J. Phys. Chem. B* 2004, **108,** 12978-12989.

[31] Yan, T.; Li, S.; Jiang, W.; Gao, X.; Xiang, B.; Voth, G. A. *J. Phys. Chem. B* 2006, **110 (4),** 1800-1806.

[32] Wang, Y.; Voth, G. A. *J. Phys. Chem. B* 2006, **110 (37),** 18601-18608.

[33] Bhargava, B.; Balasubramanian, S.; Klein, M. L. *Chem. Commun.* 2008, 3339-3351.

[34] Morrow, T. I.; Maginn, E. J. *J. Phys. Chem. B* 2002, **106,** 12807-12813.

[35] Cadena, C.; Zhao, Q.; Snurr, R. Q.; Maginn, E. J. *J. Phys. Chem. B* 2006, **110 (6),** 2821-2832.

[36] Kelkar, M. S.; Maginn, E. J. *J. Phys. Chem. B* 2007, **111 (18),** 4867-4876.

[37] Micaelo, N. M.; Baptista, A. M.; Soares, C. M. *J. Phys. Chem. B* 2006, **110,** 14444-14451.

[38] Yan, T.; Burnham, C. J.; DelPopolo, M. G.; Voth, G. A. *J. Phys. Chem. B* 2004, **108 (32),** 11877-11881.

[39] Schroder, C. *Phys. Chem. Chem. Phys.* 2012, **14,** 3089.

[40] Chaban, V. V.; Voroshylova, I. V.; Kalugin, O. N. *Phys. Chem. Chem. Phys.* 2011, **13,** 7910-7920.

[41] Men, S.; Lovelock, K. R.; Licence, P. *Phys. Chem. Chem. Phys.* 2011, **13,** 15244-15255.

[42] Hurisso, B. B.; Lovelock, K. R.; Licence, P. *Phys. Chem. Chem. Phys.* 2011, **13,** 17737-17748.

[43] A. J. Arduengo, H. V. R. Dias, R. L. Harlow, M. Kline, *J. Am. Chem. Soc.,* 1992, **114,** 5530.

[44] J. D. Holbrey, W. M. Reichert, M. Nieuwenhuyzen, O. Sheppard, C. Hardacre, R. D. Rogers, *Chem. Commun.,* 2003, 476.

[45] S. M. Dibrov, J. K. Kochi, *Acta Crystallogr., Sect.C: Cryst. Struct. Commun.,* 2006, **62,** 19.

[46] C. S. Santos, S. Rivera-Rubero, S. Dibrov, S. Baldelli, *J. Phys. Chem. C,* 2007, **111**, 7682.

[47] A. R. Choudhury, N. Winterton, A. Steiner, A. I. Cooper, K. A. Johnson, *J. Am. Chem. Soc.,* 2005, **127**, 16792.

[48] J. D. Holbrey, W. M. Reichert, M. Nieuwenhuyzen, S. Johnston, K. R. Seddon, R. D. Rogers, *Chem. Commun.,* 2003, 1636.

[49] W. M. Reichert, J. D. Holbrey, R. P. Swatloski, K. E. Gutowski, A. E. Visser, M. Nieuwenhuyzen, K. R. Seddon, R. D. Rogers, *Cryst. Growth Des.,* 2007, **7**, 1106.

[50] C. Rijksen, R. D. Rogers, *J. Org. Chem.,* 2008, **73**, 5582.

[51] J. S. Wilkes, M. J. Zaworotko, *Chem. Commun.,* 1992, 965.

[52] M. Gjikaj, J. C. Leye, Tao Xie, W. Brockner, *Cryst. Eng. Comm.,* 2010, **12**, 1474.

[53] Noda, A.; Hayamizu, K.; Watanabe, M. *J. Phys. Chem. B,* 2001, **105,** 4603-4610.

[54] Matsumotoa, K.; Hagiwara, R. *J. Fluorine Chem.,* 2007, **128,** 317-331.

[55] Huddleston, J. G.; Visser, A. E.; Reichert, W. M.; Willauer, H. D.; Broker, G. A.; Rogers, R. D. *Green Chem.* 2001, **3,** 156-164.

[56] Branco, L. C.; Rosa, J. N.; Ramos, J. J. M.; Afonso, C. A. M. *Chem. Eur. J.,* 2002, **8,** 3671-3677.

[57] Tokuda, H.; Hayamizu, K.; Ishii, K.; Susan, M. A. B. H.; Watanabe, M. *J. Phys. Chem. B,* 2004, **108,** 16593.

[58] Borodin, O. *J. Phys. Chem. B* 2009, **113,** 11463-11478.

[59] Bhargava, B. L.; Balasubramanian, S. *J. Chem. Phys.* 2007, **127 (11),** 114510.

[60] Bhargava, B. L.; Balasubramanian, S. *J. Phys. Chem. B.* 2007, **111 (17),** 4477-4487.

[61] Zhao, W.; Eslami, H.; Cavalcanti, W. L.; Müller-Plathe, F. Z. *Phys. Chem.* 2007, **221,** 1647-1662.

[62] Chaban, V. *Phys. Chem. Chem. Phys.* 2011, **13,** 16055-16062.

[63] Kosmann, S.; Thar, J.; Kirchner, B.; Hunt, P. A.; Welton, T. *J. Chem. Phys.* 2006, **124,** 174506.

[64] Martin, F.; Zipse, H. *J. Comput. Chem.* 2004, **26 (1),** 97-105.

[65] C. M. Breneman and K. B. Wiberg, *J. Comput. Chem.,* 1990, **11,** 361-373.

[66] B. H. Besler, K. M. Merz and P. A. Kollman, *J. Comput. Chem.,* 1990, **11,** 431-439.

[67] M. A. Spackman, *J. Comput. Chem.,* 1996, **17,** 1-18.

[68] Bader, R. *Atoms in Molecules: A Quantum Theory;* Oxford University Press: 1990.

[69] Schmidt, J.; Krekeler, C.; Dommert, F.; Zhao, Y.; Berger, R.; Delle Site, L.; Holm, C. *J. Phys. Chem. B* 2010, **114,** 6150-6155.

[70] Wendler, K.; Zahn, S.; Dommert, F.; Berger, R.; Holm, C.; Kirchner, B.; Delle Site, L. *J. Chem. Theory Comput.* 2011, **7,** 3040-3044.

[71] Wendler, K.; Dommert, F.; Zhao, Y.; Berger, R.; Holm, C.; Delle Site, L. *Faraday Discuss.* 2012, **154,** 111-132.

[72] Blochl, P. E. *J. Chem. Phys.* 1995, **103,** 7422-7428.

[73] Cp2k, http://www.cp2k.org.

[74] Goedecker, S.; Teter, M.; Hutter, *J. Phys. Rev. B* 1996, **54,** 1703-1710.

[75] Hartwigsen, C.; Goedecker, S.; Hutter, *J. Phys. Rev. B* 1998, **58,** 3641-3662.

[76] The Cambridge Structural Database: a quarter of a million crystal structures and rising F. H. Allen, *Acta Crystallogr.,* **B58,** 380-388, 2002.

[77] New software for searching the Cambridge Structural Database and visualising crystal structures I. J. Bruno, J. C. Cole, P. R. Edgington, M. Kessler, C. F. Macrae, P. McCabe, J. Pearson and R. Taylor, *Acta Crystallogr.,* **B58,** 389-397, 2002.

[78] Isostar: A library of information about non-bonded interactions I. J. Bruno, J. C. Cole, J. P. M. Lommerse, R. S. Rowland, R. Taylor and M. L. Verdonk, *J. Comput.-Aided Mol. Des.,* **11,** 525-537, 1997.

[79] Mercury: visualization and analysis of crystal structures C. F. Macrae, P. R. Edgington, P. McCabe, E. Pidcock, G. P. Shields, R. Taylor, M. Towler and J. van de Streek, *J. Appl. Cryst.,* **39,** 453-457, 2006.

[80] S.J. Plimpton, *J. Comp. Phys.*, **117**, 1 (1995).

[81] Marcus G. Martin; J. IljaSiepmann, *J. Phys. Chem. B* 1998, **102,** 2569-2577.

[82] W. Humphrey, A. Dalke, K. Schulten, *J. Molec. Graphics*, **14**, 33 (1996).

[83] Youngs, T. G.; Hardacre, C. *ChemPhysChem* 2008, **9,** 1548-1558.

[84] Weingaertner, H. *Angew. Chem., Int. Ed.,* 2008, **47,** 654-670.

[85] Jorgensen, W. L.; Tirado-Rives, J. *Proc. Nat. Acad. Sci. U.S.A.,* 2005, **102,** 6665-6670.

[86] Y. Zhang and Edward J. Maginn, *J. Phys. Chem. B,* 2012, **116 (33)**, 10036-10048.

[87] Jong-Min Lee, S. Ruckes, J. M. Prausnitz, *J. Phys. Chem. B,* 2008, **112,** 1473-1476.

[88] S. Zhanga, X. Qia, X. Maa, L. Lua, Q. Zhanga and Y. Deng, *J. Phys. Org. Chem.,* 2011.

[89] B. Kirchner. *TOPICS IN CURRENT CHEMISTRY: Ionic Liquids*, Springer, 2009.

[90] Y. Zhang and P. S. Cremer, *Current Opinion in Chemical Biology,* 2006, **10,** 658-663.

[91] J. M. Roberts, A. R. Diaz, D. T. Fortin, J. M. Friedle, and S. D. Piper, *Anal. Chem.,* 2002, **74,** 4927-4932.

[92] S. V. Sambasivarao and O. Acevedo, *J. Chem. Theory Comput.*, **2009,** 5, 1038-1050.

[93] Deyko, A.; Hessey, S. G.; Licence, P.; Chernikova, E. A.; Krasovskiy, V. G.; Kustov, L. M.; Jones, R. G. *Phys. Chem. Chem. Phys.*, **2012,** 14, 3181-3193.

[94] Y.U. Paulechka, G.J. Kabo, A.V. Blokhin, O.A. Vydrov, J.W. Magee, M. Frenkel, *J. Chem. Eng. Data* **2003**, *48*, 457.

Chapter 4

Vibrational signatures of cation-anion hydrogen bonding in ionic liquids: A preliminary study

4.1 Introduction

Among the multitude of interactions prevalent in molten salts (ionic liquids), the predominant one is the electrostatic. The Coulombic interactions lead to strong binding energies, of the order of 500 kJ mol^{-1} or more. Thus, at room temperature most of the inorganic molten salts are found to be at solid state. As discussed in the previous chapter, ionic liquids (ILs) are a class of molten salts which have melting point below 100 °C. At room temperature, many ionic liquids are found to be liquid, and some of them even freeze only at -90 °C. One of the most interesting properties of ionic liquids is their negligible vapor pressure up to very high temperatures. These ionic liquids show promising applications in various fields, such as in electrochemistry, analytics, nanomaterials processing, and engineering fluids.[1–3] Research on ionic liquids has been spurred by both academic interest as well as aimed at such applications.

An important subset of ionic liquids are the protic ionic liquids (PILs), which can be synthesized by combining an equimolar amount of a Brønsted acid and a Brønsted base.[4–9] An important property of protic ionic liquids is the presence of proton-donor and proton-acceptor sites, through which the protons are transferred from the acid to the base. These proton-donor and proton-acceptor sites are used to build up the hydrogen-bonded network in protic ionic liquids. This key characteristic distinguishes protic ionic liquids from their aprotic counterparts. Besides this, protic ionic liquids possess a number of unique properties such as complete proton transfer,[4] protein stabilization,[6] eutectic mixtures of PILs are liquid below 100 °C etc. Thus, protic ILs serve as perfect models to study the presence and strength of hydrogen bonding, number of hydrogen-bond donors, the interaction strength and the network formation in the liquid state.

Hydrogen bonding is an extensively studied topic in chemistry and biology because of its influence on chemical and biological systems. Hydrogen bonding is mainly attributed to electrostatic interaction, whereas electron correlation effect contributes to the dispersion character also. The structure of hydrogen bonded complex is dictated by the chemical structure of individual moieties. Generally, hydrogen bonding is known to be a directional interaction, of type $X\text{-}H\cdots Y$, where X is the donor and Y is hydrogen bond acceptor and $R(X\cdots Y)$ is less than the sum of van der Waals radii of X and Y. Therefore, in a hydrogen bonded complex, it appears to be an orbital overlap between the orbitals on both electronegative atoms X and Y. The strength of this interaction is determined by three main contributions: Coulomb, induction forces due to the dipole-dipole interaction and the dispersion forces due to electron correlation effects. Systems where the bonds involved are having non-negligible dipole moment, Coulomb and induction interactions dominates over the dispersion interactions. In ionic systems, the leading interaction becomes that of the ion-dipole (induced dipole) type. Dispersion forces decay very fast with distance ($\sim R^{-6}$), hence it can have role only at short distances between species. However, Coulomb and induction forces change much more slowly, they are stronger and long-range forces. For example, with distance ion-dipole interactions decay as R^{-2}; dipole-dipole interactions as R^{-3}; and ion-induced dipole interactions as R^{-4}.

Many experimental techniques have been used to study the intermolecular interactions between molecules and ions. These interactions cover the frequency range between 1 and 300 cm^{-1}. The ionic motions in ionic liquids have been characterised by experimental methods which include terahertz spectroscopy,[10,11] dielectric spectroscopy,[12–14] nuclear magnetic resonance spectroscopy,[14] heterodyne-detected Raman-induced Kerr effect,[13,15–17] infrared spectroscopy[18,19] etc. Recently, Ludwig et al. have shown that terahertz (THz) and far-infrared (FIR) spectroscopy can be used to study the frequency range in aprotic ionic liquids which includes vibrational bands describing the strength of cation-anion interactions.[20] In a molten salt, the cation rattles within a cage of the anion and vice versa. The rattling frequency typically is in the far infrared region and can be studied using vibrational spectroscopy. This frequency carries the signature of cation-anion interaction and the band position is proportional to the strength of the interaction. Naturally, hydrogen bonded ion partners will exhibit a far-IR band at a higher wave number than one which do not have the hydrogen bonding. Ludwig et al.[21] report such an observation by examination of a series of protic ionic liquids in which cations can form multiple (including zero) number of hydrogen bonds with the anions. Thus, there is a dire need of theoretical modelling to interpret the resultant low-frequency spectra; to explain the origins of spectral absorptions and to assign intra- and intermolecular vibrational modes. Ab initio quantum chemical calculation or density functional theory (DFT) calculations have been performed on ion-pair clusters of ionic liquids; also classical as well as ab initio molecular dynamics simulations have been reported in this respect.[22–28]

Despite these developments, there are still some problems in evaluating the low-frequency spectra. Different kinds of intermolecular interactions contribute to this part of frequency, hence it is difficult to distinguish them properly. Some research groups have suggested that long-range electrostatic interactions attribute to these bands rather the hydrogen bonding.[29,30] Sarangi et al.[28] proposed that in room temperature ionic liquids, the low frequency band arises primarily from interionic interactions and they showed by their calculations that short range interactions can reproduce the low frequency band. Recently, Ludwig et al. have studied few protic ionic liquids at room temperature.[31] They have measured the FIR spectra of tetramethylammonium nitrate $[(CH_3)_4N][NO_3]$ and trimethylammonium nitrate $[(CH_3)_3NH][NO_3]$. For $[(CH_3)_3NH][NO_3]$, they observed a distinct vibrational mode at 171 cm^{-1}, which was not present in the case of $[(CH_3)_4N][NO_3]$. They also have performed zero temperature, density functional theory (DFT) calculations of small clusters of neutral ion pairs in the gas phase. Coupled with NMR results on these ionic liquids, they conclude that this band represents vibrations associated with anion-cation interaction and can easily be assigned to the $^{+}N\text{-}H\cdots NO_3^{-}$ hydrogen bond.

In the current study, we attempt to obtain a better understanding of the low frequency modes in ionic liquids. We performed ab initio quantum chemical calculations (within density functional theory) on both isolated ion pairs as well as on clusters of ion pairs. We also plan to carry out vibrational spectral calculations on crystals of these compounds and analyze the atomic displacements corresponding to the low frequency modes. The current set of calculations (essentially gas phase ones) are thus preliminary in nature. Results from all the calculations and simulations are hoped to offer a clear view of the origin of this low frequency band.

4.2 Computational Details

We have examined three alkylammonium salts: dimethylammonium bromide $[(CH_3)_2NH_2][Br]$; trimethylammonium bromide $[(CH_3)_3NH][Br]$ and tetramethylammonium bromide $[(CH_3)_4N][Br]$. As can be seen, the anion is the same in these three; however the cations have different number of methyl groups. More the number of methyl groups, less is their capability to form hydrogen bonds with the anions. While we plan to carry out ab initio MD simulations and vibrational calculations of the crystalline phases of these compounds, currently we provide results on gas phase calculations. In the gas phase, the geometries and vibrational spectra of models of these salts were obtained at PBE/6-31++G(d,p) level of theory using the Gaussian09 code.[32] In order to have a complete description of electron correlation, geometry optimizations of all the salts were also performed at MP2/aug-cc-pvdz level of theory. Harmonic vibrational analysis was carried out at the MP2 level and those spectra were compared with those obtained at PBE/6-31++G(d,p) level. Gaussview was used to model the initial geometries of the salts. A tight optimization was performed in all the cases by employing the keywords "Opt=verytight" and "scf=verytight" during optimizations. In this approach, the convergence criteria for the root mean square of force on the nuclei and on the wave function became 10^{-6} and 10^{-8} a.u. respectively. In addition to this, in the DFT calculations, an ultrafine grid has been used. Normal mode calculations of these systems at the harmonic level showed no imaginary frequencies, indicating that they were indeed in their true energy minima. We also considered clusters of two and three ion pairs for all these salts. All the clusters have been optimized at the MP2/aug-cc-pvdz level of theory by the inclusion of "Opt=verytight" and "scf=verytight" keywords during optimizations. Optimized geometries of these clusters were used to perform the normal mode calculations at the harmonic level. No imaginary frequency was found for any of these clusters as well.

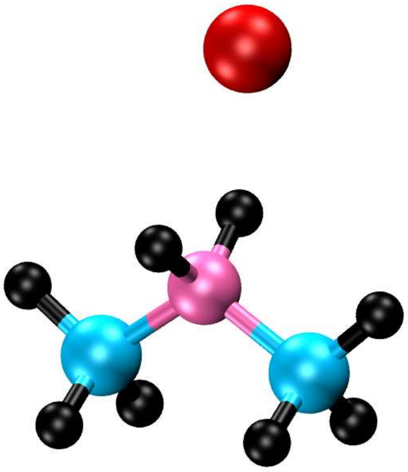

(a) Dimethylammonium bromide

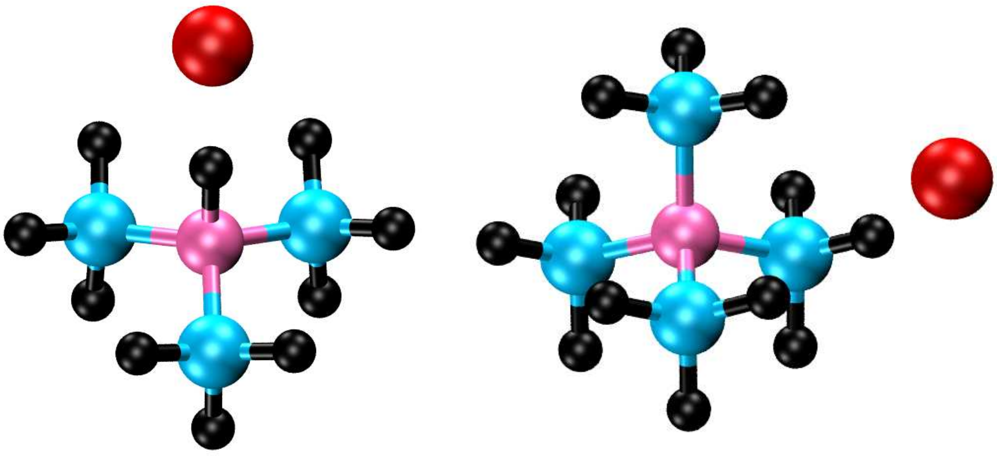

(b) Trimethylammonium bromide (c) Tetramethylammonium bromide

Figure 4.1: Different alkylammonium salts which have been studied here. Colors: Nitrogen-pink, Carbon-black, Hydrogen-cyan, Bromine-red.

Ab initio molecular dynamics simulations were performed using the CPMD-3.13.2 package.[33] A plane wave basis set was used to expand the wave function of the valence electrons. The energy and density cutoff used were 150 Ry and 900 Ry respectively. The norm conserving Troullier-Martins pseudopotentials[34] were used to consider the effect of all the core electrons and of the nucleus on the valence electrons. The effect of exchange and correlation effects were considered by using Perdew, Burke and Ernzerhof (PBE) functional.[35] The effect of van der Waals interactions (vdW) was considered through empirically determined Grimme's van der Waals correction.[36] In the gas phase for isolated molecules (or complexes), the gradient on the wave functions and on the nuclear positions were optimized every step with convergence criteria of 10^{-7} and 10^{-5} respectively. The minimized structure was used to obtain the vibrational spectra. For the crystal systems, initial cell parameters and atomic positions were taken from Cambridge structural database.[37–39] Depending on magnitude of cell parameters, two replicas in each direction were used for building supercell. Each of these systems was optimized by varying the cell parameters and coordinates iteratively until a energy minimum was found. On the final geometries, normal mode analysis have been performed at the harmonic level.

All the systems were visualized using Gaussview,[32] Mercury,[40] Jmol[41,42] and VMD.[43]

4.3 Results and Discussion

Normal mode analysis was performed for three alkylammonium salts in gas phase. The frequencies which were above 400 cm^{-1} can be attributed to intramolecular interactions and hence are not of interest here. The calculated spectra exhibit bands at sub-200 cm^{-1} which are usually attributed to unspecified librational motions. For the three different systems, the band positions decrease in wave number going from dimethyl based cation to the tetramethyl based one. It implies that the far-infrared absorption red shifts with decreasing propensity for the formation of cation-anion hydrogen bond.

Vibrational spectra obtained at PBE/6-31++G(d,p) level for $[(CH_3)_2NH_2][Br]$ showed the characteristic frequency at about 220.75 cm^{-1}, whereas for $[(CH_3)_3NH][Br]$ and $[(CH_3)_4N][Br]$, it was at 196.42 cm^{-1} and 150.38 cm^{-1} respectively. On the other hand, in the MP2/aug-cc-pvdz level, these frequencies were present at about 220.28 cm^{-1}, 193.05 cm^{-1} and 146.05 cm^{-1} respectively for the three systems. Vibrational spectra obtained from gas phase calculations using the plane wave basis set (i.e., within CPMD) always showed the appearance of the characteristic band at marginally higher frequencies than ones calculated with localised basis set. The corresponding frequencies for the three salt clusters calculated with CPMD were found to be: 245.38 cm^{-1}, 201.33 cm^{-1} and 148.09 cm^{-1} respectively. The calculated spectra (up to 300 cm^{-1}) of these alkylammonium salts are plotted in Figure 4.3.

Let us examine the data in terms of the cation-anion hydrogen bonding. In dimethylammonium bromide, there are two acidic protons on the nitrogen atom, whereas in trimethylammonium bromide only one acidic hydrogen is present on the nitrogen atom. Further, in tetramethylammonium bromide there are no acidic protons depriving it of any hydrogen bonding interaction with the anion. In trimethylammonium bromide, we can expect a single hydrogen bond between anion and cation, however, the bromide anion can form hydrogen bond with either or both of the acidic protons in dimethylammonium bromide. The interaction strength between the anion and the cation influences the position of vibrational band to a large extent. Going from the dimethyl- to the tetramethylammonium cation, hydrogen bond formation ability decreases, implying a decreasing order in interaction strength. One more factor, which is the well known “inductive effect” also plays a crucial role here. In a molecule, the transmission of charge through a chain of atoms by electrostatic induction is known as inductive effect. Inductive effect can be either

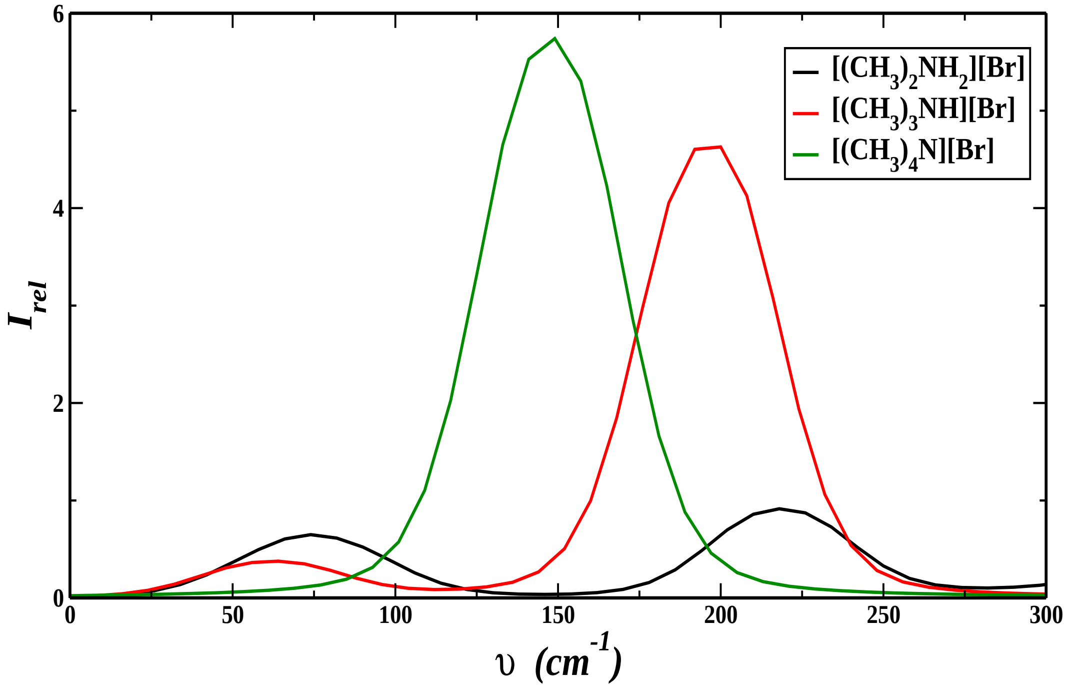

Figure 4.2: Calculated FIR spectra of alkylammonium salts at the PBE/6-31++G(d,p) level.

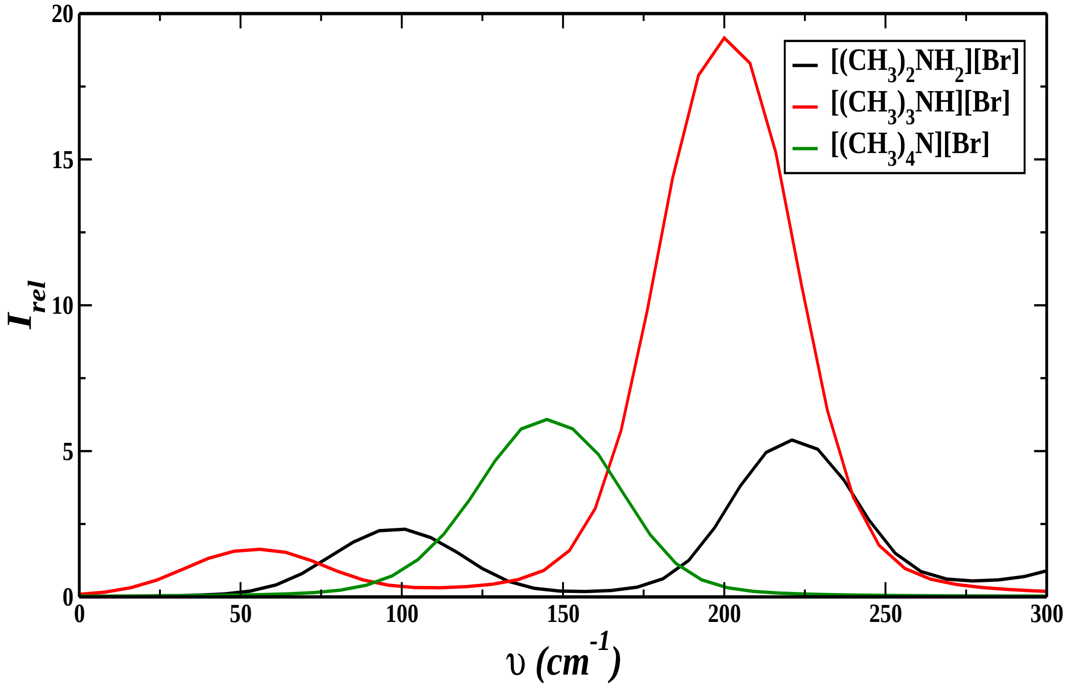

Figure 4.3: Calculated FIR spectra of alkylammonium salts at the MP2/aug-cc-pvdz level.

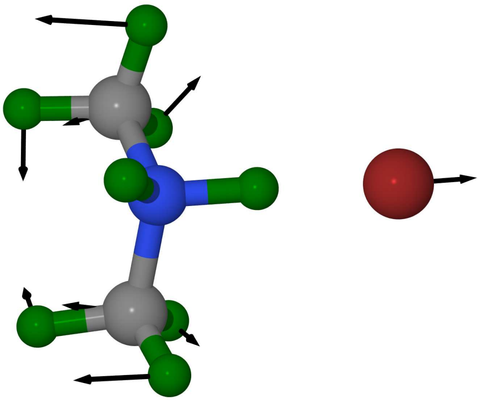

(a) Dimethylammonium bromide

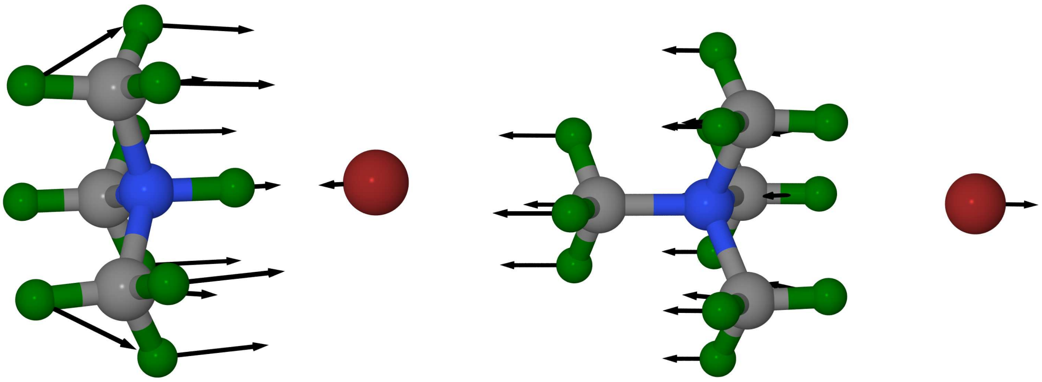

(b) Trimethylammonium bromide (c) Tetramethylammonium bromide

Figure 4.4: The atomic displacement vectors corresponding to the inter-ion low frequency mode. Colors: Nitrogen-blue; Carbon-grey; Hydrogen-green and Bromine-red.

positive or negative in nature. From the dimethyl- to the tetramethyl- group the electron releasing character increases. This would lead to lesser charge transfer into the N-H antibonding orbital as the electron density at ammonium nitrogen increases – indicating a weaker hydrogen bond. Thus, it is evident that the red shift in the frequency band appears as the hydrogen bond weakens. Therefore, it is clear that the characteristic frequency band represents anion-cation interaction and can easily be assigned to $^{+}$N-H$\cdots$Br^{-} hydrogen bond. Visualisation of these characteristic vibrational mode showed the displacement vectors between the cation and anion in particular. Those atomic displacement vectors corresponding to the $^{+}$N-H$\cdots$Br^{-} hydrogen bond mode in three different salts have been shown in Figure 4.4.

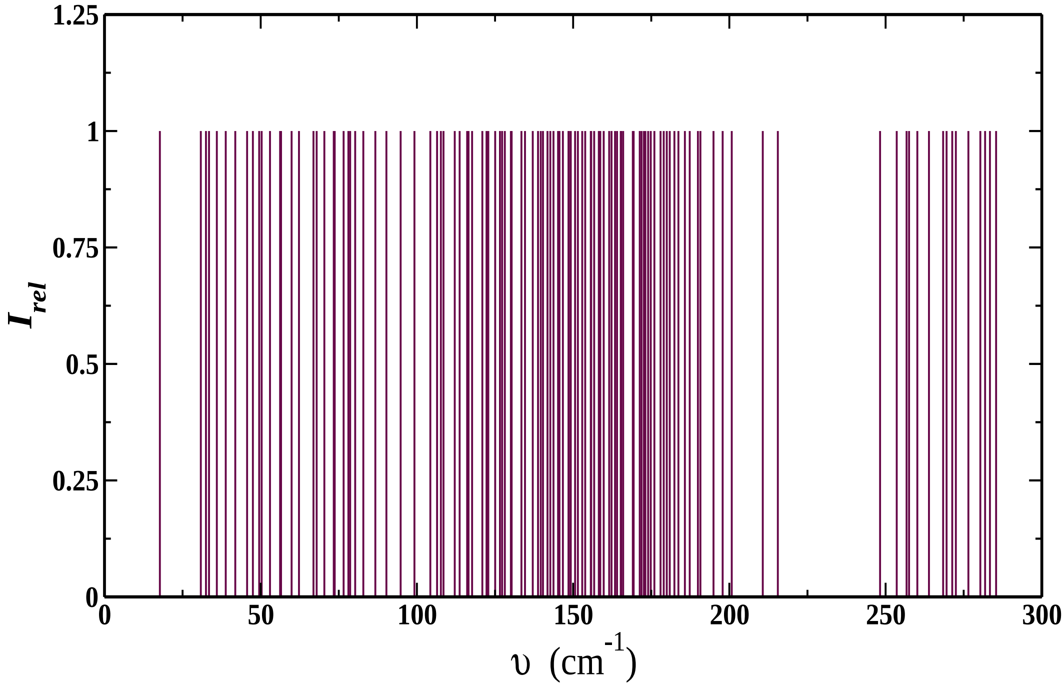

Figure 4.5: Stick pattern of calculated FIR spectra from crystalline phase simulation of dimethylammonium bromide.

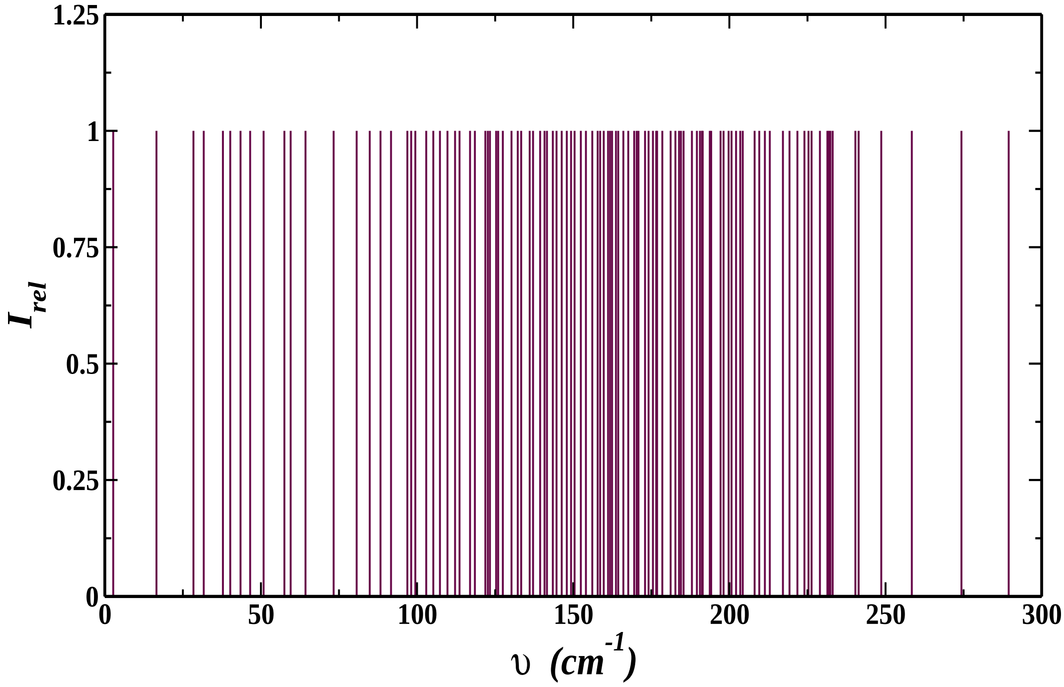

Figure 4.6: Stick pattern of calculated FIR spectra from crystalline phase simulation of trimethylammonium bromide.

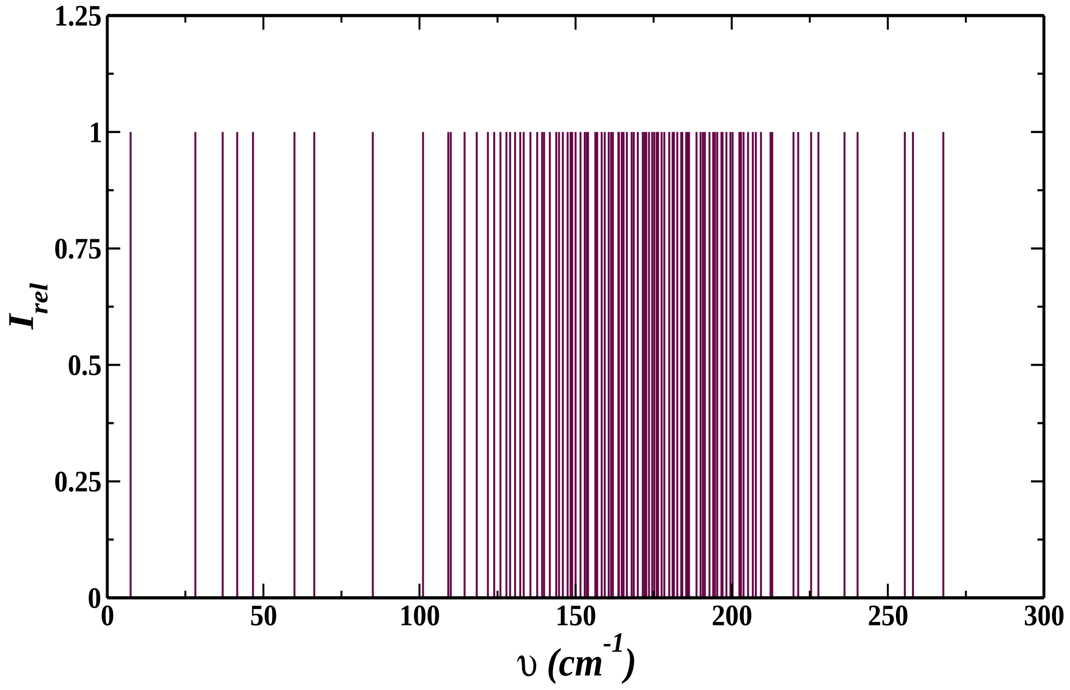

Figure 4.7: Stick pattern of calculated FIR spectra from crystalline phase simulation of tetramethylammonium bromide.

Up to now we saw the different comparisons in gas phase single ion pair vibrational analysis. In order to observe the correlation between gas phase and bulk phase vibration spectra, we performed the hessian calculations on the crystal phase of these three salts also. The vibrational spectra obtained from the crystal phase simulations of these three different salts, showed a group of frequencies in some specific regions. Among those group of frequencies, there were few vibrational modes noticed, which corresponds to the interactions between cation and anion in the salts. In those collection of modes, we observed that all the ion pairs were not showing the displacement vectors in every frequency. In a particular mode, only one or two ion pairs were involved in the harmonic motion. In those group of frequencies, each vibrational mode were separated by few cm^{-1} (1-2 cm^{-1}). Here, the group of vibrational band for dimethyl-, trimethyl- and tetramethylammonium bromide, started appearing from 248 cm^{-1}, 198 cm^{-1} and 150 cm^{-1} respectively. Therefore, it is evident that the trend we observed in the gas phase vibrational analysis, is also quite present in the bulk phase of these ammonium salts. As we move from dimethyl- to tetramethylammonium bromide, the interaction strength between anion and cation decreases, leading to the low wavenumber appearance of the vibrational band corresponding to anion-cation interaction. This phenomenon also suggests the presence of low frequency bands due to presence of hydrogen bond between in protic ionic liquids. The frequencies obtained from these bulk phase simulations are plotted against an arbitrarily chosen intensities as we CPMD calculation do not produce the intensity values explicitly. For all the three different alkylammonium salts, these frequency profiles are given in Figure 4.5, Figure 4.6 and Figure 4.7.

4.4 Conclusions

In protic ionic liquids, we have observed that the H-bond vibrational modes can be located in the 140-220 cm^{-1} region of the far infrared spectra. Vibrational analysis from cluster calculations are have provided rich information on the nature of these modes. Specifically, we find a clear blue shift in the far-IR mode with increasing number of hydrogen bonding sites on the cation. Our endeavor now will be to study these systems in the condensed phases – both crystalline and the liquid. The former are easier to study and inexpensive. The modes too can be visualized and assigned in an uncomplicated manner for the crystalline phase. The liquid phase simulations will be performed for a direct comparison to experiments. Attention will be paid to the strength and geometrical characteristics of the cation-anion hydrogen bonds and how these aspects influence the far-infrared vibrational spectra.

Bibliography

[1] F. Endres, S. Z. El Abedin, *Phys. Chem. Chem. Phys*, 2006, **8,** 2101.

[2] R. D. Rogers, K. R. Seddon, *Science*, 2003, **302,** 792-793.

[3] P. Wasserscheid, T. Welton, *Ionic Liquids in Synthesis*, 2nd ed., Wiley-VCH, Weinheim, 2008,

[4] T. L. Greaves, C. J. Drummond, *Chem. Rev*, 2008, **108**, 206-237.

[5] E. Bodo, P. Postorino, S. Mangialardo, G. Piacente, F. Ramondo, F. Bosi, P. Ballirano, R. Caminiti, *J. Phys. Chem. B*, 2011, **115**, 13149-13161.

[6] C. A. Angell, N. Byrne, J.-P. Belieres, *Acc. Chem. Res*, 2007, **40**, 1228-1236.

[7] W. Xu, C. A. Angell, *Science*, 2003, **302**, 422-425.

[8] J. Stoimenovski, E. I. Izgorodina, D. R. MacFarlane, *Phys. Chem. Chem. Phys.*, 2010, **12**, 10341-10347.

[9] A.Wulf, K. Fumino, R. Ludwig, *Angew. Chem*, 2009, **121**, 3230-3233.

[10] Yamamoto, K.; Tani, M.; Hangyo, M. *J. Phys. Chem. B*, 2007, **111**, 4854.

[11] Stoppa, A.; Hunger, J.; Buchner, R; Hefter, G.; Thoman, A.; Helm, H. *J. Phys. Chem. B*, 2008, **112**, 4854.

[12] Daguenet, C.; Dyson, P. J.; Krossing, I.; Oleinikova, A.; Slattery, J.; Wakai, C.; Weingartner, H. *J. Phys. Chem. B*, 2006, **110**, 12682.

[13] Turton, D. A.; Hunger, J.; Stoppa, A.; Hefter, G.; Thoman, A.; Walther, M.; Buchner, R.; Wynne, K *J. Am. Chem. Soc.*, 2009, **131**, 11140.

[14] Nakamura, K.; Shikata, T. *ChemPhysChem*, 2010, **11**, 285.

[15] Shirota, H.; Castner, E. W. *J. Phys. Chem. A*, 2005, **109**, 9388.

[16] Xiao, D.; Rajian, J. R.; Hines, L. G., Jr.; Li, S.; Bartsch, R. A.; Quitevis, E. L. *J. Phys. Chem. B*, 2008, **112**, 13316.

[17] Fujisawa, T.; Nishikawa, K.; Shirota, H. *J. Chem. Phys*, 2009, **131**, 244519.

[18] Dominguez-Vidal, A.; Kaun, N.; Ayora-Canada, M. J.; Lendl, B. *J. Phys. Chem. B*, 2007, **111**, 4446.

[19] Yokozeki, A.; Kasprzak, D. J.; Shiflett, M. B. *Phys. Chem. Chem. Phys.*, 2007, **9**, 5018.

[20] R. Ludwig, A. Wulf, K. Fumino, P. F. Taday, *ChemPhysChem*, 2010, **11**, 349-353.

[21] A. Wulf, K. Fumino, R. Ludwig, *Angew. Chem*, 2010, **122**, 459-463; *Angew. Chem*, 2010, **49**, 449-453.

[22] P. A. Hunt, B. Kirchner, T.Welton, *Chem. Eur. J.*, 2006, **12**, 6762-6775.

[23] F. Dommert, J. Schmidt, B. Qiao, Y. Zhao, C. Krekeler, L. Delle Site, R. Berger, C. Holm, *J. Chem. Phys.*, 2008, **129**, 224501.

[24] P. A. Hunt, I. R. Gould, B. Kirchner, *Aust. J. Chem.*, 2007, **60**, 9-14.

[25] S. Zahn, J. Thar, B. Kirchner, *J. Chem. Phys.*, 2010, **132**, 124506.

[26] E. I. Izgorodina, *Phys. Chem. Chem. Phys*, 2010, **13**, 4189-41207.

[27] H. V. Spohr, G. N. Patey, *J. Chem. Phys.*, 2010, **132**, 154504.

[28] S. S. Sarangi, S. K. Reddy, S. Balasubramanian, . *Phys. Chem. B*, 2011, **115**, 1874-1880.

[29] T. Buffeteau, J. Grondin, Y. Danten, J.-C. Lassege, *J. Phys. Chem. B*, 2010, **114**, 7587-7592.

[30] J. Grondin, J.-C. Lassege, D. Cavagnat, T. Buffeteau, P. Johansson, R. Holomb, *J. Raman Spectrosc.*, 2011, **42**, 733-743.

[31] K. Fumino, E. Reichert, K. Wittler, R. Hempelmann. R. Ludwig, *Angew. Chem*, 2012, **51**, 6236-6240.

[32] Frisch, M. J.; et al. Gaussian 09, Revision B. 01; Gaussian Inc.; Wallingford, CT, 2010.

[33] Hutter, J.; Ballone, J. P.; Bernasconi, M.; Focher, P.; Fois, E.; Goedecker, S.; Marx, D.; Parrinello, M.; Tuckerman, M. E. CPMD, version 3.13.2; Max Planck Institut fuer Festkoerperforschung and IBM Zurich Research Laboratory: Stuttgart, Germany, and Zurich, 1990.

[34] Troullier, N.; Martins, J. L. *Phys. Rev. B*, 1991, **43**, 1993.

[35] Perdew, J. P.; Burke, K.; Emzerhof, M. *Phys. Rev. Lett.*, 1996, **77**, 3865.

[36] S. Grimme, *J. Comp. Chem.*, 2006, **27**, 1787.

[37] The Cambridge Structural Database: a quarter of a million crystal structures and rising F. H. Allen, *Acta Crystallogr.,* **B58,** 380-388, 2002.

[38] New software for searching the Cambridge Structural Database and visualising crystal structures I. J. Bruno, J. C. Cole, P. R. Edgington, M. Kessler, C. F. Macrae, P. McCabe, J. Pearson and R. Taylor, *Acta Crystallogr.,* **B58,** 389-397, 2002.

[39] Isostar: A library of information about non-bonded interactions I. J. Bruno, J. C. Cole, J. P. M. Lommerse, R. S. Rowland, R. Taylor and M. L. Verdonk, *J. Comput.-Aided Mol. Des.,* **11,** 525-537, 1997.

[40] Mercury: visualization and analysis of crystal structures C. F. Macrae, P. R. Edgington, P. McCabe, E. Pidcock, G. P. Shields, R. Taylor, M. Towler and J. van de Streek, *J. Appl. Cryst.,* **39,** 453-457, 2006.

[41] Jmol:An open-source Java viewer for chemical structures in 3D. http://www.jmol.org/

[42] McMahon, B.; Hanson, R. M. *J. Appl. Crystallogr.* 2008, **41**, 811.

[43] W. Humphrey, A. Dalke, K. Schulten, *J. Molec. Graphics*, **14**, 33 (1996).